SELF-ORGANIZATION OF THE CLIMATE SYSTEM: SYNCHRONIZED POLAR AND OCEANIC TELECONNECTIONS

Elizabeth Piccard Reischmann

A dissertation submitted to the faculty of the University of North Carolina at Chapel Hill in partial fulfillment of the requirements for the degree of Doctor of Philosophy in the Department of Geological Sciences.

Chapel Hill
2016

Approved by:

José A. Rial

Jonathan M. Lees

Donna Surge

Erika Wise

Tamlin Pavelsky

ABSTRACT

Elizabeth Piccard Reischmann: Self organization of nonlinear Paleoclimate and climate
oscillators
(Under the direction of José A. Rial)

Synchronization is a widespread phenomenon in nonlinear, physical systems. It describes

the phenomena of two or more weakly interacting, nonlinear oscillators adjust their natural

frequencies until they come into phase and frequency lock. This behavior has been observed in

biological, chemical and electronic systems, including neurons, fireflies, and computers, but has

not been widely studied in climate. This thesis presents a study of several major examples of

synchronized climatic systems, starting with ice age timings seemingly caused by the global

climate's gradual synchronization to the Earth's 413kyr orbital eccentricity band, which may be

responsible for the shift of ice age timings and amplitudes at the Mid-Pleistocene transition. The

focus of the thesis, however, is centered the second major example of stable synchronization in

the climate system: the continuous, 90 degree phase relationship of the polar climate signals for

the entirety of the available ice record. The existence of a relationship between polar climates has

been widely observed since ice core proxies became available in both Greenland and Antarctica.

However, my work focuses on refining this phase relationship, utilizing it's linear nature to apply

deconvolution and establish an energy transfer function. This transfer function shows a distinctly

singular frequency, suggesting that climate signal is predominately communicated north to south

with a period of 1.6kyrs. This narrows down possible mechanisms of polar connection

dramatically, and is further investigated via a collection of intermediate proxy datasets and a set

of more contemporary, synchronized, sea surface temperature dipoles. While the former fails to show any strong indication of the nature of the polar signal due in part to the overwhelming uncertainties present on the centennial and millennial scales, the latter demonstrates a large set of synchronized climate oscillations exist, communicate in a variety of networks, and have a direct connection to larger climate patterns (in this case, precipitation anomalies). Overall, this thesis represents a clear advance in our understanding of global climate dynamics, presents a new method of climate time series analysis, evidence of 16, stable, synchronized sea surface temperature dipoles, and provides a detailed sediment core database with explanations of age model limitations for future investigation.

To: My family and my friends
And especially my cats
For their patience and love.

ACKNOWLEDGMENTS

TABLE OF CONTENTS

LIST OF TABLES

LIST OF FIGURES

.

CHAPTER 1: AN INTRODUCTION TO SYNCHRONIZATION IN THE CLIMATE SYSTEM

1.1 Introduction

Synchronization is a fundamental, nonlinear phenomenon and a basic mechanism of self-organization of complex systems. It was first observed in the XVII century by Christiann Huygens while studying two early pendulum clocks hanging from a single beam. The clocks' initially different phases and frequencies slowly drifted until they achieved full phase and frequency lock, oscillating in-phase until the resulting positive feedbacks overwhelmed the system and forced the clocks out of phase once again. This coupling is attained through the very weak exchange of vibrational energy through the beam created by the impacts of the pendulum maximums, which in turn result in positive and negative feedbacks. Since this initial discovery, synchronization has been observed in a wide range of fields, including physics, chemistry, biology, electrical engineering and recently in climatology, and has been widely explored mathematically [Tziperman et al., 2006,; Pikovsky et al., 2002; Balanov et al., 2009; Rial, 2012; Gonzalez-Miranda, 2004; Oliveira and Melo, 2015]. In biology, this method of self-organization has been used to characterize the actions of neurons leading to seizures, heartbeats responding to poetry reading, and even firefly rhythms [Strogatz, 2003]. The study of synchronization in the climate system, on the other hand, has only just begun, largely due to the characteristics of climate data series and the complexity of the system, both of which complicate the study of isolated signals in reproducible environments. Two major examples of long term, stable synchronized systems in the climate system have been established, and are presented here. The first is an example of forced, or master-slave, synchronization wherein the 413-kyr orbital

eccentricity (which modulates the amplitudes of the orbital 100-kyr eccentricity and precession) phase locked, frequency entrained, frequency modulated, and amplified [Pikovsky and Kurths, 2002; Rial, 2012] the free oscillations of the climate system during the past 1.2 Myr, the discovery of which was the basis of the work in this thesis. Prior to this work, the study of phase relationships in the climatic signals was performed on modern, directly observational signals. While some uncertainty is definitely present in the LR04 stack, tuned or un-tuned, for reasons thoroughly discussed in Chapter 4, on the scale of 100kyr periodicities, these uncertainties are not significant.

The second an example of small-world synchronization, wherein nonlinear ocsillators are able to pass information between each other for two or more oscillators until all oscillators achieve stable phase and frequency relationships. In this case, the major oscillators are the polar ice sheets, passing information via the intermediate earth, ocean and atmosphere, resulting in a stable, 90° phase relationship between the polar, $\delta^{18}O$ climate proxy records over the past 100kyrs. Both examples demonstrate the key characteristics of synchronization: nonlinear, oscillating signals coming into gradual phase and frequency lock as the systems interact. Moreover, the presence of synchronization in these systems implies a simplified method of understanding the dynamics of ice ages and the global climate system, with my own contribution to both papers having focused on model simulations and model parameter stability in simulating the data's behavior.

Part 1.2: Amplitude Modulation of the Global Climate System via the 413-kyr Orbital Eccentricity Cycle.[1]

Since about 1.2-1.3 million years ago, glacial–interglacial cycles have had a period of about 100,000 years. Prior to this point, the cycles had lower amplitudes and an approximately 40,000 periodicity [Clark et al., 2006]. This shift does not correspond to a known change in the physical features of the globe, and is known as the mid-Pleistocene transition. Both of these cycles have nearly corresponding Milankovitch cycles, i.e., cycles of changes in orbital features. However, the magnitude of the change in incoming solar radiation due to the 100kyr cycle—insolation—at this timescale is small, and therefore difficult to reconcile with the amplitude of the glacial cycles [Lisiecki, 2010; El-Kibbi and Rial, 2001; Huybers and Wunsch, 2005; Raymo, 1997; Berger et al., 2005; Clark et al., 2006]. As mentioned above, our group has focused on synchronization as a climate organizing mechanism. Using spectral analyses aided by a numerical model, we found that the climate system signal as recorded in the LR04 prxy stack synchronized to the 413,000-year eccentricity cycle about 1.2 million years ago and has remained synchronized ever since. This synchronization allows for a nonlinear transfer of power and frequency modulation that increases the amplitude of the 100,000-year cycle. We conclude that the forced synchronization can explain the strong 100,000-year glacial cycles through the alignment of insolation changes and internal climate oscillations.

The search for synchronization in this dataset was motivated by previous work done by Rial [1999] which noted that untuned climate proxy records show a frequency [Van der Pol,

---

[1]This section was published in Nature Geoscience. The original citation is: Rial, José A., Jeseung Oh, and Elizabeth Reischmann. "Synchronization of the Climate System to Eccentricity Forcing and the 100,000-year Problem." *Nature Geoscience* 6, no. 4 (2013): 289–293.

1930; Lathi and Ding, 2009]. The LR04 time series specifically shows that the 100kyr glacial cycles are modulated by a 413kyr cycle, i.e. orbital eccentricity (Fig. 1). In the frequency domain, multi-taper [Ghil et al., 2002] spectra of both the untuned LR04 data and $Fm(t)$ (a simple model approximating the LR04 stack, see Methods) also have the side-lobe frequencies 1/125, 1/77, 1/64 and 1/55 kyr. These side lobes are spaced around the ~ 1/100-kyr peak at spectral distances equal to integer multiples of 1/413 kyr, once again indicating that this is our modulating signal [Rial, 1999; Van der Pol, 1930,; Lathi and Ding, 2009].

In order to better test this, I used a simplified climate model (see Supplementary Information) that was originally designed to simulate the time evolution of global ice volume, atmospheric CO2 and ocean temperature [Saltzman, 2002]. Supplementary Fig. S4 shows that besides reproducing the characteristic sawtooth waveform of the palaeoclimate records, forcing the model with only the 413-kyr component of eccentricity (Fig. 1d) produces frequency modulation of the model's ~ 100-kyr band that closely fits (within time uncertainty) the timing of glacial terminations [Raymo, 1997].
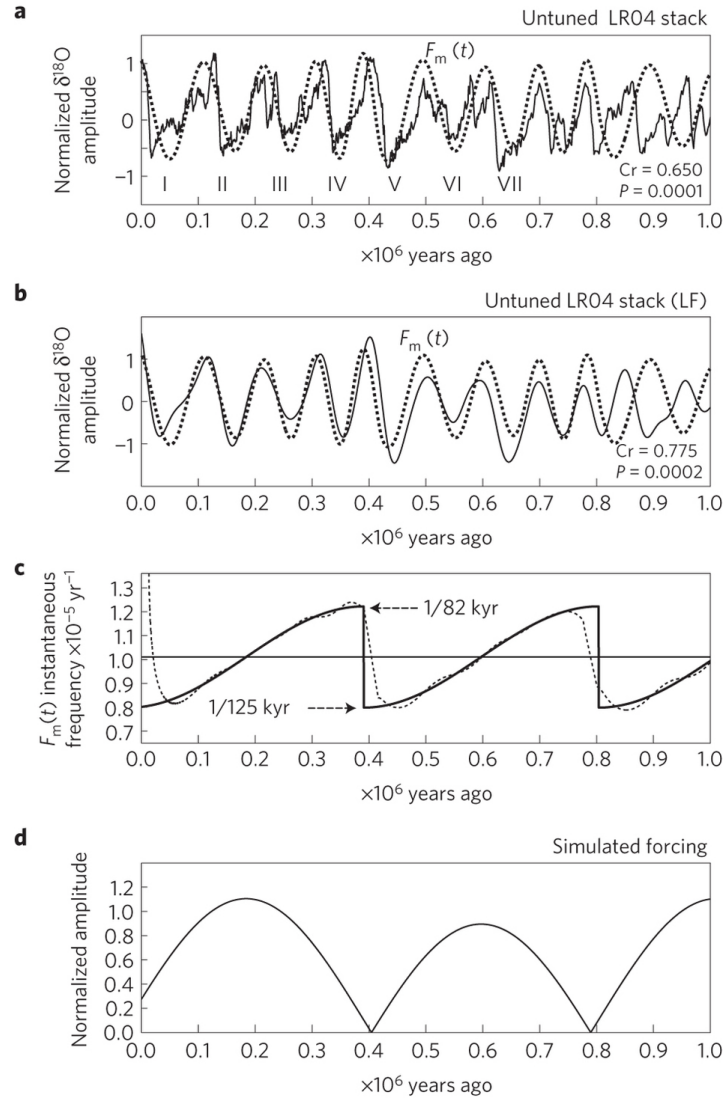
Figure 1.1: a, A frequency-modulated sinusoid Fm(t) fits reasonably close the ~ 100-kyr glaciations of the untuned LR04 stack. **b**, Comparison of Fm(t) to LR04 low-pass-filtered to attenuate periods shorter than 50 kyr. Correlation coefficients and associated P values are calculated for the 0.8–0 Myr ago interval using standard numerical algorithms. If $P<0.05$ the correlation coefficient is statistically significant. **c**, The calculated frequency deviation is consistent with the observations. The continuous curve is the analytic result and the dotted curve is the numerical approximation using the method in Gabor [1946] **d**, The simulated 1/413-kyr eccentricity forcing hm(t) = $\|\cos(\omega \text{m}t - \phi\|)$ (see Methods).

Frequency modulation in the paleoclimate also implies the existence of a modulator, which is also known as the intelligence of the modulated system. This intelligence, calculated via the Gabor method of taking the envelope of the rectified time dericatived of the low-pass filtered 5-million-year-long LR04 stack, should represent a proxy for the climate's response to forcing (shown in Figure 2, details of the calculation in Methods [Lathi and Ding, 2009] from a modulated time series.
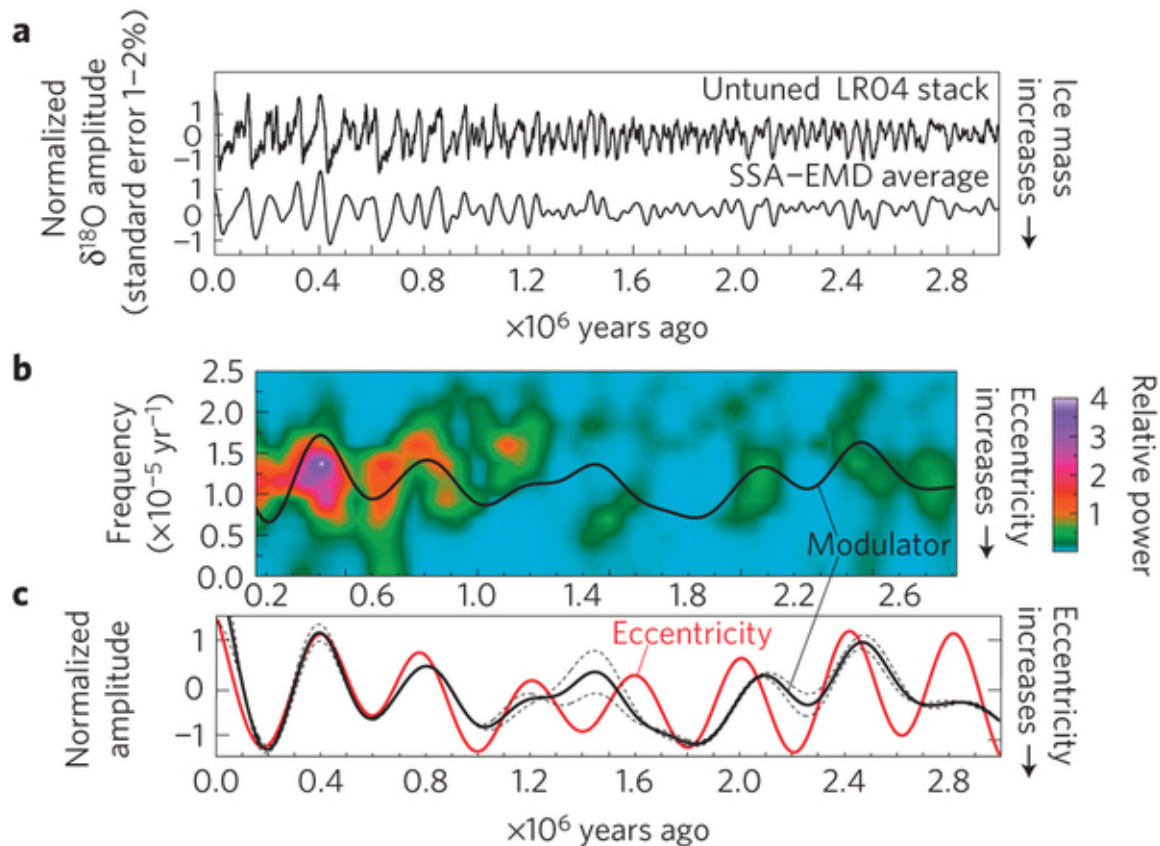
Figure 1.2: **The modulator. a**, Time series and low-pass-filtered untuned LR04 stack. The filtered trace is the average of singular spectral analysis (SSA) and empirical mode decomposition (EMD; see Methods). **b**, The untuned LR04 spectrogram (moving window Fourier transform; window length 300 kyr, sliding window length 30 kyr, low-pass corner at 0.020 kyr−1). **c**, The modulator extracted from an ensemble of filtered LR04 time series (see Methods and Supplementary Figs S6–S8) compared to the 413-kyr component of eccentricity. The continuous line

is the mean and dashed lines are ±1σ . The modulator function represents the forcing as seen from the climate system's reference frame. All calculations are performed using the complete 5-Myr record.

To examine the details of the evolution of the forced synchronization between the modulating solar forcing and the modulated climate response, we looked to the phase difference [Pikovsky et al., 2002; Huang et al., 1998; Gabor, 1946] (Fig. 3). The phase difference appears to gradually stabilize at 0 from the period of 5myr ago to 1.2myr ago (Figs 2c and 3). The phases then appear to lock and remain so until the most recent measurements (Supplementary Figs S9 and S10). Further, the stabilization around 1.2 Myr ago is statistically significant, as the null hypothesis of circular uniformity of phase can be rejected in the interval 1.2–0 Myr ago, but accepted for earlier times (see Methods).
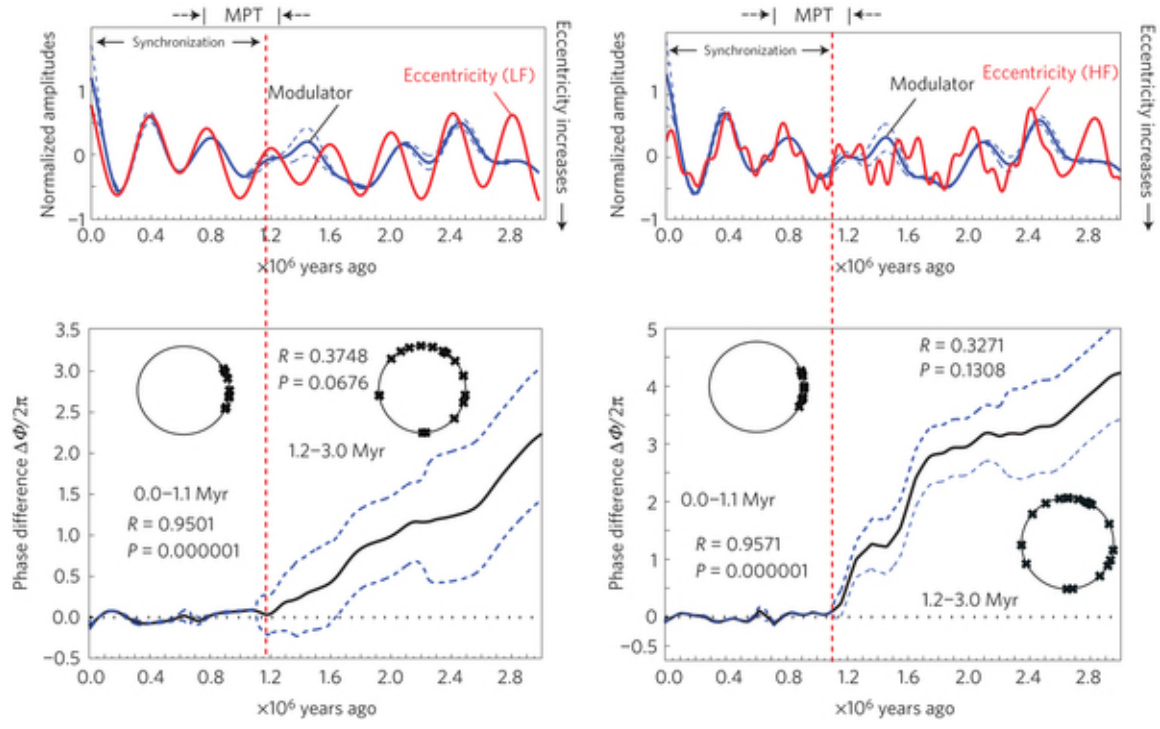
Figure

1.3. Theoretical low-frequency (period > 300 kyr) and high-frequency (period > 80 kyr) orbital eccentricity compared with the modulator (top). Their phase difference (see Methods) decreases monotonically (bottom) with time until phase locking occurs about 1.2–1.1 Myr ago. Mean value (solid) ±1σ (dashed) of are shown. In the insets it is shown that the Rayleigh R test and P values (see Methods) reject the null hypothesis of phase circular uniformity in the 1.2–0 Myr ago interval, so that the abrupt change in $\Phi(t)$ at ~1.2 Myr ago is statistically significant. The LR04 time series and the 100-kyr eccentricity have previously been shown to be phase locked in the 1.2–0 Myr ago interval using a wavelet approach.

Further evidence of synchronization is seen on close inspection of Figs 2, 3 and 4, which show that synchronization of the modulator to the 413-kyr eccentricity occurs simultaneously with increased signal power in the ~ 100-kyr band of the LR04 stack. This energy transfer happens because synchronization forced the climate system's internal feedbacks to warming or cooling at the same pace long-period insolation changes induced by the 413-kyr eccentricity

8

were increasing or decreasing, resulting in frequency-modulated internal ~ 100-kyr cycles reaching unprecedented amplitudes during the late Pleistocene.
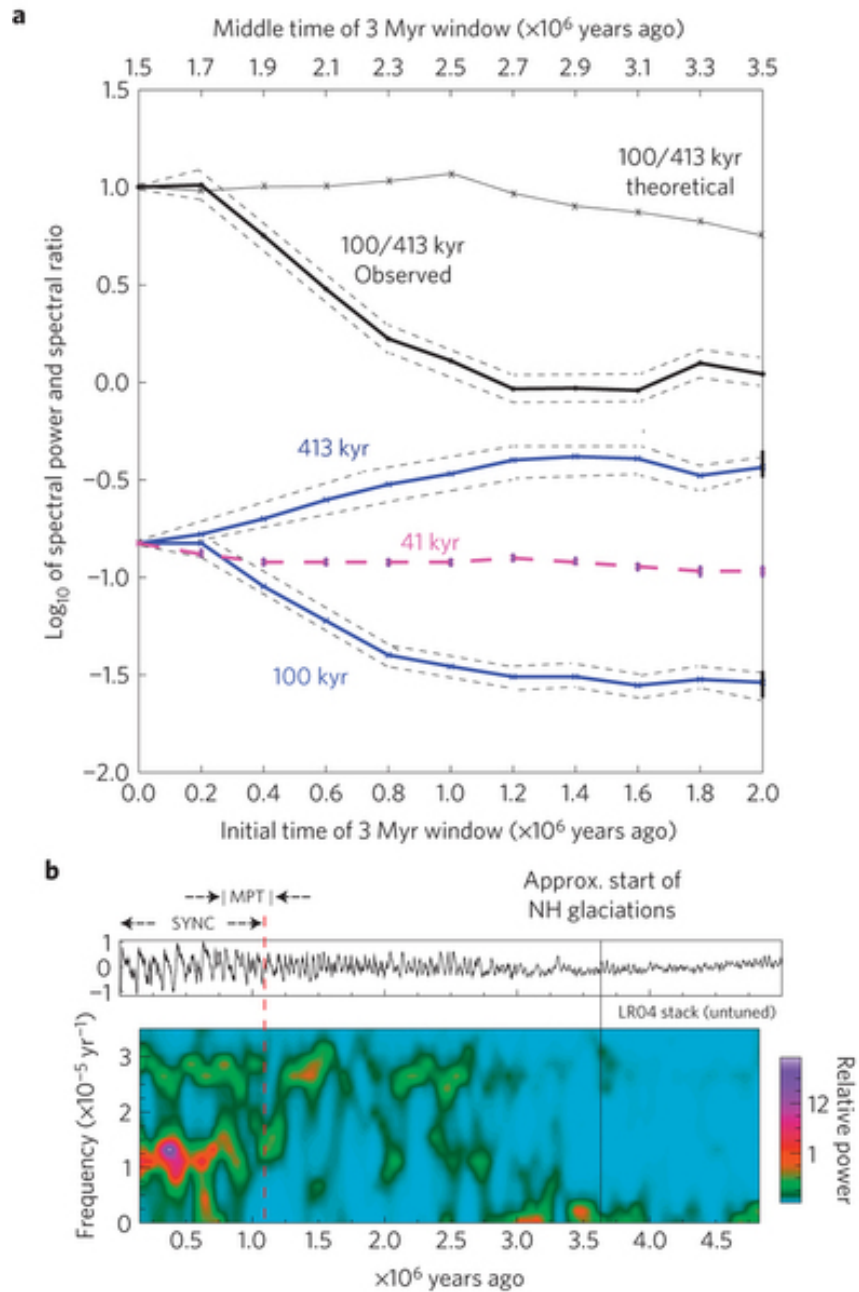
Figure 1.4. **a**, Spectral power nonlinearly transferred from the 413-kyr component to the 100-kyr component of eccentricity. The graphs for the 41-, 100- and 413-kyr bands are normalized to have the same (but otherwise arbitrary) value at present. The spectral ratio 100/413 kyr is shifted upwards for clarity. Dashed lines are ±1σ

9

estimates of spectra measurement error. **b**, Spectrogram showing the time evolution of the power in the 1/41-, 1/100- and the 1/413-kyr frequency bands. The higher resolution shows details missed by the long-term trends in **a**.

One other event that strongly suggests energy transfer across frequencies is the relatively brief period of nonlinear resonance that, as suggested by Fig. 2c, happened when $\Delta \Phi(t) \approx 0$ and frequency detuning $\Delta \Omega \approx 0$ occurred simultaneously about 400 kyr ago (see Methods). That is, the time when the spectrogram in Fig. 2b records the largest power in the signal lasting not longer than ~ 20 kyr. The warming trend of low eccentricity reinforced by internal feedbacks working in unison with the forcing rapidly shrunk the ice sheets, resulting in the high-frequency ($\sim 1/82$ kyr) unusually warm interglacial episode at marine isotope stage 11 (MIS11; Fig. 2). We can infer that the amplitude of the response became strong enough to nonlinearly shift the system away from resonance, which explains the brevity of the resonant interval. Similar astronomical circumstances (low eccentricity) also occurred at ~ 0.8 Myr ago and are happening today, but both then and now, as seen in Figs 2c and 3, the instantaneous frequencies are distinct (within time uncertainty), and $\Delta \Phi(t) \neq 0$.

Transfer of energy from the 1/413- to the 1/100-kyr bands is apparent in Fig. 4a. From 5 Myr ago to ~ 1.2 Myr ago the ratio of peak spectral power at 1/100 kyr to that at 1/413 kyr remained almost constant, but starting around ~ 1.2 Myr ago the ratio began to rapidly increase because power in the $\sim 1/100$-kyr band increased nearly at the same time and the same rate as power in the $\sim 1/400$-kyr band decreased. One mechanism that probably produces this result is amplitude modulation by the 1/413-kyr band transforming into frequency modulation of the $\sim$ 1/100-kyr band (Fig. 1 and Supplementary Figs S1 and S2–S4).

In contrast, the spectral power in the 1/41-kyr (obliquity) band increased slowly from 5 Myr ago, reached a maximum around 1.2 Myr ago and then remained nearly constant [Lisieki and Raymo, 2007] until the present time. It has been suggested that the 41-kyr obliquity forcing paces the glacial terminations [Huybers and Wunsch, 2005], but neither the simple function Fm(t) (Fig. 1 and Supplementary Fig. S1) nor the nonlinear ice volume model (Supplementary Fig. S4) required 41-kyr obliquity forcing which, accordingly, does not seem necessary to account for the timing of the glacial terminations. Further, frequency modulation does not require the climate state to arbitrarily select skipping one rather than two obliquity beats before deglaciation takes place [Huybers and Wunsch, 2005], while forced synchronization explains the MPT without further assumptions.

In the foregoing we have assumed that there exist natural frequencies of oscillation in the climate system close to those of the orbital forcing, and thus master–slave synchronization is possible [Gonzalez-Miranda, 2004]. However, even if this is true, there is no direct way to confirm it. Yet, there is compelling evidence of a natural frequency in the ~ 1/100-kyr band [Nie, 2011], and a 500-kyr oscillation [Nie et al., 2006] in benthic carbon isotopic records. The former supports our main assumption and the latter oscillation is explained by our proposed mechanism as probably arising from the forced synchronization of a natural 500-kyr oscillation by the 413-kyr eccentricity forcing (see Supplementary Figs S11 and S12). As far as we know, only nonlinear synchronization predicts the possible appearance of frequencies near the main forcing frequency in climate records in general.

There is also suggestive evidence for synchronization in the time evolution of the modulator's instantaneous phase ΦC: Supplementary Fig. S9 shows that the phase of the modulator, basically constant before 4 Myr ago, begins to approach the phase ΦF of the eccentricity forcing around the start of the Northern Hemisphere Plio–Pleistocene glaciations at ~ 3.6 Myr ago [Lisiecki and Raymo, 2007]. From this time on, the eccentricity forcing seems to drive the climatic response, because the modulator's phase approaches the eccentricity's phase in a nearly smooth and apparently deterministic fashion until both synchronize around 1.2–1.1 Myr ago and both share the same frequency (1/413 kyr). In fact, the instantaneous frequency of the modulator (given approximately [Gabor, 1946] by the time-averaged slope of ΦC) increases from ~ 0 at 5 Myr ago to ~ 1/413 kyr at 1.2 Myr ago. Consistent with these observations, the modulator is of low frequency and low amplitude before the start of the Northern Hemisphere glaciations (see Supplementary Fig. S10).

Thus, the eccentricity forcing seems to capture the climate system's emerging oscillation starting as early as 3.6 Myr ago. How such capture may develop as the phases become close enough is reproduced by numerical experiments in Supplementary Fig. S11. This theoretical result shows that if the natural frequencies of oscillation of the climate system are within 10–20% of the forcing period, synchronization occurs even for very small forcing amplitude and can produce a power gain (ratio of the synchronized power to the forcing power) of 300–700% and greater for small detuning. Thus, as the climatic response synchronizes with the eccentricity forcing, the climate's oscillations become more energetic because of the nonlinear transfer of

power (Fig. 4), which results in an increased bandwidth of the ~ 100-kyr glacial cycles due to frequency modulation (Supplementary Figs S2 and S4).

Synchronization allowed energy from the sun to flow into or out of the climate system at the same time internal feedbacks were warming or cooling it, resulting in unprecedentedly large climate fluctuations that powered the great Pleistocene glaciations (a process akin to resonance of a forced linear oscillator). Forced phase synchronization, which is still occurring, started 1.2 Myr ago, and culminated at the time of the MIS11 (~ 0.4 Myr) with a brief period of nonlinear resonance. During synchronization, the 1/413-kyr component of eccentricity forced the frequency modulation of the ~ 1/100-kyr band, evidenced by depleted spectral power at 1/413 kyr and the presence of power at frequencies absent in the spectrum of the orbital forcing. Today resonance has faded but frequency modulation persists, driving the ~ 1/82–1/125-kyr frequency deviation that paces the timing of the major glacial terminations [Raymo, 1997].

Methods:

Master–slave synchronization.

The condition for (phase) synchronization can be expressed as

$$|\Delta\Phi(t)| = |m\Phi_F(t) - n\Phi_C(t)| \leq \text{constant}$$

In the present context ΦF and ΦC are the phases of the astronomical forcing and climatic response respectively, and *m* and *n* are small integers [Pikovsky et al., 2002; Balanov et al., 2009]. Forced (also phase) synchronization is an adjustment of the forced oscillator's natural frequencies to those of the orbital forcing and can be described in terms of phase locking and frequency entrainment (*p/q* frequency lock, where *p* and *q* are small integers) [Pikovsky et al., 2002; Balanov et al., 2009]. In terms of the instantaneous phases, frequency lock occurs when Δ $\Omega = \langle p(\mathrm{d}\Phi F/\mathrm{d}t) - q(\mathrm{d}\Phi C/\mathrm{d}t)\rangle = 0$, which with $p = q = 1$ seems to have happened

13

simultaneously with $\Delta\Phi(t) = 0$ around the MIS11 time (Fig. 2c), an event described here as nonlinear resonance. The time series in Figs 2 and 3 show that the instantaneous phase and its derivative (instantaneous frequency) are nearly the same at 400 kyr ago, even allowing for age uncertainty, so it is not improbable that they are resonating. The instantaneous phase is computed using the standard analytic function procedure [Gabor, 1946]. The $\langle\ \rangle$ brackets denote a time average so that $\Delta\Omega$ is the difference in mean frequencies [Balanov et al., 2009].

Frequency modulation.

Clear evidence of frequency modulation is usually difficult to demonstrate unless the proxy records are astronomically untuned[8]. Tuning to the astronomical clock destroys frequency or phase modulation information (see Supplementary Fig. S2) and implies unwarranted [El-Kibbi and Rial, 2001; Clark et al., 2006; Saltzman, 2002; Rial, 1999; Pisias and Moore, 1981; Paillard, 1998; Muller and McDonald, 2000; Tziperman et al., 2006] linear relationships (proportionate amplitudes frequencies and phases) between external forcing and response.

The signal Fm(t) introduced in Fig. 1 (see also Supplementary Fig. S1) is

$$F_m(t) = A(t)[1 - ah_m(t)]\cos[\omega_c t + \varphi - \varepsilon h_m(t)]$$

$$\text{With } h_m(t) = \||\cos(\omega_m t - \psi)\|| \tag{1}$$

Equation (1) is a physically plausible mathematical form for the oscillation of the ice sheets [Rial, 1999], exhibits frequency deviation (Fig. 1c) in the same range (1/82–1/125 kyr) as the untuned proxy record, predicts a variable duration for each glaciation consistent (within age uncertainty) with the timing of glacial terminations [Raymo, 1997], and its frequency modulation index is almost identical to that estimated from the observations. Equation (1) has the form of a frequency-modulated solution to the Mathieu differential equation [Van der Pol, 1930] that can describe frequency modulation of the ice sheets' oscillation. To correctly simulate the

eccentricity waveform the modulating frequency is $\omega m/2\pi$ = 1/826 kyr, so that the rectified

cosine $h\text{m}(t)$ has the correct 1/413-kyr frequency of the eccentricity cycle. The phase ϕ is set

equal to the actual value (Fig. 1d). $\omega c/2\pi$ is a natural oscillation frequency (carrier) of the

climate system, assumed to be ~ 1/100 kyr. $A(t)$ is a slowly varying negative linear ramp

constructed ad hoc to attenuate the signal for early times. The frequency modulation index, ε =

$\Delta\omega c/\omega m$, is the ratio of the mean frequency deviation of the carrier (1/82–1/125)/2 to the

modulating frequency (1/826) [Rial 1999; Lathi and Ding, 2009]. For a rectified cosine of

frequency 1/826 kyr the modulation index ε should be ~ 1.73, close to the calculated value ε

= 1.75 that produces the highest correlation coefficient (0.775) between $F\text{m}(t)$ and the filtered

LR04 stack over the past 0.8 Myr. The amplitude modulation index a = 0.25 is consistent with

weak amplitude modulation. Besides a, the constant phase ϕ is the only other adjustable

parameter in equation (1).

Extracting the modulator from LR04 stack.

The modulating function or modulator (Fig. 2b,c) of the LR04 stack is the envelope of

the rectified time derivative of the low-pass-filtered record [Lathi and Ding, 2009]. An ensemble

of modulators was obtained from low-pass realizations of the LR04 record as the filter's corner

frequency varied from 0.02 to 0.03 kyr^{-1} in steps of 0.001 kyr^{-1} (see Supplementary Figs S6–

S8). The mean value and ±1 σ curves are plotted in Figs 2c and 3. Adaptive methods such as

singular spectrum analysis [Ghil et al., 2002] and empirical mode decomposition [Huang et al.,

1998] were used to make sure that linear filtering does not distort the frequency/phase

composition of the signal.

The instantaneous phases of eccentricity and modulator (Fig. 3 and Supplementary Figs S6 and S9) were calculated according to ref. 25, whereby the instantaneous phase of a one-component time function $x(t)$ (the modulator and eccentricity are very nearly one-component functions) is obtained by calculating the inverse tangent, $\tan^{-1}\{H[x(t)]/x(t)\}$, where $H[\cdot]$ is the Hilbert transform [Bracewell, 1986] of its argument. The Rayleigh R test [Berens, 2009] was performed and the null hypothesis of circular uniformity rejected for the flat (0–1.1 Myr) branches ($R>0.5$) and accepted on the 3–1.2 Myr BP branches ($R<0.5$) of the phase difference plots.

Part 1.2: Synchronization of the Polar Climates Over the Last Ice Age[2]

1. Introduction

Having established the roll of forced synchronization in the Mid Pleistocene Transition, we now turn our focus to the synchronization of the ice sheets. The climate records seen in the polar ice cores can also be characterized as nonlinear, complex, oscillating systems, with periods of abrupt warming separated by abrupt cooling. Here, we demonstrate the effectiveness of modeling the polar climates as synchronized, nonlinear oscillators, using the same ice volume model (Saltzman, 2002) used in the previous section, only here we use two coupled systems, each of which represents one polar climate as simple Van der Pol oscillators.

Research identifying and modeling the polar climates' similar dynamics can be summarized as follows: "The EPICA Community Members (2006) identified a linear relationship between the stadial intervals at the poles during the MIS3 interval 50 ka–30 ka (1 ka = 1000 years ago). Prior to this, Crowley had put forward the basic bipolar hemispheric seesaw hypothesis (Crowley, 1992; Broecker, 1998) as an explanation of how the abrupt warming episodes in the North Atlantic lead to the beginning of cooling episodes in Antarctica, namely via polar climate communication through meridional (equatorially asymmetric) heat transport and North Atlantic deep water (NADW) production. Blunier et al. (1998) and Blunier and Brook (2001) built on this idea, demonstrating that events in Greenland's climate follow those in Antarctica by about 1–3 ky (1 ky = 1000 years) and that this is due to the ocean controlling the climate at both poles. Hinnov et al. (2002) studied the specific connection between the Byrd and GISP2 records' inter-hemispheric anti-phasing (180° phase shift) of the

Dansgaard–Oeschger (DO) oscillations over the 10–90 ka interval. Even more recently, Steig (2006) reported a $\pi/2$ phase shift between the polar climates, seen by analyzing high-resolution records from EDML (Antarctica) and NGRIP (Greenland) cores. Barker et al. (2009) then published data from the South Atlantic which demonstrated the existence of rapid but opposite temperature changes occurring at the same time as those documented in the north and proposed a link between the DO oscillations in the Arctic and the sub-Antarctic temperature variations. In a follow up study, they used Crowley's simple, conceptual bipolar seesaw model to forecast the unknown Greenland record using the 800 ky record of Antarctica (Barker et al., 2011), though the lack of actual Greenland records beyond ~120 ka means that they were unable to validate their results. Finally, in response to this, Rial (2012) proposed the nonlinear phase synchronization of the millennial-scale polar climates fluctuations during the last glaciation as an explanation for the apparent teleconnection between the Polar Regions."

These studies, especially the work of Rial, were the basis of this investigation. We sought to quantify the strength and robustness of polar synchronization using a data adaptive decomposition technique, surrogate data tests, and long-term methane-matched age models when possible, providing a more complete characterization of the polar connection and behavior of the polar climates as oscillators. The approach demonstrated in this paper uses the modified Saltzman model to reproduce the 100 ky Greenland ice core record (GRIP). We show that bi-directional, or mutual, phase synchronization affects these millennial cycles, but does not appear overlap with the long periods discussed in the previous section, i.e. those dominated by the Milankovitch forcing.

To clarify, the term synchronization or phase synchronization refers to frequency entrainment and phase lock (i.e. a constant phase difference), and is not the opposite of *asynchronous* as used by some authors to refer to the polar climate being locked out of phase (Blunier et al., 1998; Stenni et al., 2010). It is also unrelated to the synchronizing of age models via methane records from both Polar Regions (e.g., Blunier and Brook, 2001). This last technique allows for relative ages between polar samples to be constrained, and is what allows us to compare the instantaneous phases of the southern Byrd and northern GRIP (details will be explained later with Fig. 5).
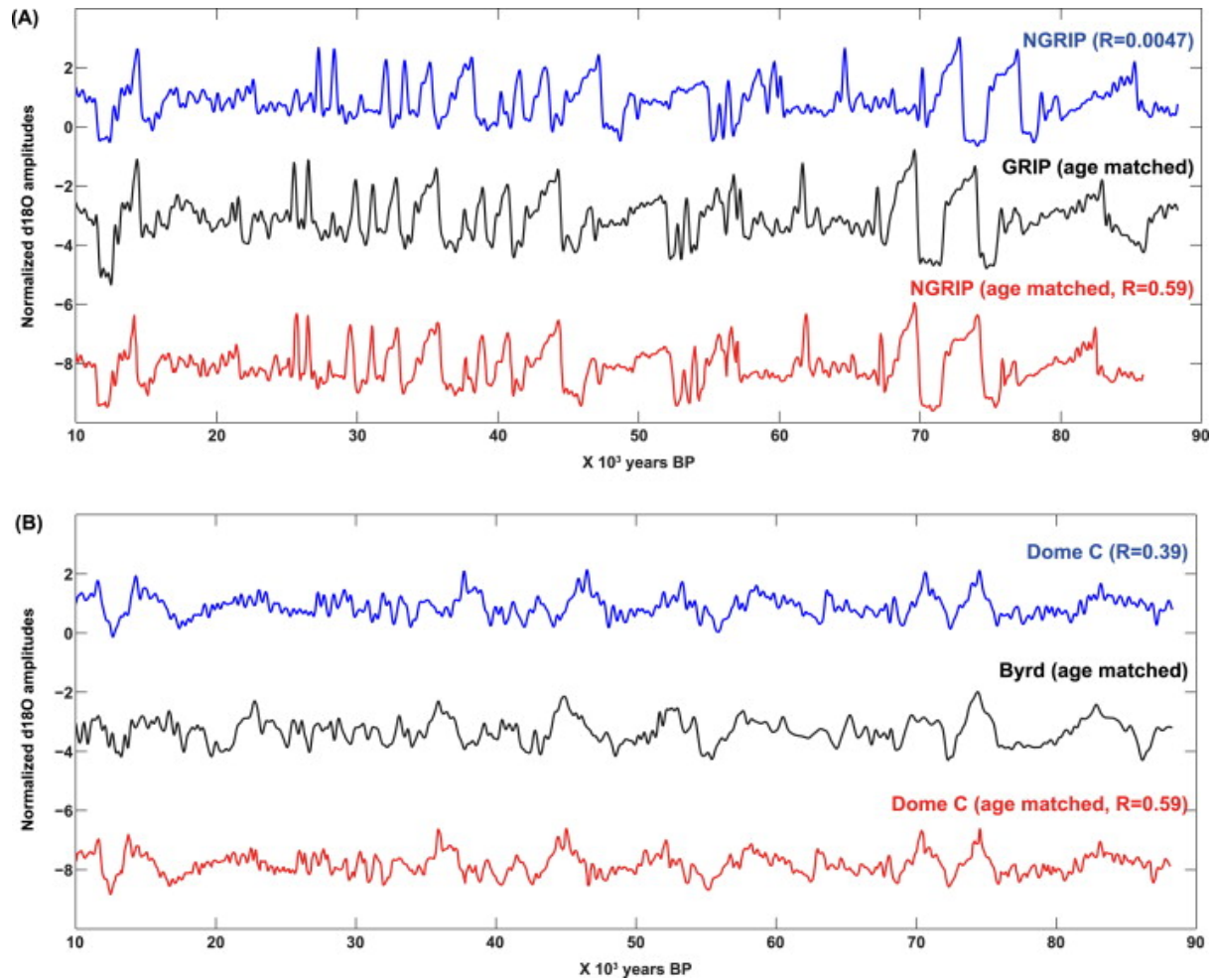
Fig. 1.5.

(A) Age model matching between NGRIP (blue: before age matching, red: after age matching) and GRIP (black) records using GRIP for standard. Since GRIP and Byrd age models have been matched previously using methane records from both poles (Blunier and Brook, 2001) this allows to tune NGRIP to GRIP (see text for details). Correlation coefficient (R) between NGRIP and GRIP records increases from 0.0047 to 0.59 by matching age model of NGRIP and GRIP. (B) Age model matching of EPICA Dome C to the Byrd record using the same approach. This results in the age model match of NGRIP and Dome C. Note that the correlation of NGRIP and GRIP before the match (0.0047) and that of Byrd and Dome C before the match (0.39) are different because of uncertainties in the original age models.

2. Polar synchronization paradigm

2.1. Polar synchronization

As mentioned earlier, in order for synchronization to be established, phase lock must be present between two or more, interacting time series. Note that the phase lock can either be in-phase, anti-phase, or an arbitrary, constant phase. For the polar regions, all millennial scale frequency components in the signal are $\pi/2$ phase locked, meaning each of a pole's frequency components is shifted by one-fourth of its period to align with the other. Thus time series pairs like NGRIP-DomeC or GRIP-Byrd can be formally described as approximate Hilbert transform pairs (Bracewell, 1986; see Appendix A).

Being able to identify any type of synchronization in the ice cores is far from simple, though, as each pole is affected by different factors, there are decadal to centennial scale uncertainties in the dating, and their interactions are easily obscured. However, in spite of these problems, our analysis suggests that a few simple rules controlling the relationship between polar climates do exist.
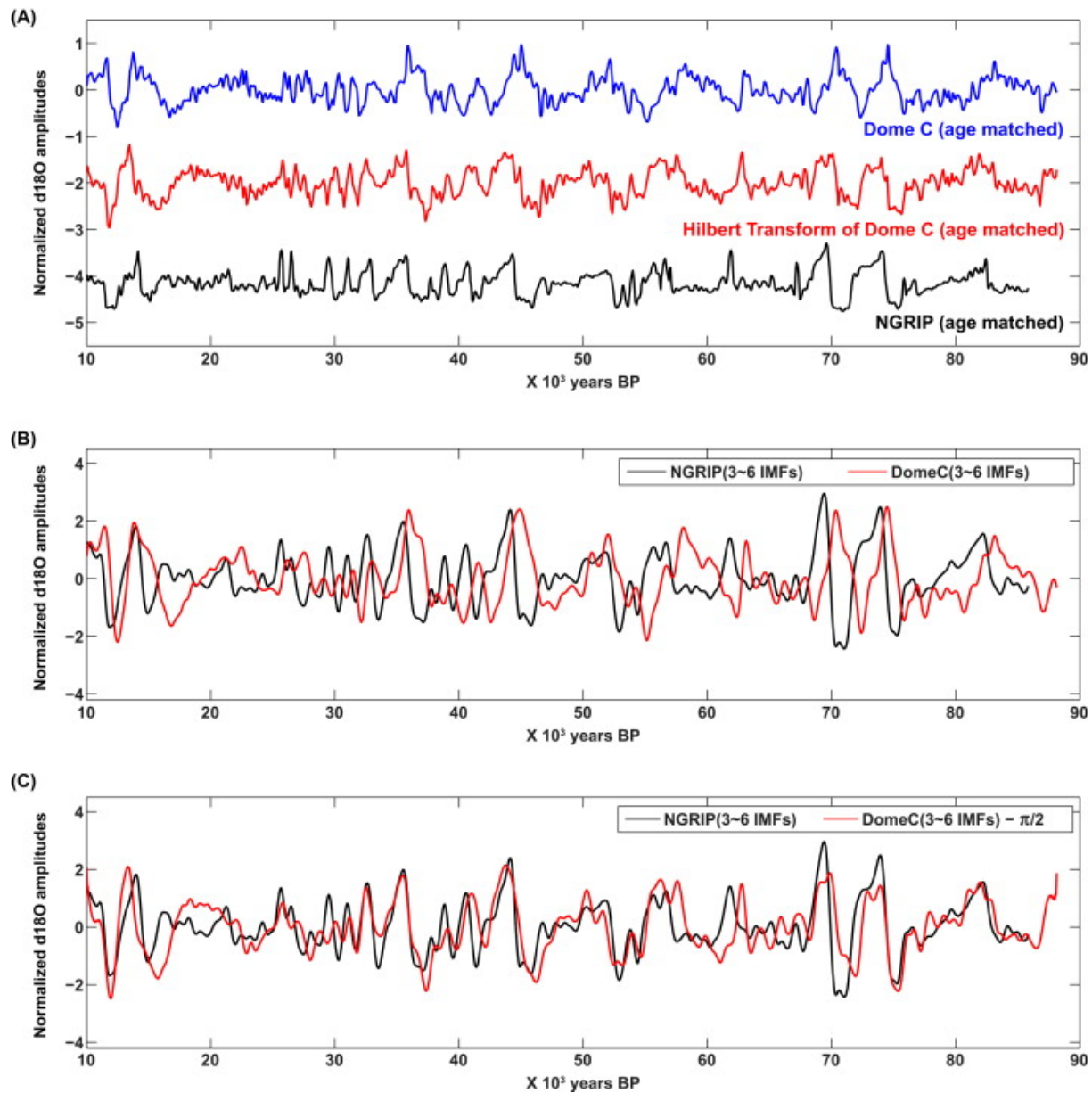
Fig. 1.6.

(A) Polar synchronization ($\pi/2$ phase lock) between the North and South climate proxy records from Greenland (NGRIP) and Antarctica (Dome C). The age models of Dome C and NGRIP records are matched, i.e., they are tuned each other (see text for details). The Hilbert transform (HT) of Dome C correlates with NGRIP, which implies that the records of the Polar Regions are synchronized. (B) 3rd ~6th Intrinsic Mode Functions (IMFs) from NGRIP (black) and Dome C (red) records. Here we use the Empirical Mode Decomposition (EMD) (Huang et al., 1998) which provides Intrinsic Mode Functions (IMF) each of which is a mono-component. (C) Same as (B) but with Dome C signal transformed by $-\pi/2$ phase shift (Hilbert transform). The HT is applied to each mono-component

22

signal, a procedure equivalent to a Hilbert Huang Transform (HHT) (Huang et al., 1998). To obtain the phase shifted signal, we applied HHT (equivalent to a $-\pi/2$ shift) to the Dome C record with integral limits from past to future (see Appendix 1).
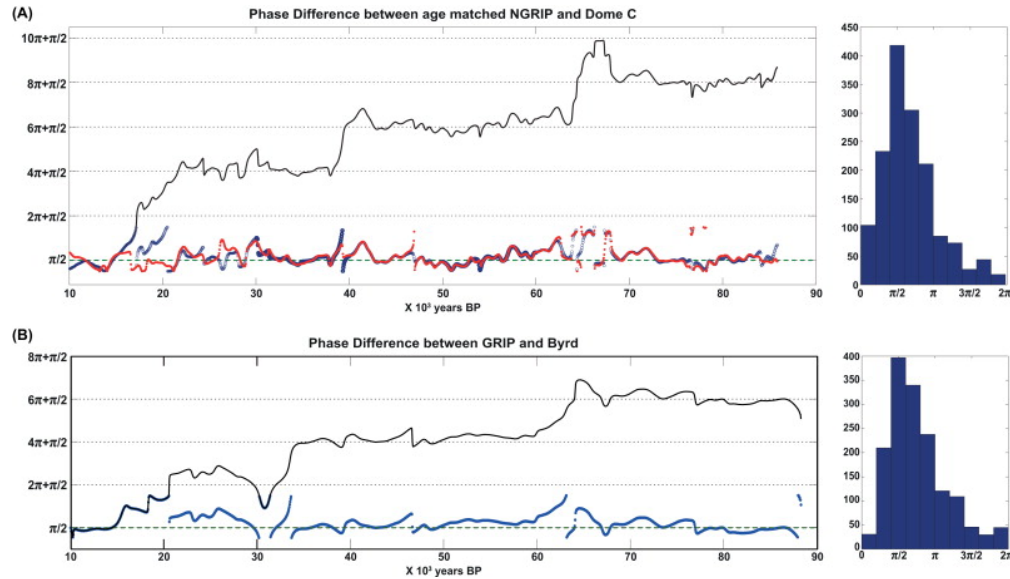
Fig. 1.7.

(A) Phase difference between age matched NGRIP and Dome C records at millennial scale. Phase differences are calculated from 3rd~6th IMFs shown in Fig. 1.6(B). Once the age models are matched, the phase differences between time series from NGRIP and Dome C show that the two series are synchronized. 2π jumps are expected to occur due to noise, or external forcing. Blue circles are shown after removing 2π shifts from the original phase differences (black line) show that the differences are bounded at $\pi/2$, which is a condition for phase synchronization between two coupled nonlinear oscillators. Red dots describe the phase differences calculated using same frequency band data linearly filtered. (B) Like in (A) for GRIP and Byrd. The histograms show the distribution of phase difference (modulo 2π).

2.2. Transforming one polar climate into the other

The quantified phase difference calculations shown in Fig 1.5-7 require precise instantaneous phase calculations, which is a non-trivial process. To begin, as mentioned earlier, a set of relative dates are established via a pair of methane records from the two poles (e.g. Blunier et al., 1998; Capron et al., 2010). These chronologies were then extended via a Monte Carlo approach (e.g., adapted from Blunier et al., 2007). This gives us 7 cores and 12 pairs of records to work with.

In order to determine the instantaneous phase of these now comparable time series, analytical functions are constructed for each time series (see Appendix A) (Gabor, 1946). The ice core temperature proxy signals are complicated signals, whereas the Hilbert Transform is only proven accurate on mono-components (Cohen, 1995; Huang et al., 1998). Therefore, the mono-components of the signal polar signals were extracted using the Empirical Mode Decomposition (EMD) (Huang et al., 1998) which provides Intrinsic Mode Functions (IMF). The HT is then applied to each mono-component signal (each IMF), a procedure equivalent to a Hilbert Huang Transform (HHT) (Huang et al., 1998). To obtain the phase shift transformed signal, we employed HHT (equivalent to a $-\pi/2$ shift) and inverse HHT ($+\pi/2$ shift) with integral limits from past to future (see Appendix A).

As seen in Fig. 1.6, the 1 ky–6 ky period signals are synchronized with $\pi/2$ phase shift. Therefore, the Antarctic climate leads that of Greenland by 250yr–1500yr. Hinnov et al. (2002) showed a time lead of BYRD DO oscillations over GISP2 by 384 ± 70yr, which is within that

range. Our observations indicate that the phase shift is frequency independent, as all Fourier components are shifted by $\pi/2$, at least in the period band 1 ky–6 ky.

Figure 1.6 shows the full results of the comparison between NGRIP in the north and the HT of Dome C in the south. As shown in Fig. 1.7, the calculated phase lock is nearly constant and equal to $\pi/2$ modulo 2π. Sudden phase jumps of 2π, which occur during abupt de-synchronization episodes (Fig. 1.7), are likely excited by noise, timing errors or external forcing and do not persist for long periods.

3. Simulation of Antarctic climates from Greenland climates

3.1. Frequency band separation

In order to begin to build our model, we separate the polar signals into two bands, above and below 50 kyrs. The 800 kyr-long EPICA proxy records (and most temperature proxy records for the last million years) also have a well established tendency of consisting of easily identifiable and disjointed groups of statistically significant power peaks in the long period band (>70 kyr) and the short period band (<45 kyr), with little or no interaction between the two. The latter is assumed to reflect the high frequency response of sea ice, while the former reflects the long period response of the major ice sheets to eccentricity-induced changes in insolation.

To ensure that the separation of these nonlinear signal components is valid, Empirical Mode Decomposition (EMD) and Singular Spectrum Analysis (SSA) were used (Fig. 4). Note that the EMD and SSA techniques have been broadly adopted for the analysis of paleoclimatic

time series (e.g., Gloersen and Huang, 2003; Lin and Wang, 2006; Sole et al., 2007; Huang and Wu, 2008) and are described in detail in Appendix D.
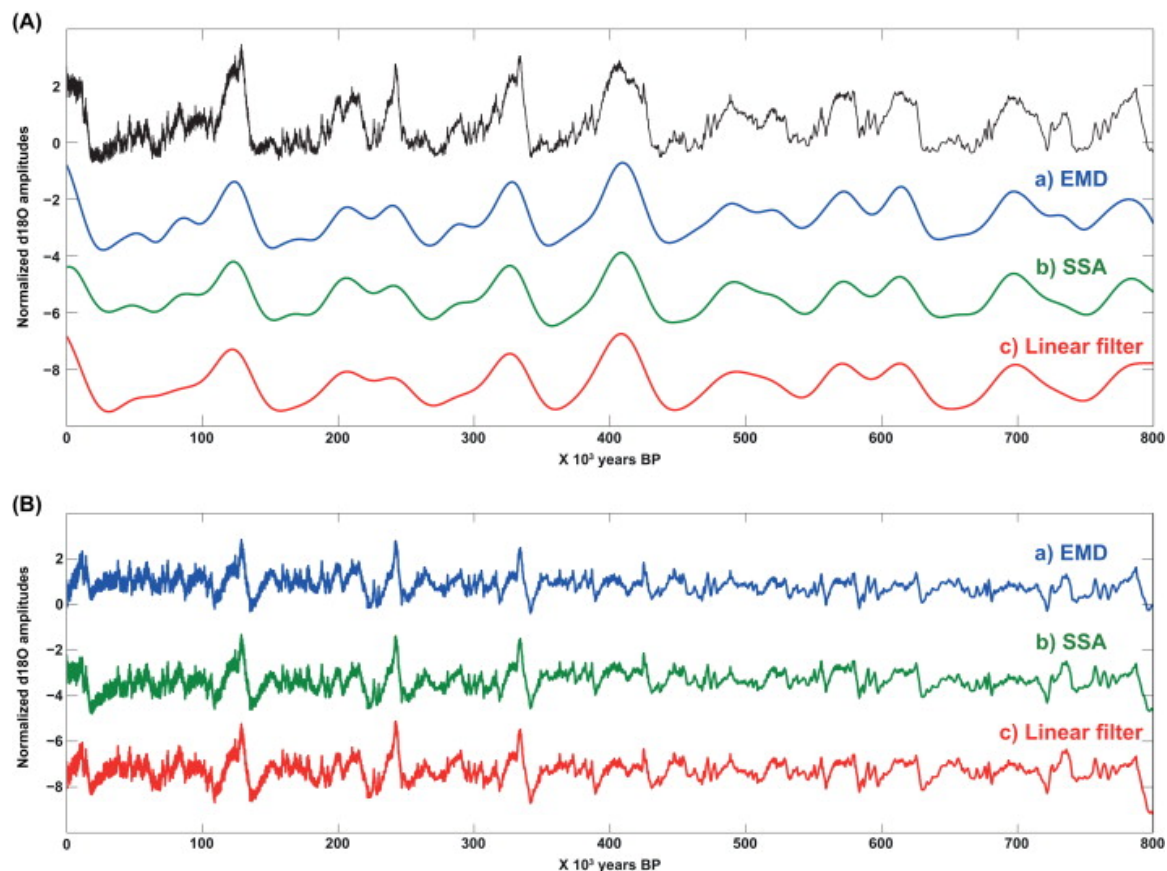
Fig. 1.8.

(A) Long period signals obtained by various filtering methods. Black line on the top shows Epica Dome C temperature proxy. a) Long period signal obtained by decomposing the data into 13 IMFs. The long period signal shown is calculated by summing 8th–12th IMFs. The IMFs are selected so that they produce ~100 ky frequency band signal. b) Long period signal obtained using SSA. For the long period from SSA, we adopted first 3 components with 1600 point windows. c) Low pass filtered signal using a conventional linear filter. All three techniques extracted essentially the same wave shape of long period signal from the data. See Appendix for details of the filtering methods. (B) High frequency signals after removal of long period components in (A).

Dome C, shown in Fig. 1.8, shows very little distortion in either the long or the short band, suggesting a true separation of the processes that produced the long and short period signals in both a linear and nonlinear combination.

3.2. Modeling the climate of the South from that of the North

In climate science, there are few well-established, simplified models that include both aperiodic forcing and stochastic effects (as are needed for polar modeling), but many areas of science indicate that relaxation oscillators are excellent candidates for the simulation of natural nonlinear oscillators. The Van der Pol oscillator is one of the most common, and has already been applied in climate sciences. Saltzman and Moritz (1980), Saltzman et al. (1981), Saltzman and Sutera (1984) and later Saltzman (2002) formally introduced a set of nonlinear, ordinary differential equations for sea ice extent and average ocean temperature in a glacial atmosphere equivalent to a Van der Pol/Duffing oscillator, which have since been widely adapted (Yang and Neelin, 1993; Zhang et al., 1995; Egger, 1999; Rial and Yang, 2007; Stommel, 1961; Källén et al., 1979; Paillard, 1998; Schulz et al., 2004; Colin de Verdière et al., 2006; Marchal et al., 2007; Crucifix , 2011; Rial and Saha, 2011; Crucifix, 2012; De Saedeleer et al., 2013).

Therefore, to simulate the high frequency response, we used the basic Van der Pol Synchronization Oscillator (VSO) model (see Appendix B). The VSO model consists of two pairs of first order, ordinary differential equations that represent two coupled Van der Pol oscillators, with each pair describing sea ice extent and mean ocean temperature at each Polar Region. The model is externally forced by summer insolation at 65 degrees North.

Rial (2012) used a VSO to simulate temperature proxies in short segments of the Greenland and Antarctica records and assess the presence of synchrony between the Polar Regions. We extended that study, employing a VSO to simulate the Antarctic temperature proxy record from that of Greenland (Fig. 1.9). Fig. 1.9A shows the theoretical Greenland temperature (calculated with a single Van der Pol model oscillator) over the last 400 ky compared to the EPICA record. Fig. 1.9B shows the modeled southern temperature oscillations with external forcing and noise but without coupling ($q_1 = q_2 = 0$; see Appendix B for the meaning of the parameters). As coupling is incorporated, the VSO model produces a far better simulation of the data (Fig. 1.9C). Comparison of Fig. 1.9B and C suggests that the effects of noise and insolation forcing are nearly suppressed when the coupling is applied, though the specific role of all parameters in the model will be discussed in detail in the next section.
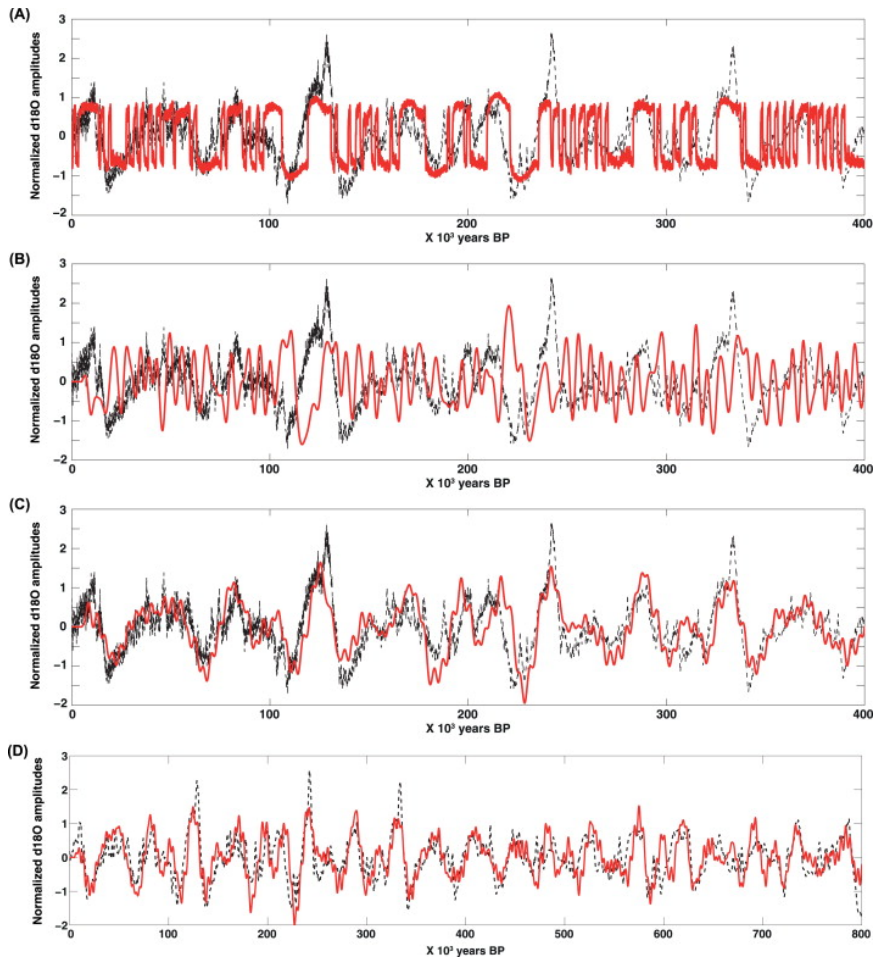
Fig. 1.9.

(A) The simulated record of Greenland temperature variation (red) and the high frequency (HF) component of the EPICA record. (B) The simulated Antarctic record without synchronization. (C) The Greenland record transformed by the VSO model into a synchronized Antarctica record compared to the actual time series (black). (D) The simulations (red) for the HF EPICA for the last 800 ky compared to the actual records (black). Parameter values for the results (D): $q_1 = 1000$, $q_2 = 0$, $a_1 = 0$, $a_2 = 0.06$, TN = 1500, TS = 2400, noise level = 0.55.

Fig. 1.9D shows the simulation results using the polar synchronization VSO model. From 100 ka to 800 ka, this model is based upon the theoretical northern temperature variations depicted in Fig. 1.9A.

In order to simulate the separated long period response, we use the ice volume model devised by Saltzman (2002), mentioned earlier and described in detail in Appendix C. This model produces free oscillations with periods near 100 ky of ice mass, carbon dioxide, and deep ocean temperature with appropriate parameter values in the absence of external (astronomical) forcing. Saltzman (2002) indicated the region for the parameters in which the model produces stable oscillations and provided the simulation of ~100 ky period glacial cycles with those parameter values (Saltzman, 2002). As shown in Fig. 1.10 the ice sheet model closely reproduces the frequency and amplitude of glacial cycles with the simulated 413 ky forcing of the past 800 ky.
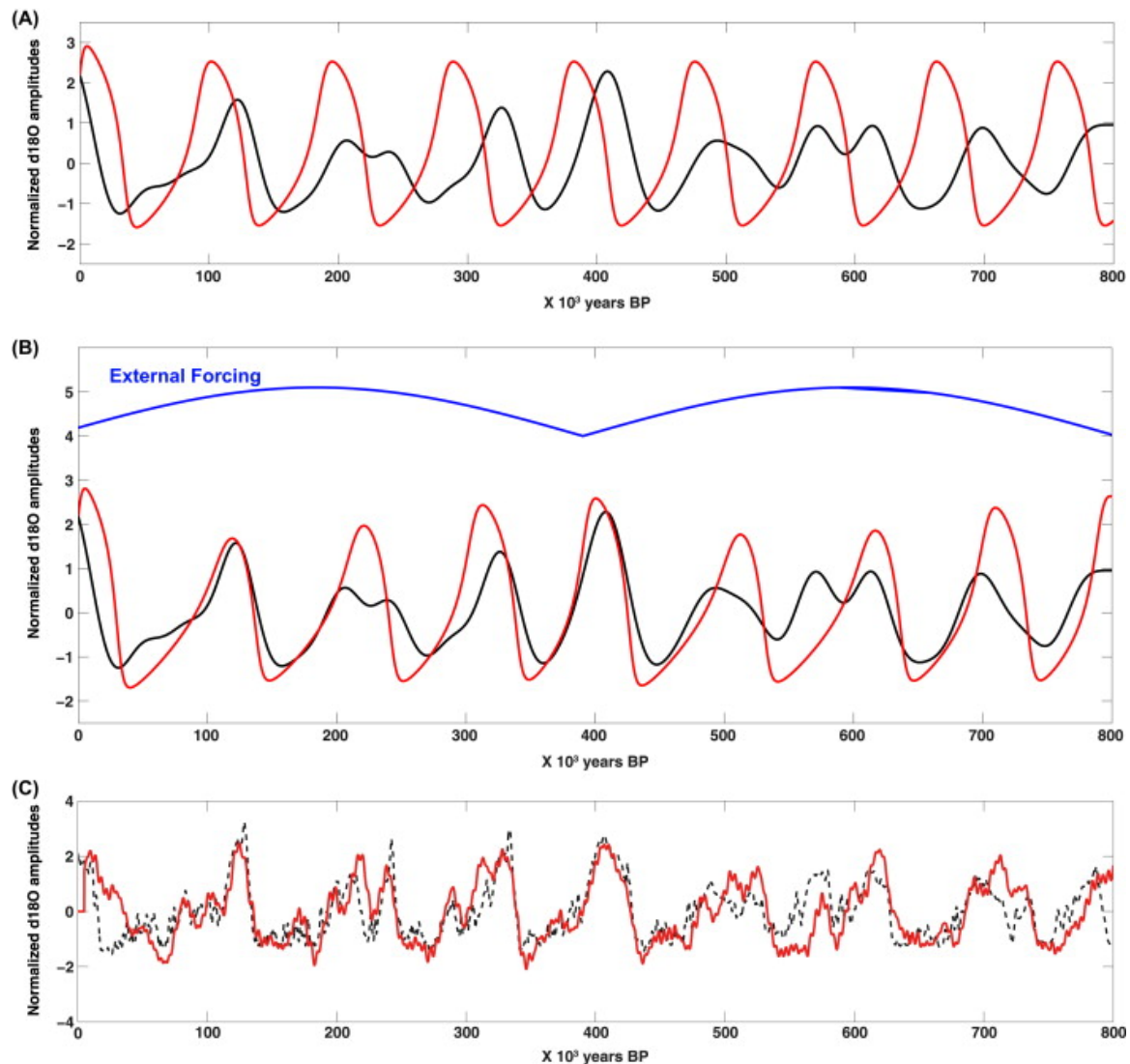
Fig. 1.10.

(A) Long period (~100 ky) simulation using the ice sheet model without external forcing. Epica Dome C temperature proxy data (black) and simulated ~100 ky components (red) are shown. (B) The model is externally forced by rectified cosine curve (blue line) that simulates the 413 ky eccentricity forcing. (C) The simulations (red) for the HF and low frequency components together for the last 800 ky compared to the actual records (black). Parameter values for the results (C) are same with those for Fig. 1.9D.

Now that we have developed simulations describing both the long and short period frequency bands of the records, they can be combined to create a complete model for the last

31

800 ky. Fig. 1.10C shows the long period component from the ice sheet model added to the simulated high frequency signal.

3.3. Model stability under parameter uncertainty

There are three sources of uncertainty generally considered in a modeling procedure: the stochastic nature of a given model, parameters, and observed input data. Since the stochastic nature of the VSO model is in the stochastic term of the model and the model does not require observed data, the uncertainty of the VSO modeling results arises from the uncertainty in the values of the three adjustable parameter pairs (see Appendix B) a_i, ω_i and q_i (a_1, ω_1, q_1 in the North; a_2, ω_2, q_2 in the South). These describe the strength of external forcing, the assumed natural oscillating frequency, and the coupling strength, respectively. Here, we investigate the effect of parameter uncertainty on the model stability and provide the range of the parameters within which the uncertainty of the parameters is restricted to be under that from the stochastic term. First, we find the parameter set that provides the best fit according to the correlation coefficient (R) and root mean square error (RMSE); then we assume that the parameter set is true. To explore the uncertainty from the stochastic term, we ran the model 10,000 times, then calculated the corresponding R and RMSE with the fixed true parameters so that the model responded only to internal stochastic forcing. From the 10,000 values, we determined 5% and 95% of R (0.43, 0.57) and RMSE (0.85 1.29) as lower and upper limits respectively. Then, as a parameter changes, if both R and RMSE remain within the interval 95% and 5% respectively, we consider the model stable to changes in that parameter (Fig. 1.10A). With this information, we obtained the regions of each parameter space within which the VSO model simulates a temperature proxy in Antarctica compatible with the observations, which is shown in Table 1

32

and where the parameter uncertainty is restricted to smaller than the uncertainty from the stochastic term.
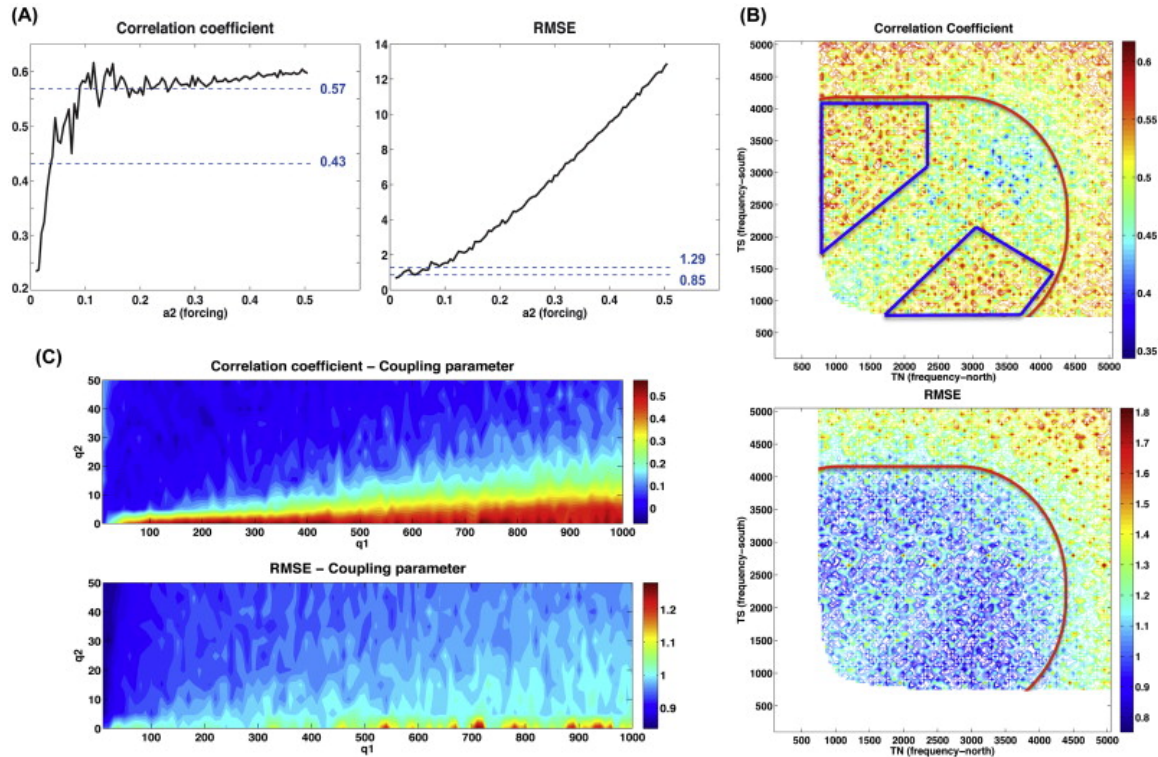
Fig. 1.11.

Stability of the VSO model simulation as changing parameter values. (A) Correlation coefficient and RMSE as the forcing level a_2 increases from 0 to 0.5. Strong external forcing makes the model to be controlled only by the forcing, so the model produces large errors for $a_2 > 0.1$. (B) Correlation coefficient and RMSE as periods TN and TS range from 0 to 5000 years. When either TN or TS are less than 750 (white region), the model results diverge. The oscillation parameters bounded by the blue rectangular produce the smallest uncertainty (i.e. the stable regions for both TN and TS range from 750y to 4200y). (C) Correlation coefficient and RMSE as q_1 increases from 0 to 1000 and q_2 from 0 to 50. The VSO model produces stable simulations when $q_1 > 60$.

Table 1:

VSO model parameter values which produces stable simulation of Antarctica temperature proxy for the last 800 ky.

Parameter	Range	Function
q_1	60~6000	Rate of mean ocean temperature change between Arctic and Antarctic
q_2	0	Mean ocean temperature change between Arctic and Antarctic
a_1	0	External forcing to north
a_2	0.05~0.12	External forcing to south
TN	750~4000	Oscillation (north)
TS	750~4000	Oscillation (south)

a_1 and a_2 adjust strength of external insolation forcing (a_1: north, a_2: south). These parameters modulate how strongly the insolation affects the natural oscillation of the climate. (a) The parameters are large enough: simulated results from the VSO model are completely dependent on the insolation. (b) These parameters are too small: the simulated results are independent of the insolation. Temperature fluctuation at millennial scale should be between (a) and (b). Though it is impossible to calculate the exact amount of insolation affecting the millennial scale climate oscillation, we suggest the range of parameter values that could produce compatible simulation with the observation. q_1 and q_2 adjust strength of coupling effects (q_1: dissipative, q_2: reactive). These parameters modulate how strongly the north–south coupling affects to the simulated results. If both these parameters are zeros, north and south are simulated independently without synchronization. q_1 adjusts the strength of the coupling effect caused by differences in mean ocean heat flux which is calculated by differences between gradient of mean ocean temperature in north and south. q_2 adjusts the strength of coupling effect caused by differences in mean ocean temperature. The model simulation suggests that the synchronization occurs through differences in mean ocean heat flux rather than simple differences between two poles.

Fig. 7 shows the model uncertainty from the parameters. The model behavior according to the parameter uncertainty and the ranges of the parameters that produce smaller effects than stochastic forcing can be summarized as follows:

i) Insolation parameters (a_1, a_2), Fig. 1.11A: Parameter a_i regulates the strength of external forcing. The synchronization model originally included two forcing terms (a_1, a_2) at each pole (Eqs. (B.1) and (B.3)), but we use only one external forcing term (a_2) in the south for this simulation. Strong external forcing overwhelms the model's responses to the other parameters (q and ω), thus a_2 has to be constrained under a certain value because when external forcing is too strong, the simulated time series just follows the shape of forcing. From Fig. 1.11A, calculated as a_2 increases, the model produces stable simulation when $0.05 < a_2 < 0.10$.

ii) Oscillation parameters (ω_1, ω_2), Fig. 1.11B: The angular frequencies ω_1 and ω_2 are given by $\omega_1 = 2\pi/TN$ and $\omega_2 = 2\pi/TS$ where TN and TS are the assumed periods of the natural oscillations of the North and South climates respectively.

The model produces close simulations when the periods are within both the millennial scale and the range of the assumed period of the thermohaline circulation (Marotzke et al., 1988; Bond et al., 2001). Fig. 1.11B shows the range of the natural frequency parameters which produces smaller uncertainty and a close simulation of Antarctic Records (e.g. TN: 1500yr and TS: 3000yr or vice versa).

iii) Coupling parameters (q_1, q_2), Fig. 7C: RMSE ranges from 0.86 to 1.26 but these values fall within the range of RMSE values generated by the stochastic response. Thus, RMSE

cannot be used as a criterion for selecting best parameter values in this case. The results show that the correlation coefficients dramatically decrease as q_2 increases and the model produces stable outputs when $q_1 > 60$ and $q_2 < 10$. Consequently, the reactive coupling term (q_2) can be dropped in modeling while the dissipative term (q_1) is required to be strong for both smaller uncertainty and a close simulation of the Antarctic temperature proxy.

4. Discussion

The results of both model and data study support a continuous phase synchronization of the polar climates for the length of the records. The physical processes behind this are not fully understood, but, as the next chapter demonstrates, evidence points to the thermohaline circulation as the most likely driver of the climate connection between the poles. The models we used to characterize the connection are robust with respect to changes in the adjustable parameters, and suggest that the connection between northern and southern climates is strongest when it involves the dissipative properties of the ocean/atmosphere, namely the difference between northern and southern heat flux.

The simplified VSO model does not have enough detail to provide a more specific view of the systems that couple the two Polar Regions. On the other hand these first two sections indicate that the idea of climatic synchronization is likely to be general. Indeed, modern patterns of atmospheric/oceanic circulation of large spatial scale and a high degree of temporal persistence show examples of synchronization (see Chapter 3). However, given the evidence of the drifting synchronization seen in the overall global climate with respect to the eccentricity forcing and the physical differences in the two poles as oscillators, we could hypothesize that the

polar climates were once unrelated to each other and likely chaotic, and that, through weak oceanic/atmospheric coupling, the two polar systems eventually synchronized by slowly modifying their own frequencies and phases to respond to each other's influence, until synchronization ensued and stabilized.

5. Conclusions

This study presents statistical investigations to explore and quantify the long-term relationship between Greenland and Antarctica's climate variability with polar synchronization as a mechanism to connect them, as well as presenting simplified, easily computable, and stable models for the last 800 ky of the polar paleoclimates. Using methane-matched records from GRIP and Byrd ice cores, we were able to match the age models of NGRIP and Dome C ice core records through a Monte-Carlo approach. Further, analysis of the model uncertainty with such minimal relative age uncertainty supports that simulated results are robust under small change of parameters. Use of this model and the simplified view of a highly complex system would be helped by further explanation of the underlying physical processes of the polar climates. However, synchronization as a paradigm for the linking of polar climate processes is well supported by our results and takes us a step further in our understanding of large-scale climate dynamics.

Part III: Conclusions

The progression of these two synchronization studies provide simplified dynamical rules for internal oscillations of the global climate system, but in the latter case, the question of mechanism of connection and energy transfer is left unanswered. However, the linear phase

relationship between the polar climates (i.e. the linear pi/2 phase shift present throughout the record) may allow for linear analysis tools to be used on these nonlinear systems, when studying their interactions. This would allow the simple models shown here to gain more physical meaning in the context of the paleoclimate.

Supplemental Figures:

Section 1

$$F_m(t) = A(t)[1 - a h_m(t)]\cos[\omega_c t + \varphi - \varepsilon h_m(t)]$$

$$h_m(t) = \|\cos(\omega_m t - \psi)\|$$
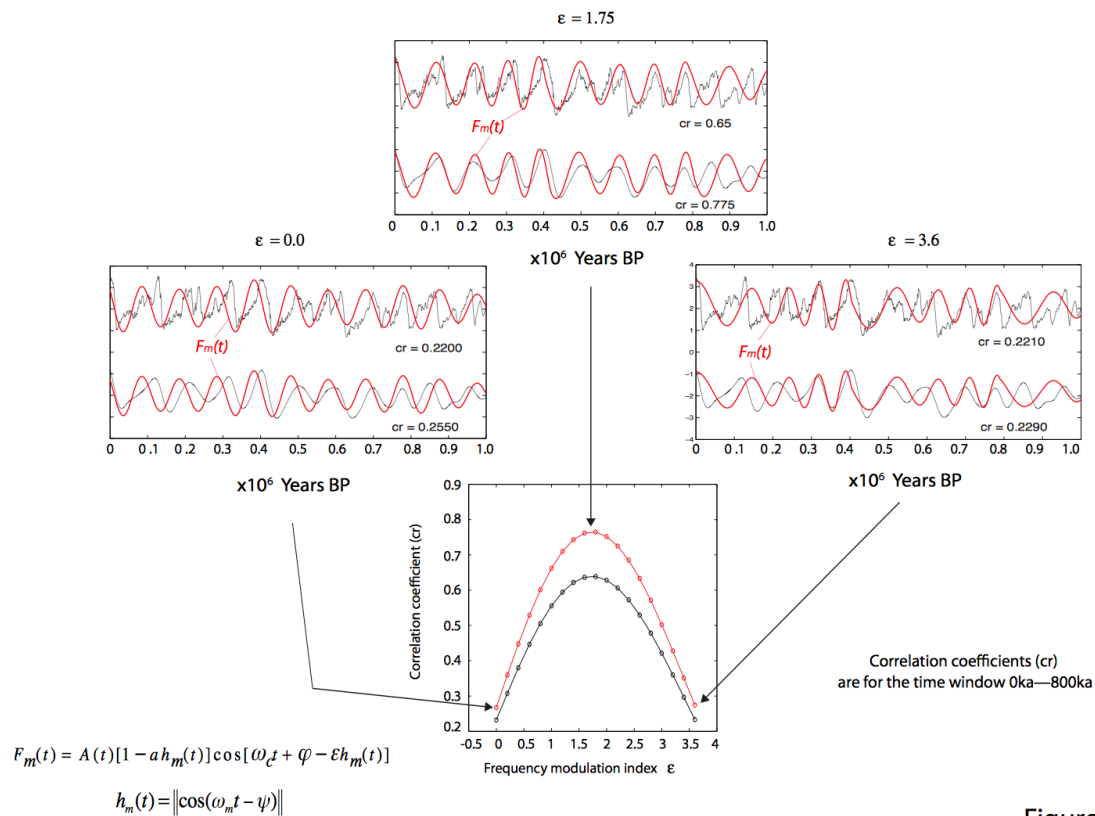
Figure S1

Figure S1: Correlation coefficients between the frequency modulated signal $F_m(t)$ and the LR04 stack over the last 1my as FMI increases. The highest correlation coefficient (0.775) corresponds to FM1=1.75.
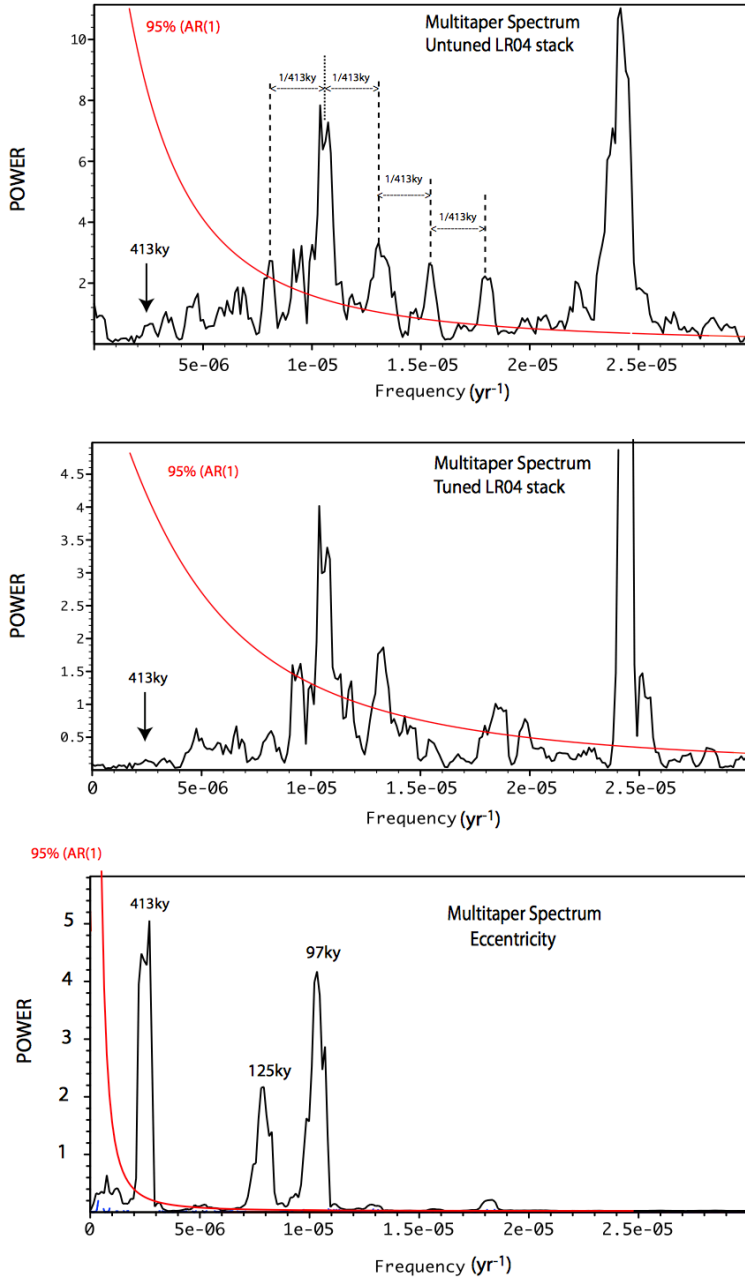
Figure S2: Evidence for frequency (phase) modulation in the spectrum of the untuned benthic stack LR04 are the sidelobes around the main 97ky carrier spaced 1/413ky from each other. The spectrum of the LR04 stack shows negligible power at 1/413ky (compared to 1/100ky power). In contrast, the spectrum of orbital eccentricity contains a strong peak at 1/413ky.

40
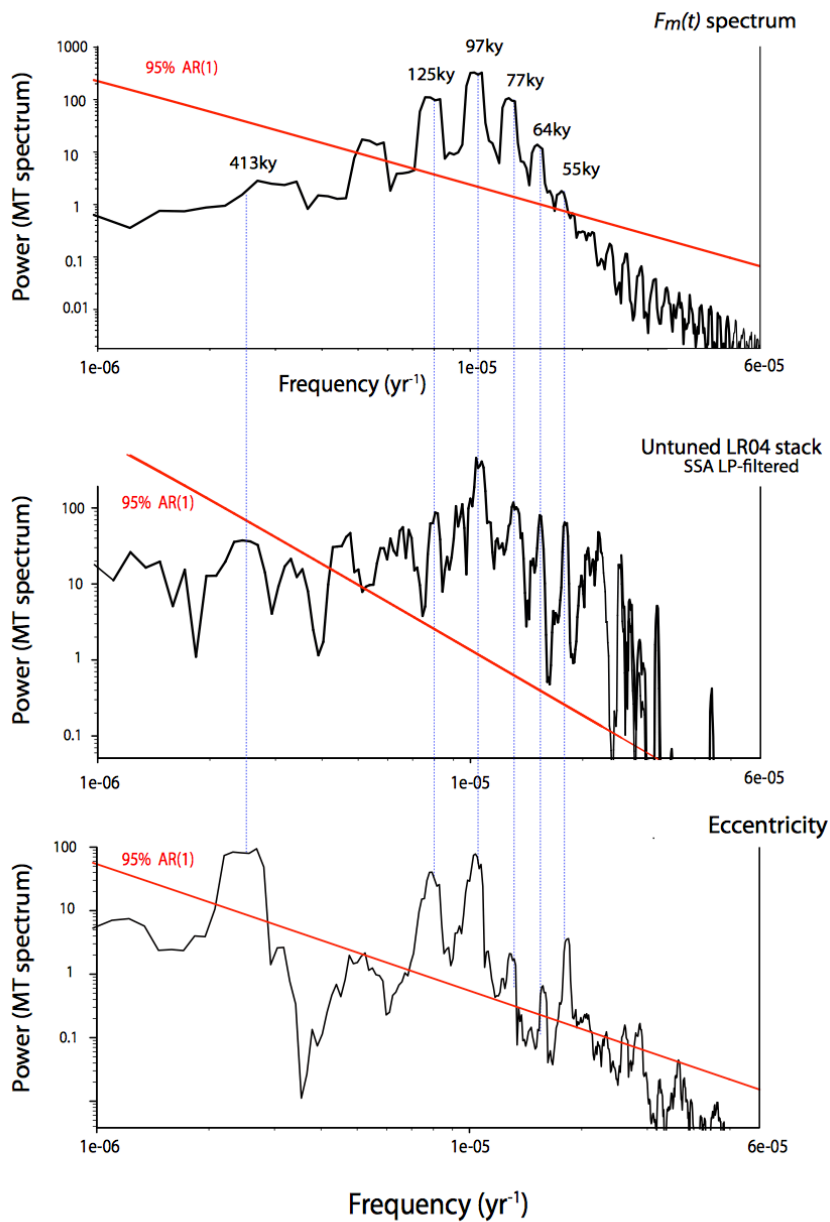
Figure S3: Spectra of the simulated *Fm(t)* function (see Methods), the LR04 stack and theoretical eccentricity forcing. Amplitude modulation produces sidelobes at the same frequencies as frequency modulation21, 22, but as shown in the eccentricity spectra here and in Figure S2 they are nearly two orders of magnitude smaller than the main eccentricity peaks. The spectrum of the data in contrast shows strong sidelobes of the same magnitude of the eccentricity peaks, consistent with a moderate frequency modulation index of ε=1.75
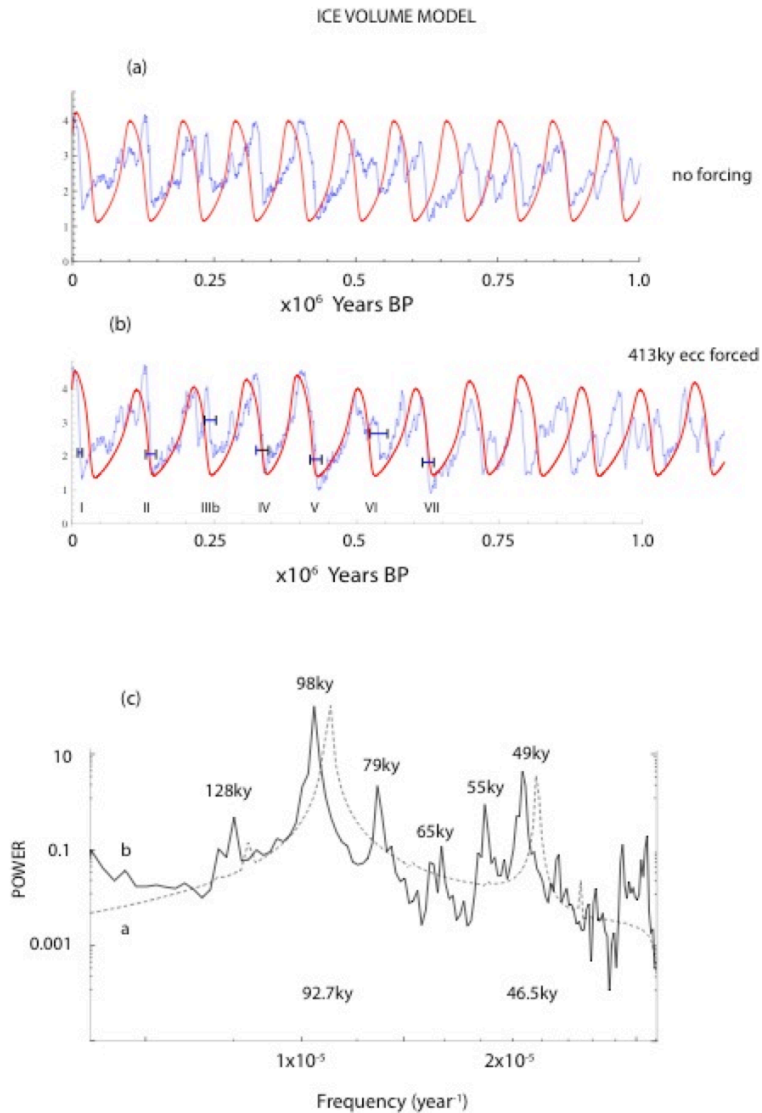
Figure S4

A free oscillation of ~93ky is obtained using p=1.69; q=0.58; r=0.55; v=0.68, s=0.78 and A=0 (unforced) plus harmonics (the first higher harmonic at 46.5ky is shown) that account for the saw-tooth waveform. With the same parameters as above, and just increasing the forcing to A=1 the model closely reproduces the LR04 record and within timing uncertainty (horizontal bars) fits the timing of the glacial terminations. The figure shows that the 1/413ky simulated eccentricity forcing is transformed into frequency modulation of the ~1/100ky natural frequency, resulting in time series and spectral characteristics similar to those observed.
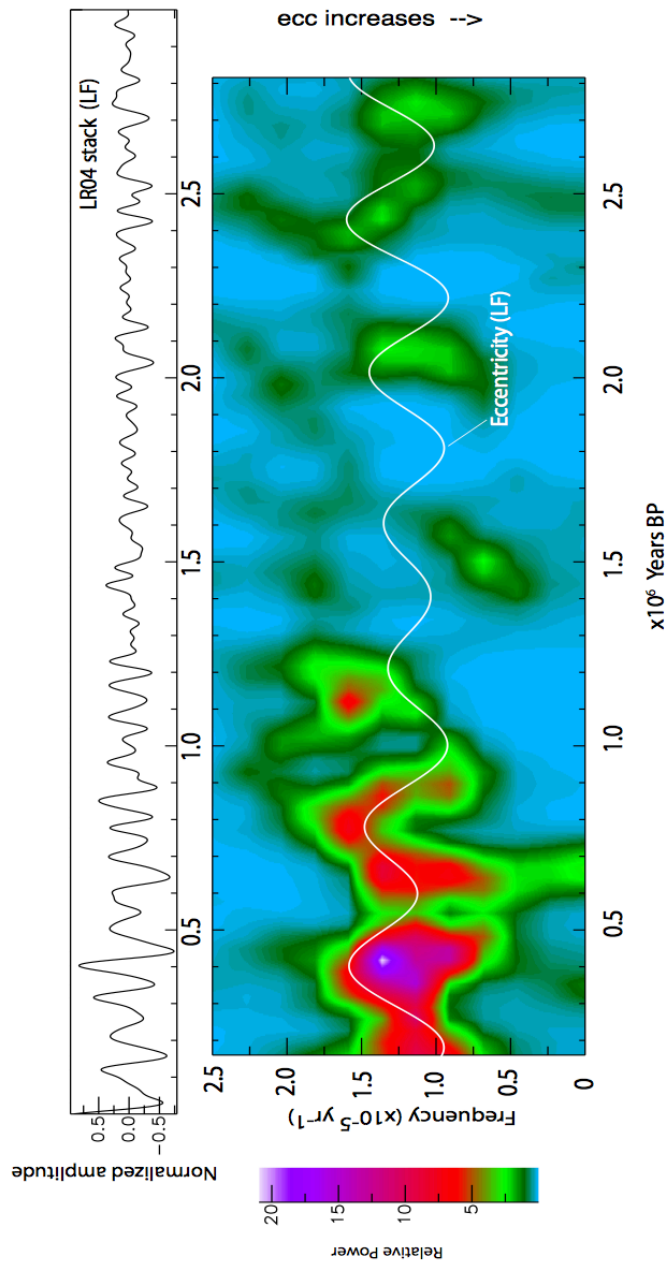
Figure S5

The spectrogram of the band-pass filtered LR04 stack is compared with the low frequency component of eccentricity (see text for details).

Figures S6-S8

These figures (S6-S8) show details of the analysis summarized in Fig. 1.7.
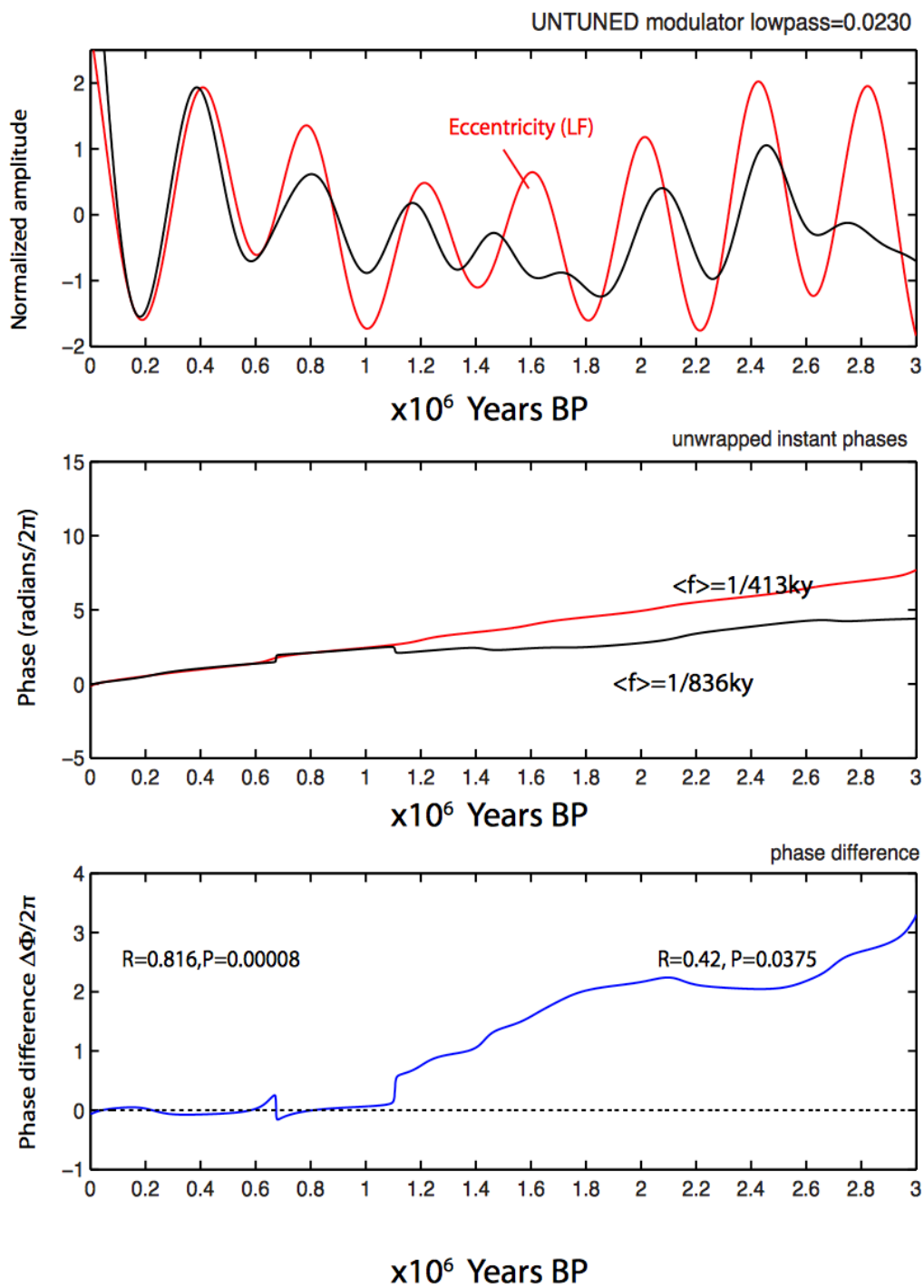
Figure S6
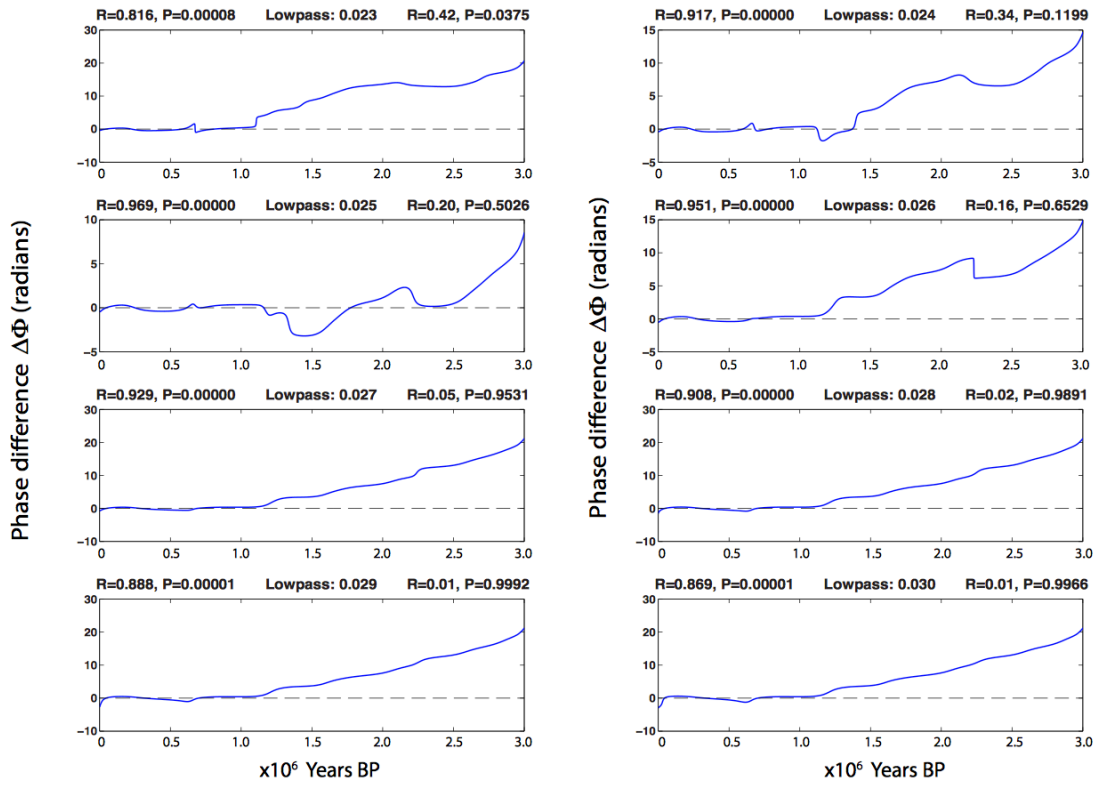
Figure S7

Figure S8

46
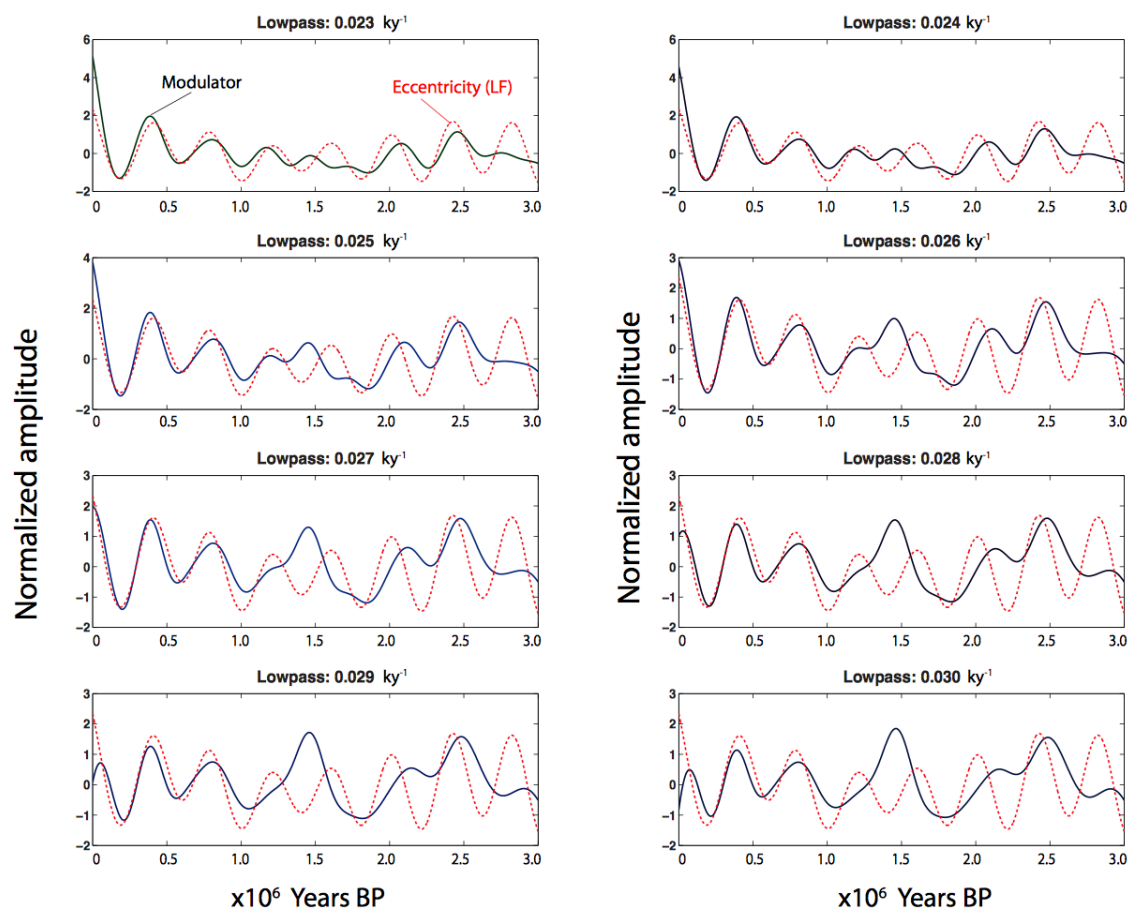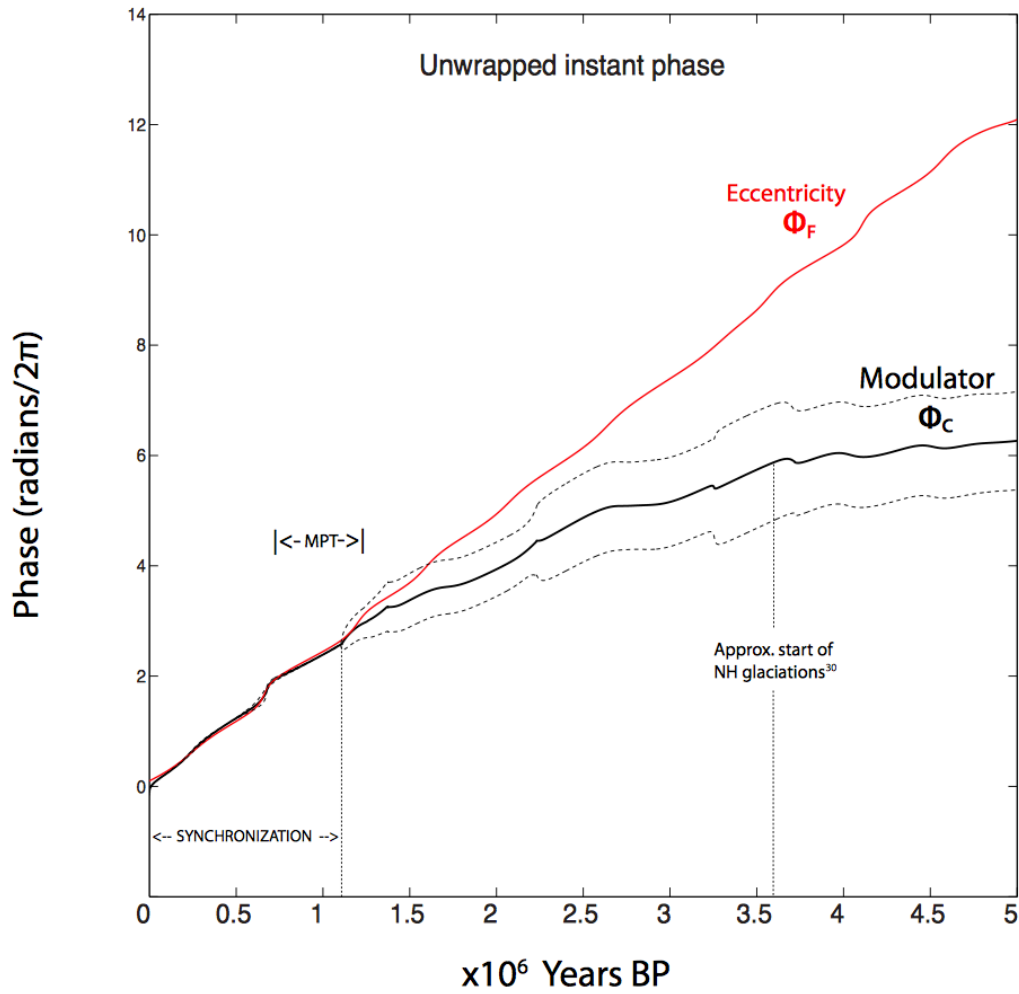
Figure S9

Evolution of the phases of modulator and eccentricity forcing from 0My to 5My. The Mid Pleistocene Transition (MPT) occurs when the phase of the long-period climate response is finally 'captured' by the 413ky eccentricity forcing, around 1.2Ma.
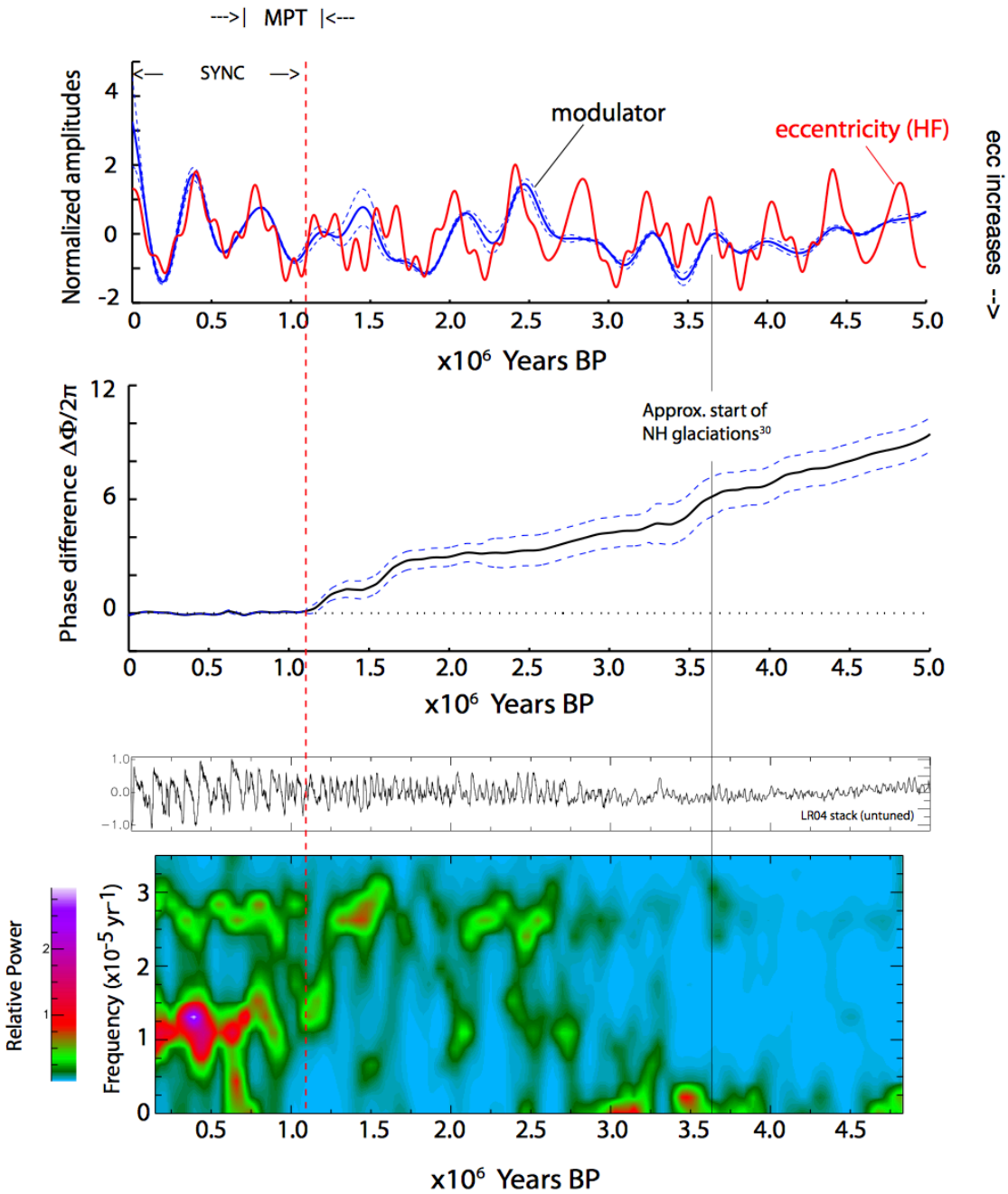
Figure S10

Modulator, HF forcing, phase difference function $\Delta\Phi(t)$ and spectrogram of the LR04 stack showing the

time evolution of the power in the 1/41ky, 1/100ky and 1/400ky frequency

bands from 0My to 5My.

48

SCHEMATIC EXAMPLE OF SPECTRAL SYNCHRONIZATION (computed with ice volume model)
(1/413ky FORCING OF FREE OSCILLATIONS fo 1/450ky and 1/500ky)
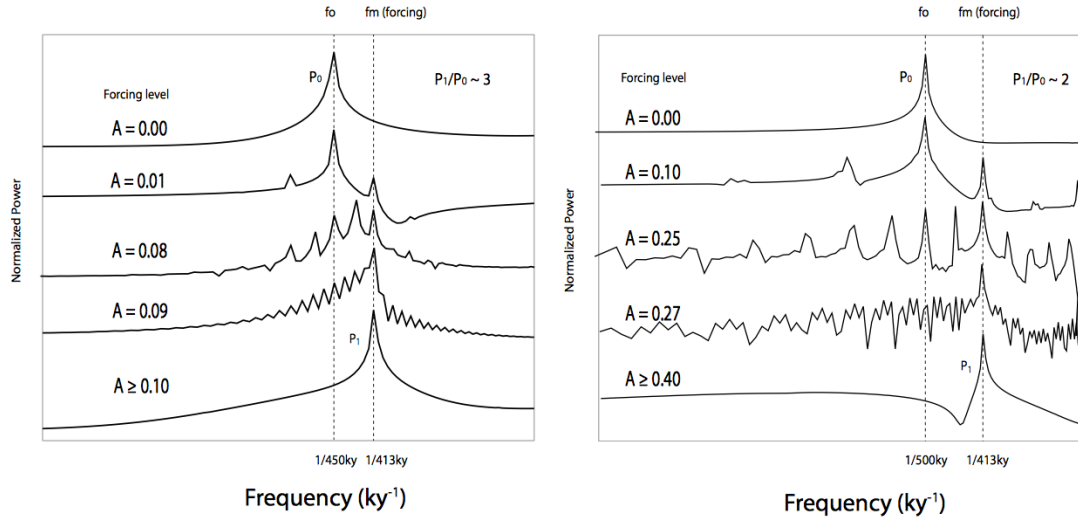
Figure S11

Using model S-1 to illustrate the theoretical effect of synchronization by the 413ky of natural oscillations at periods of 450ky and 500ky for increasing forcing.
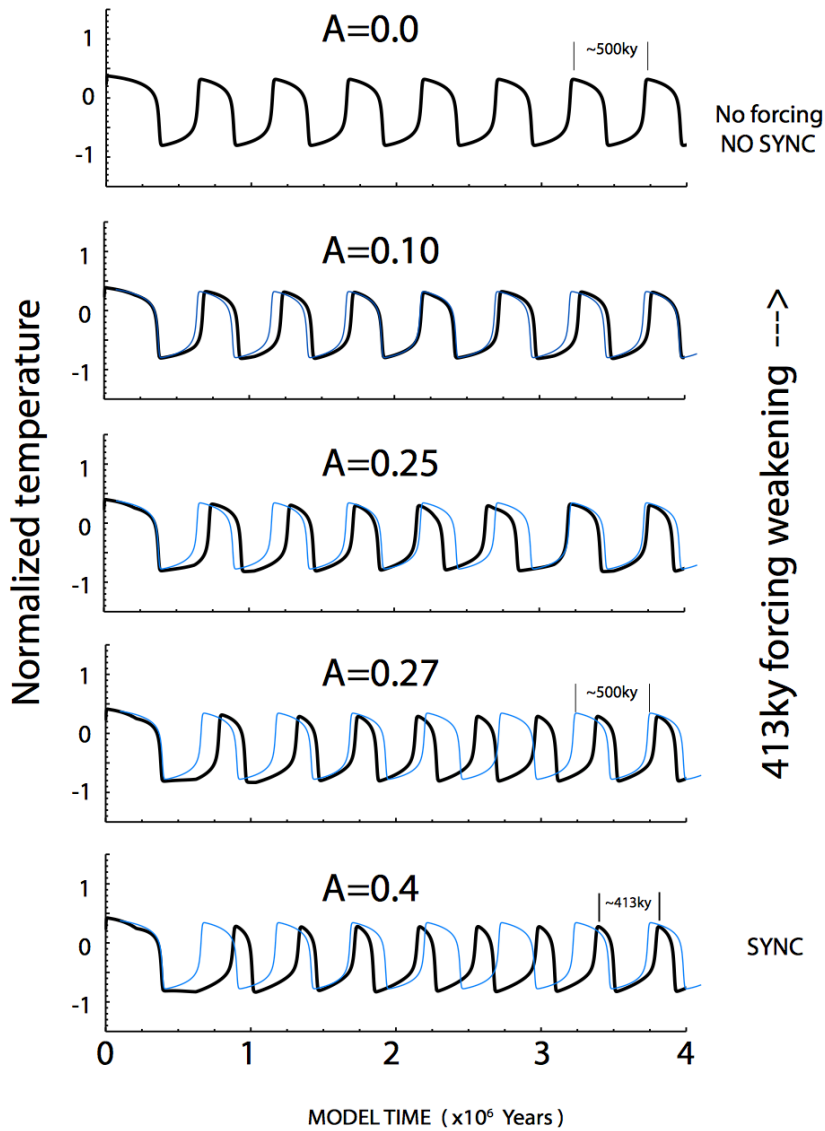
Figure S12

The time series of the previous figure for the 500ky case illustrate the probable cause of the observed ODP Site 659 switch from ~400ky cycles before 1.8Ma to ~500ky cycles since then.

Phase differences and modulators for tuned and untuned LR04
(effect of age uncertainty)
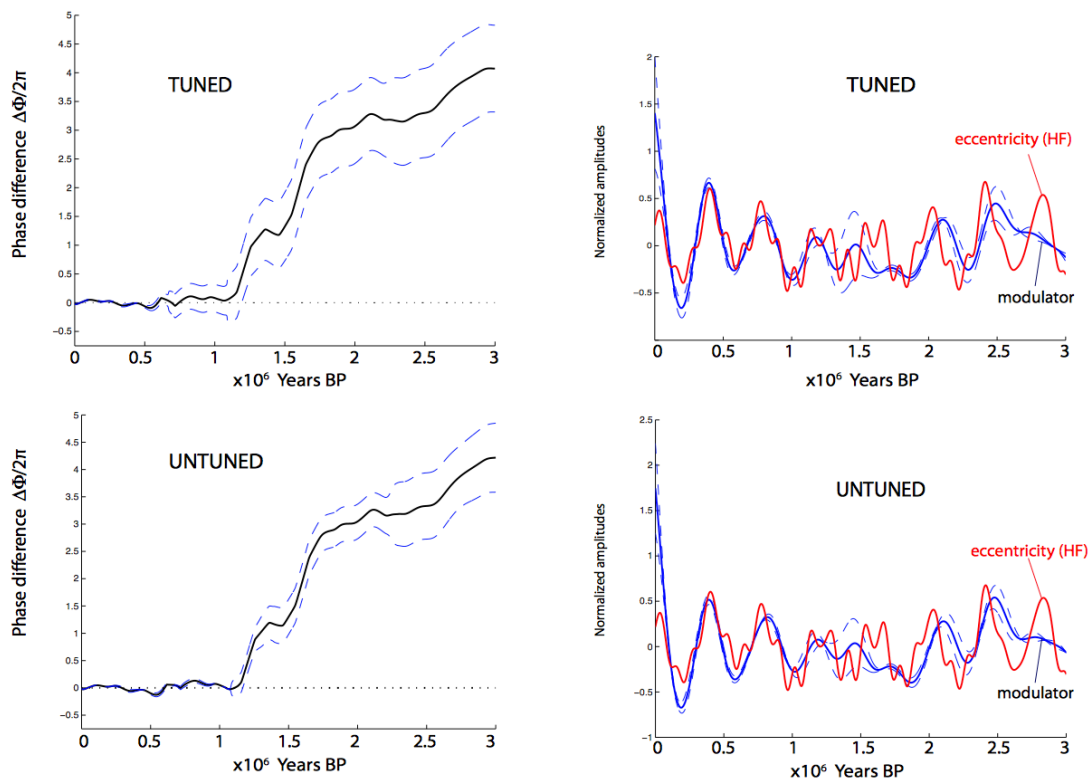
Figure S13

Comparison between phase difference functions and modulators for the tuned and untuned LR04 proxy records. The differences are small and consist, in the tuned record, of greater standard deviation from the mean for times earlier than 0.7Ma and slight de-phasing of the modulator.
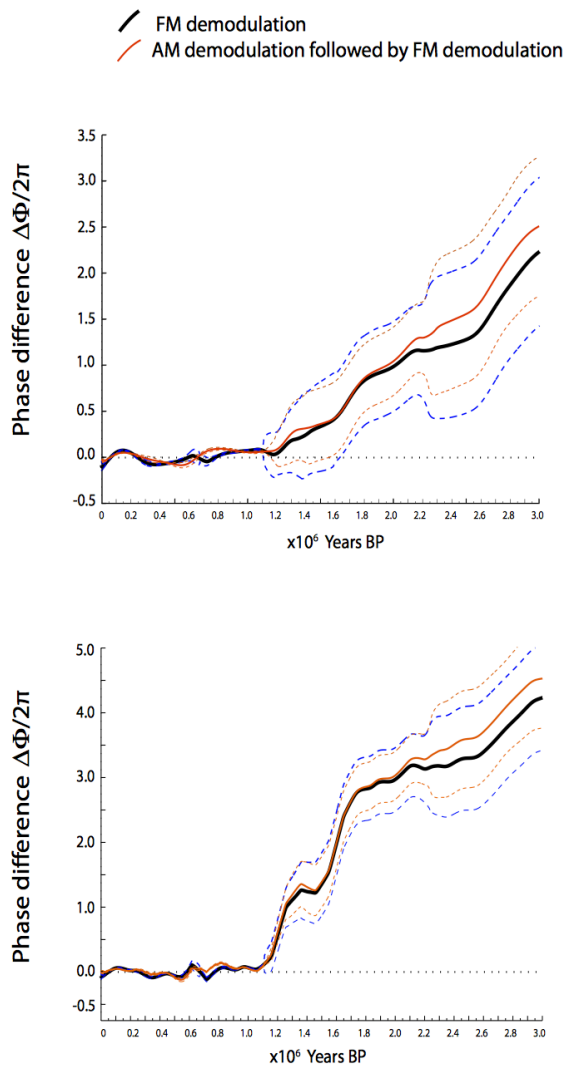
Figure S14

Comparison between phase difference curves shows that show not removing the amplitude modulation would produce a second order effect and would not affect our conclusions.

REFERENCES

Balanov, A., Janson, N., Postnov, D., Sosnovtseva, O., 2009. Synchronization, From Simple to Complex. Springer-Verlag, Berlin, Heidelberg, p. 425.

Barker, S., Diz, P., Vautravers, M.J., Pike, J., Knorr, G., Hall, I.R., Broecker, W.S., 2009. Interhemispheric Atlantic seesaw response during the last deglaciation. Nature 457, 1097e1102.

Barker, S., Knorr, G., Edwards, L., Parrenin, F., Putnom, A.E., Skinner, L.C., Wolff, E., Ziegler, M., 2011. 800,000 Years of abrupt climate variability. Science 334, 347e 351.

Bennett, M., Schatz, M.F., Rockwood, H., Wiesenfeld, K., 2002. Huygens' clocks. Proc. R. Soc. London A 458, 563e579.

Berger, A., Melice, J. L. & Loutre, M. F. On the origin of the 100-kyr cycles in the astronomical forcing. Paleoceanography 20, PA4019 (2005).

Blunier, T., Chappellaz, J., Schwander, J., Dallenbach, A., Stauffer, B., Stocker, T.F., Raynaud, D., Jouzel, J., Clausen, H.B., Hammer, C.U., Johnsen, S.J., 1998. Asyn- chrony of Antarctic and Greenland climate change during the last glacial period. Nature 394, 739e743.

Blunier, T., Brook, E.J., 2001. Timing of millennial-scale climate change in Antarctica and Greenland during the last glacial period. Science 291, 109e112.

Blunier, T., Spahni, R., Barnola, J.M., Loulergue, L., Schwander, J., 2007. Synchronization of ice core records via atmospheric gases. Clim. Past 3, 325e 330.

Bond, G., Kromer, B., Beer, J., Muscheler, R., Evans, M.N., Showers, W., Hoffmann, S., Lotti-Bond, R., Hajdas, I., Bonani, G., 2001. Persistent solar influence on North Atlantic climate during the Holocene. Science 294, 2130e2136.

Bracewell, R., 1986. The Fourier Transform and its Applications, second ed. McGraw- Hill, New York, p. 474.

Broecker, W.S., 1998. Paleocean circulation during the last deglaciation: a bipolar seesaw? Paleoceanography 13 (2), 119e121.

Broomhead, D.S., King, G., 1986. Extracting qualitative dynamics from experimental data. Phys. D 20, 217e236.

Capron, E., Landais, A., Chappellaz, J., Schilt, A., Buiron, D., Dahl-Jensen, D., Johnsen, S.J., Jouzel, J., Lemieux-Dudon, B., Loulergue, L., Leuenberger, M., Masson-Delmotte, V., Meyer, H., Oerter, H., Stenni, B., 2010. Millennial and sub- millennial scale climatic variations recorded in polar ice cores over the last glacial period. Clim. Past 6, 345e365.

Clark, P. U. et al. The Middle Pleistocene transition: Characteristics, mechanisms, and implications for long-term changes in atmospheric pCO2 . Quat. Sci. Rev. 25, 3150–3184 (2006).

Cohen, L., 1995. Time-frequency Analysis. Prentice-Hall, Englewood Cliffs, NJ.

Colin de Verdière, A., Ben Jelloul, M., Sévellec, F., 2006. Bifurcation structure of thermohaline millennial oscillations. J. Clim. 19 (22), 5777e5795.

Crowley, T.J., 1992. North Atlantic deep water cools the Southern Hemisphere. Paleoceanography 7 (4), 489e497.

Crucifix, M., 2012. Oscillators and relaxation phenomena in Pleistocene climate theory. Phil. Trans. R. Soc. A 370, 1140e1165.

Crucifix, M., 2011. How can a glacial inception be predicted? Holocene 21, 831e 842.

De Saedeleer, B., Crucifix, M., Wieczorek, S., 2013. Is the astronomical forcing a reliable and unique pacemaker for climate? A conceptual model study. Clim. Dyn. 40 (1e2), 273e294.

Egger, J., 1999. Internal fluctuations in an oceaneatmosphere box model with sea ice. Clim. Dyn. 15, 595e604.

El-Kibbi, M. & Rial, J. A. An outsider's review of the astronomical theory of the climate. Earth Sci. Rev. 56, 161–177 (2001).

EPICA Community Members, 2006. One-to-one coupling of glacial climate vari- ability in Greenland and Antarctica. Nature 444, 195e198.

Feliks, Y., Ghil, M., Robertson, A.W., 2010. Oscillatory climate modes in the Eastern Mediterranean and their synchronization with the North Atlantic Oscillation. J. Clim. 23 (15), 4060e4079.

Gabor, D., 1946. Theory of Communication. Part 1: The analysis of information: Electrical EngineersePart III: Radio and Communication Engineering. J. Inst. 93 (26), 429e444.

Ganopolski, A., Calov, R., 2011. The role of orbital forcing, carbon dioxide and regolith in 100 kyr glacial cycles. Clim. Past 7, 1415e1425.

Gildor, H., Tziperman, E., 2001. Physical mechanisms behind biogeochemical glacial-interglacial CO2 variations. Geophys. Res. Lett. 28, 2421e2424.

Gloersen, P., Huang, N., 2003. Comparison of interannual intrinsic modes in hemispheric sea ice covers and other geophysical parameters. IEEE Trans. Geosci. Remote Sens. 41 (5), 1062e1074.

Golyandina, N., Nekrutkin, V., Zhigljavsky, A., 2001. Analysis of Time Series Struc- ture: SSA and Related Techniques. Chapman and Hall/CRC.

Hinnov, L.A., Schulz, M., Yiou, P., 2002. Interhemispheric space-time attributes of the Dansgaard-Oeschger oscillations between 100 and 0ka. Quater. Sci. Rev. 21, 1213e1228.

Huang, N.E., Shen, Z., Long, S.R., Wu, M.C., Shih, H.H., Zheng, Q., Yen, N.C., Tung, C.C., Liu, H.H., 1998. The empirical mode decomposition and the Hilbert Spectrum for nonlinear and nonstationary time series analysis. Proc. R. Soc. London A 454, 903e995.

Huang, N.E., Wu, Z., 2008. A review on HilberteHuang transform: method and its applications to geophysical studies. Rev. Geophys. 46, RG2006.

Huybers, P., Wunsch, C., 2005. Obliquity pacing of the late Pleistocene glacial terminations. Nature 434, 491e494.

Huygens, Ch, 1673. Horologium Oscillatorium, Apud F. Muguet, Paris, France. En- glish translation; The Pendulum Clock, 1986. Iowa U. Press, Ames.

Källén, E., Crafoord, C., Ghil, M., 1979. Free oscillations in a climate model with ice- sheet dynamics. J. Atmos. Sci. 36 (12), 2292e2303.

Lathi, B. P. & Ding, Z. Modern Digital and Analog Communication Systems (Oxford Univ. Press, 2009).

Lin, Z.S., Wang, S.G., 2006. EMD analysis of solar insolation. Meteorol. Atmos. Phys. 93, 1871e1893.

Lisiecki, L. Links between eccentricity forcing and the 100,000-year glacial cycle. Nature Geosci.3,349–352 (2010).

Lund, D.C., Mix, A.C., 1998. Millennial-scale deep water oscillations: reflections of the North Atlantic in the deep pacific from 10 to 60 ka. Paleoceanography 13, 10e19.

Maraun, D., Kurths, J., 2005. Epochs of phase coherence between El Niño/Southern Oscillation and Indian monsoon. Geophys. Res. Lett. 32, L15709.

Marchal, O., Jackson, C., Nilsson, J., Paul, A., Stocker, T.F., 2007. Buoyancy-driven flow and nature of vertical mixing in a zonally averaged model. In: Schmittner, A., Chiang, J.C.H., Hemming, S.R. (Eds.), Ocean Circulation: Mechanisms and Im- pacts e Past and Future Changes of Meridional Overturning. American Geophysical Union, Washington, D.C.

Marotzke, J., Welander, P., Willebrand, J., 1988. Instability and multiple steady states in a meridional-plane model of the thermohaline circulation. Tellus 40A, 162e 172.

Muller, R. & McDonald, G. Ice Ages and Astronomical Causes: Data, Spectral Analysis and Mechanisms (Springer, 2000).

Oerlemans, J. Milankovitch and Climate, Part 2 (Berger, A. L. et al.) 607–611 (1984).

Oliveira, Henrique M., and Luís V. Melo. "Huygens synchronization of two clocks." *Scientific Reports* 5 (2015).

Osipov, G.V., Hu, B., Zhou, C.S., Ivanchenko, M.V., Kurths, J., 2003. Three types of transitions to phase synchronization in chaotic oscillators. Phys. Rev. Lett. 91, 024101.

Paillard, D., 1998. The timing of Pleistocene glaciations from a simple multiple-state climate model. Nature 391, 378e381.

Paillard, D., Parrenin, F., 2004. The Antarctic ice sheet and the triggering of de- glaciations. Earth Planet. Sci. Lett. 227, 263e271.

Pikovsky, A., Rosenblum, M., Kurths, J., 2001. Synchronization: A Universal Concept in Nonlinear Sciences. Cambridge University Press.

Pisias, N. G. & Moore, T. C. Jr The evolution of the Pleistocene climate: A time series approach. Earth Planet. Sci. Lett. 52, 450–458 (1981).

Raymo, M. E. The timing of major climate terminations. Paleoceanography 12, 577–585 (1997).

Rial, J.A. Pacemaking the ice ages by frequency modulation of Earth's orbital eccentricity. Science 285, 564–568 (1999).

Rial, J.A., 2012. Synchronization of polar climate variability over the last ice age: in search of simple rules at the heart of climate's complexity. Am. J. Sci. 312 (4), 417e448.

Rial, J.A., Oh, J., Reischmann, E., 2013. Synchronization of the climate system to orbital eccentricity insolation and the 100ky problem. Nature Geosci. 6, 289e 293.

Rial, J.A., Saha, R., 2011. Modeling abrupt climate change as the interaction between sea ice extent and mean ocean temperature under orbital insolation forcing. In: Rashid, H., Polyak, L., Mosley-Thompson, E. (Eds.), Abrupt Climate Change: Mechanisms, Patterns, and Impacts, Geophysical Monograph Series, vol. 193, pp. 57e74.

Rial, J.A., Yang, M., 2007. Is the frequency of abrupt climate change modulated by the orbital insolation? In: Schmittner, A., Chiang, J.C.H., Hemming, S.R. (Eds.), Ocean Circulation: Mechanisms and ImpactsdPast and Future Changes of Meridional Overturning, Geophysical Monograph Series, vol. 173, pp. 167e 174.

Ridgwell, A., Watson, A., Raymo, M., 1999. Is the spectral signature of the 100 kyr glacial cycle consistent with a Milankovitch origin. Paleoceanography 14, 437e 440.

Rosenblum, M.G., Pikovsky, A.S., Kurths, J., 1997. From phase to lag synchronization in coupled chaotic oscillators. Phys. Rev. Lett. 78 (22), 4193e4196.

Rulkov, N.F., Sushchik, M.M., Tsimring, L.S., Abarbanel, H.D.I., 1995. Generalized synchronization of chaos in directionally coupled chaotic systems. Phys. Rev. E 51, 980e994.

Saltzman, B., 2002. Dynamical Paleoclimatology: A Generalized Theory of Global Climate Change. Academic Press, San Diego.

Saltzman, B., Maasch, K.A., 1988. Carbon cycle instability as a cause of the Late Pleistocene Ice Age Oscillations: modeling the asymmetric response. Global Biogeochem. Cycl. 2 (2), 177e185.

Saltzman, B., Moritz, R., 1980. A time-dependent climatic feedback system involving sea-ice extent, ocean temperature, and CO2. Tellus 32, 93e118.

Saltzman, B., Sutera, A., 1984. A model of the internal feedback system involved in late quaternary climatic variations. J. Atmos. Sci. 41, 736e745.

Saltzman, B., Sutera, A., Evenson, A., 1981. Structural stochastic stability of a simple auto-oscillatory climate feedback system. J. Atmos. Sci. 38, 494e503.

Schulz, M., Paul, A., Timmermann, A., 2004. Glacialeinterglacial contrast in climate variability at centennial-to- millennial timescales: observations and conceptual model. Quater. Sci. Rev. 23, 2219e2230.

Sole, J., Turiel, A., Llebot, J.E., 2007. Using empirical mode decomposition to corre- late paleoclimatic time-series. Nat. Hazards Earth Syst. Sci. 7, 299e307.

Steig, E.J., 2006. Climate change: the southenorth connection. Nature 444, 152e 153.

Stenni, B., Masson-Delmotte, V., Selmo, E., Oerter, H., Meyer, H., Röthlisberger, R., Jouzel, J., Cattani, O., Falourd, S., Fischer, H., Hoffmann, G., Iacumin, P., Johnsen, S.J., Minster, B., Udisti, R., 2003. The deuterium excess records of EPICA Dome C and Dronning Maud Land ice cores (East Antarctica). Quarter. Sci. Rev. 29, 146e159.

Stommel, H., 2010. Thermohaline convection with two stable regimes of flow. Tellus 13 (2), 224e230.

Strogatz, Steven. *Sync: The emerging science of spontaneous order*. Hyperion, 2003.

Sun, J., Hong, X., Tong, S., 2012. Phase synchronization analysis of EEG signals: an evaluation based on surrogate tests. IEEE Trans. Biomed. Eng. 59 (8), 2254e 2263.

Theiler, J., Eubank, S., Longtin, A., Galdrikian, B., Farmer, J.D., 1992. Testing for nonlinearity in time series: the method of surrogate data. Phys. D 58 (1e4), 77e 94.

Tsonis, A.A., Swanson, K., Kravtsov, S., 2007. A new dynamical mechanism for major climate shifts. Geophys. Res. Lett. 34, L13705.

Tziperman, E., Raymo, M., Huybers, P. & Wunsch, C. Consequences of pacing the Pleistocene 100kyr ice ages by nonlinear phase locking to Milankovitch forcing. Paleoceanography 21, PA4206 (2006).

Van der Pol, B. Frequency Modulation. Proc. Inst. Radio Eng. 18, 1194–1205 (1930).

Vautard, R., Ghil, M., 1989. Singular spectrum analysis in nonlinear dynamics, with applications to paleoclimatic time series. Phys. D 35, 395e424.

Yang, J., Neelin, J.D., 1993. Sea-ice interaction and the stability of the thermohaline circulation. Atmos. Ocean 35, 433e469.

Zhang, S., Lin, C.A., Greatbatch, R.J., 1995. A decadal oscillation due to the coupling between an ocean circulation model and a thermodynamic sea-ice model. J. Mar. Res. 53, 79e106.

CHAPTER 2: DETECTING THE THERMOHALINE CIRCULATION'S PERIODICITY: HOW POLAR PALEOCLIMATES COMMUNICATE [3]

Introduction: Previous studies have empirically identified a plausible dynamic connection between the Polar Regions climates since the last ice age, but the mechanism(s) responsible remains elusive. Recent works have identified synchronization of the polar climate oscillators as a possible mechanism, based on the constant relative phase of their proxy time series throughout most of the last glaciation. Consequently, one pole's millennial-scale climatic time series can be approximately transformed into that of the other pole through a linear mathematical operator. Here we show that, if each stable isotope proxy time series can therefore be thought of as the input and/or output of an unknown transfer function that couples two synchronized oscillators, ad-hoc spectral deconvolution techniques can be used to estimate this transfer function, i.e. the operator which converts one polar signal into the other. After special attention is paid to the reliability of the proxies' relative chronologies, the deconvolution reveals two, equally possible, directionally-dependent transfer functions, one of which exhibits a predominant 1.67 ky period, consistent with the oft-suggested, but as yet unproven, periodical, millennial-scale oscillations of the ocean/atmosphere system. As far as we know, this is the first time that a deconvolution involving data from both poles has been attempted to better understand polar climate connectivity. We discuss the possibility that the Thermohaline Circulation is one plausible

---

physical mechanism of connection, which could drive polar communication through temperature and gas exchange.

The mechanism(s) of polar climate connection remains a fundamental question of polar dynamics (EPICA Community Members, 2006; Broeker, 1998; Steig, 2006; Rial, 2012). The bi-polar seesaw, one of the forefront proposed models of connection, was the first published solution, stating that the two polar climates oscillate in direct opposition, which was later refined by Broecker (1998) and has been expanded to consider the necessary dynamics of heat and fresh water signals that could create the anti-phase oscillation (Stocker et al., 2003). EPICA Community Members discuss a 'one-to-one' relationship between Antarctic warming and stadial Greenland in support of the bipolar seesaw (Epica Community Members, 2006). However, new, high resolution data is more consistent with a $\pi/2$ phase shift (Oh et al., 2014), which has since been shown to be stable for the duration of the available $\delta^{18}O$ ice core records with inter-comparable age models (Rial, 2012, Oh et al., 2014). Additionally, the quasi-periodic major climate change events, such as the Heinrich events and Dansgaard-Oescher oscillations (Ditlevsen et al., 2007), are not well explained by the mechanism of the bipolar seesaw, further motivating the hypothesis of polar synchronization and the exploration of polar climate connections under this paradigm.

The observed phase and frequency lock of the polar climates' proxy records for nearly the entire length of the last glaciation is strong evidence for polar synchronization. However, identifying synchronization requires carefully quantified relative phase difference calculations between the polar records, complicated by timing errors, noise, and varying age models used by individual researchers (Veres et al., 2013). Two recent methods of dating have made vast strides

60

in narrowing these inconsistencies of age models between proxy records at both poles: the methane matched model method, which establishes better relative ages between the poles, (Oh et al, 2014; Blunier et al., 2007) and the AICC 2012 age model, which refines absolute ages in southern cores in a standardized manner, and ties them to a northern core (Veres et al., 2013). In this paper, we examine the results from the methane matched age model due to the focus of this study on the relationship between the poles, prioritizing relative ages (Oh et al., 2014). While the ice cores available from AICC 2012 have also been analyzed, and found to show comparable spectral peaks, the methods used to narrow absolute dates do not specifically focus on the pole to pole relationship, increasing the potential for error in the transfer function (see Supplemental Information for details).

Using methane matched base pairs (Blunier et al., 2007), we obtained seven primary cores (three Greenland and four Antarctic) with 12 possible N-S combinations of isotope climate proxy records, interpolated to 50 yr intervals and matched via the Monte Carlo method (Oh et al., 2014). Milankovitch-related (longer than 10kyr) and high frequency noise (shorter than 100 years) signals were removed before deconvolving the pairs from each other, creating north-to-south and south-to-north transfer function sets for each pair. These cores and the specific pairs are listed in Figure 1.
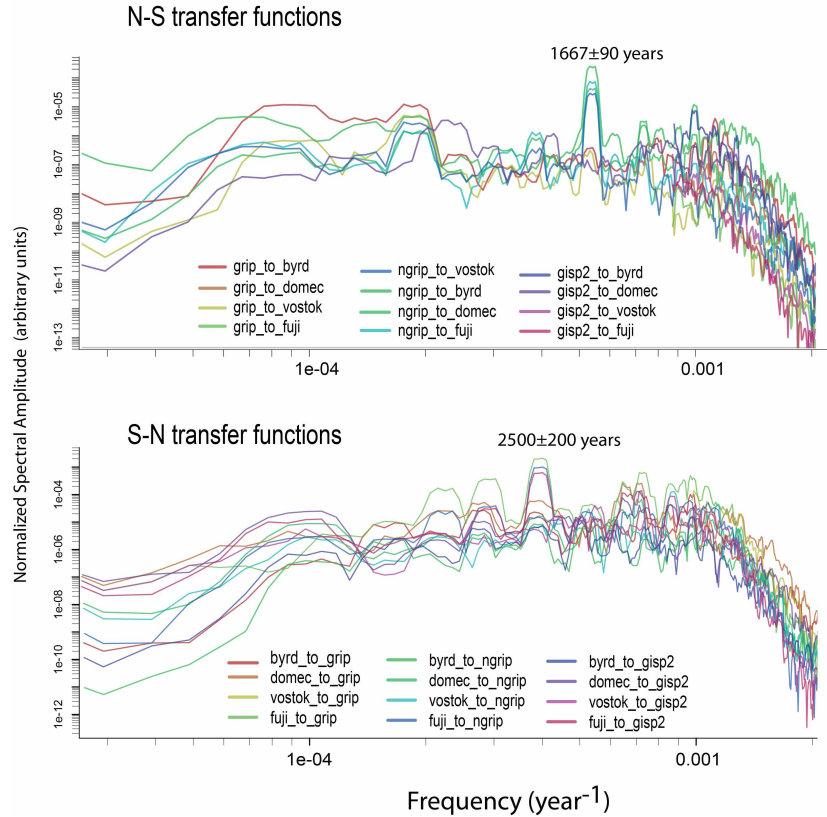
Figure 2.1: Spectra of the transfer functions (spectral ratios) obtained from the deconvolution of the twelve combinations of Greenland and Antarctica time series (GISP2, GRIP and NGRIP from Greenland and Byrd, DomeC, Vostok and Fuji from Antarctica) whose age models have been matched using a combination of methane-matching and Monte Carlo estimation, plotted in loglog (Oh et al., 2014). The stronger spectral peaks at 1667±90 years and at 2500±200 years are highlighted. All the 12 different combinations of records from Greenland and Antarctica were used to generate 24 transfer functions (12 N-S and 12 S-N). Here the damped least-squares deconvolution regularization method (Dimri, 1992) is used for all the cases shown. All the regularization methods used produce similar results. Spectra are calculated using the multi-taper method (MTM) with three tapers. The linear plot can be seen in Supplemental Figure 3.

Spectral deconvolution is a simple mathematical operation, often applied in electronics and seismology. Here, we call *a(t)* and *g(t)* any pair of Antarctic and Greenland records, respectively. We call *A(w)* and *G(w)* their respective Fourier spectra and *w* the circular

frequency. We assume that $a(t) = h(t) \otimes g(t)$ and $g(t) = s(t) \otimes a(t)$, where $h(t)$ is the North-South transfer function, $s(t)$ is the South-North transfer function and $\otimes$ stands for the convolution operation. In the frequency domain convolution translates into spectral product and so $A(w)=H(w)G(w)$ and $G(w)=S(w)A(w)$. Therefore, spectral deconvolution means that $H(w)=A(w)/G(w)=1/S(w)$, where $H(w)$ and $S(w)$ are the Fourier spectra of the N-S and S-N transfer functions respectively. Five separate methods of deconvolution regularization were applied and tested to identify robust, stable power spectra (see Supplemental Figure 1 and 2 for details and examples) (Dimri, 1992; Aster et al., 2013).

Note that the direction of the deconvolved transfer function is determined by which polar record is used for numerator or denominator in the deconvolution (Dimri, 1992). The resulting time series obtained by Fourier inversion are assumed to represent the 'transfer functions' between the oscillations of the polar climates, and can be thought of as a measure of the dynamic teleconnection between the poles. Significant spectral peaks from both transfer function directions are noted in Figure 1 for reference.

Remarkably, all deconvolutions result in power spectra with clear frequency peaks depending on whether they are N-S or S-N spectral ratios, as seen in Figure 1. The deconvolved spectra exhibit strong spectral peaks at periods of 2.5±0.2, 1.89±0.06, 1.4±0.1and 1±0.1 kyrs in the south to north transfer function (the first of which may be attributed to solar forcing signals, and is not strongly present in all pairs (Usoskin, 2008)), while the north to south exhibits a single, strong peak at 1.67±0.09 with secondary peaks at 1.3 ±0.06 and 1.1±0.09kyrs. All listed peaks are above the 95% confidence interval. While spectral amplitudes vary across pairs, peak locations remain the same, as do the nearly sinusoidal nature of the north to south transfer

functions in the time domain (see Figure 2, Supplemental Figures 1, 2 and 3). The strong, stable peak in the N-S spectra is associated with a prominent spectral hole present in the Greenland records (predominantly in NGRIP, see Supplemental Figure 1) but is nearly completely absent from the Antarctic records. The simplicity of their time series, and the relative signal to noise (S/N) ratios of the two transfer functions for each pair allows us to tentatively select the N-S transfer functions for further study, and, for the interested reader, details of the S-N transfer may be inspected in all Supplemental Data Figures. Geographically intermediate data could be identified in order to clarify the directionality of the signal and significance of spectral peaks, but do not currently exist in a comparable resolution or with an adequate age model.
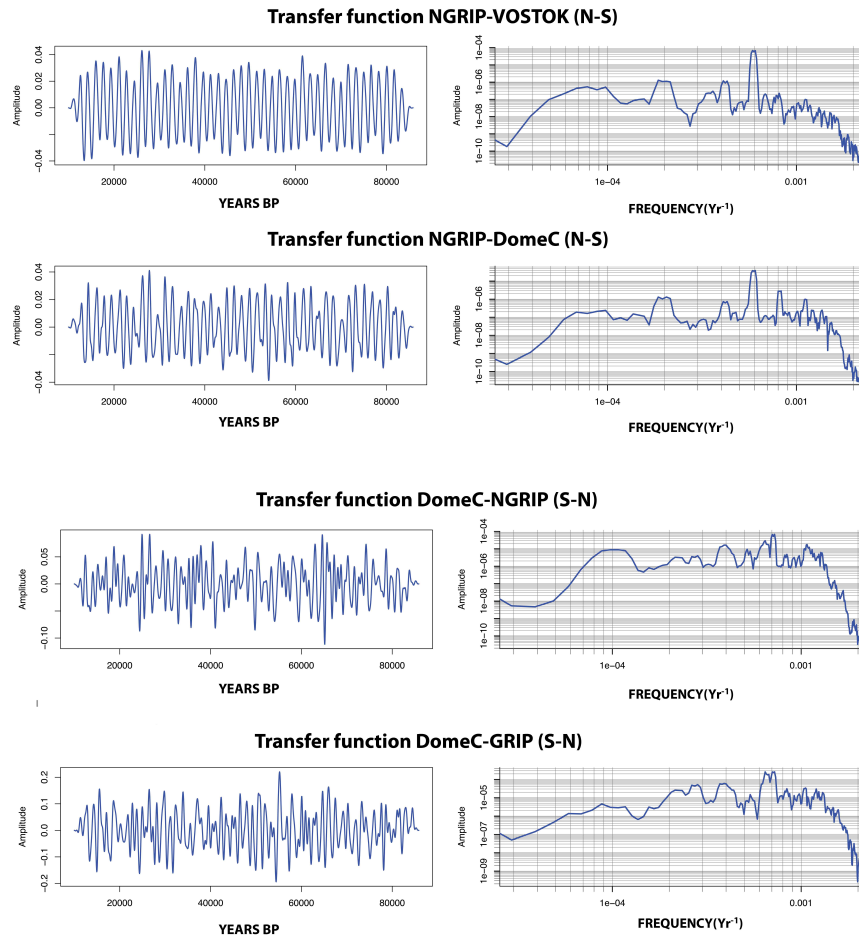
Figure 2.2: Selected time-domain transfer functions (left and their spectra (right) from Figure 1. In the N-S functions, the spectrum of Greenland's NGRIP is the denominator and in the S-N functions, Antarctica's DomeC is the denominator of the spectral ratio. The strong power peak at 1.67±0.09ky is the main characteristic of the N-S transfer function (see Figure 1). In the S-N transfer functions, a broad peak is centered at 1.4±0.1ky, another at 1.8kyrs, and a less prominent one at 2.5±0.2ky. The time series of the middle pair can be seen in Supplemental Figure 4.

The predominant periodicities of the transfer functions offer constraints to the potential processes of connection. Specifically, only two, nearly monochromatic oscillations with

periodicities close to the highly coherent N-S 1.67kyr signal have been identified in the paleoclimate literature: the Keeling tidal cycle and the Thermohaline Circulation (THC). The Keeling tidal cycle is a minor harmonic of orbital cycles, creating an oscillation of tidal strength with a proposed 1.8kyr periodicity, which is also comparable to the 1.89kyr signal in the S-N signal. Though it is possible that the asymmetric distribution of the polar oceans could result in modification of upwelling intensity within the oceans, leading to pole-to-pole propagation of energy, a strong influence from this tidal forcing should be visible in the individual polar climate records, but is not. Indeed, the level of significance of this harmonic of the tidal cycles is still controversial (Keeling, 2000; Munk, 2002), as a possible signature of its periodicity has not been conclusively identified in existing records. Conversely, the influence of the THC in polar climates has been widely suggested in a variety of datasets.

The THC refers to the part of ocean circulation controlled by density differences, specifically variations in temperature and salinity (Rahmstorf, 2006; Dima, 2009; Kuhlbrodt, 2009). Most models agree that the main driver of this circulation is high latitude deep-water formation, specifically, the formation of very cold, high salinity water masses at the high latitudes. Models do not agree on intermediate mechanisms of overturning, precise paths, or even exact periodicities of circulation (Rahmstorf, 2006; Schmitz, 1995). Data suggests that the THC has persisted in some mode for the duration of recorded circulation, leading to models of the circulation as a self-sustaining oscillation, created by the nonlinear convection processes (Verdière et al., 2006). It has also previously been cited as an important connection between ocean basins (Schmitz, 1995), with any variations, natural or anthropogenic, having widespread

theoretical consequences for the global climate (Rahmstorf, 2006; Latif et al., 2000; Stouffer et al., 2006).

Published periodicities for the THC are usually ~1.5±.5kyrs, supported by the appearance of this periodicity in numerous data sets. Specifically, for the last three decades (Ditlevsen, 2007; Pestiaux et al., 1988; Hinnov et al., 2002; Holger et al.; Obrochta et al., 2012), an extensive literature has accumulated on observations of millennial-scale periodic oscillations in sediment cores, cave records, lake pollen and ice cores covering the Holocene and the last ice age. These oscillations have largely been attributed to the THC.

However, no published data set provides conclusive evidence for the continuous existence, path or period of the THC, or the connection of climate proxy time series to the THC. In contrast, this study shows a nearly monochromatic N-S transfer function with a 1.67kyr period, which is in the range of the published body of data attributed to the THC. This signal is stable for the length of the record, and visible in the relationship between the two poles, but not in individual polar climate proxy time series. The periodicity and the un-damped character of this signal suggests that the calculated transfer functions could be proxies of the internally driven, simple, monochromatic, minimally damped oscillation (Verdière, 2006), likely caused by energy imbalance between the advection of cold water and the diffusion of heat by vertical turbulent mixing in the high latitude deep ocean. The THC is therefore a plausible candidate for the driving mechanism of climate signal information transfer between the poles.

Not only is the THC a potential carrier of temperature and salinity signals, it is also a carrier of dissolved CO_2, a signal which may be sequestered and released at varying rates based on the mixing stratification at either pole, as well as the gradient of gases and temperature at the ocean/atmosphere boundary of upwelling regions. This signal has been cited as having a large impact on major polar climate change events in the distant past on a much longer time scale than this study (Ridgewell et al., 2014). Two out of three of the traditional carbon pumps are affected by changes in temperature, sea ice, and salinity, allowing the dissolved CO_2 signal to follow changes in the polar climates, and to be transmitted through the major down welling regions at the poles (Ridgewell et al., 2014). In this manner, the THC is theoretically able to transmit, store and release polar climate information forcing signals, best preserved in the North to South direction, given the lack of upwelling regions in this path.

It is also worth noting that the predominant periodicities in both directions loosely fit a sub-harmonic relationship. That is, if we identify $F_0=1/5000y$ as a 'fundamental' frequency, then its harmonics are $2F_0=F_1=1/2500y$, $3F_0=F_2=1/1667y$, $4F_0 =F_3=1/1250y$, and $5F_0=F_4=1/1000y$. Frequencies within a hundred years of each harmonic F_0, F_1, F_2, F_3, and F_4 have been identified in our transfer functions, which is generally within the potential error range given the prioritization of relative ages over absolute in our dataset (Blunier et al., 2007). However, the physical mechanism underlying this relationship, and the origin of the fundamental frequency F_0 remain unknown.

As stated earlier, intermediate climate data series are necessary to make more definitive statements about the potential path and mechanism of transfer within the THC, and to verify the

presence of the THC in the transfer functions. These intermediate proxies would allow us to begin to reconstruct various layers of ocean temperature, circulation, and dissolved gas concentrations. Ideally, further stable phase relationships between the polar records and sediment core proxy records, or between individual sediment core proxy records, would allow for the use of synchronization and deconvolution analysis to trace the signal through the deep ocean and surface waters. Unlike the ice cores, however, sediment core age models have not yet been refined thoroughly enough to allow for accurate phase relationship analysis on the scale of single millennia. Low, irregular sampling rates, unreported age model uncertainties, wide variation between investigator-specific tuning methods, and even proxy calibration uncertainties, create potential errors which currently negate the use of inter-sediment core comparison (Hinnov et al., 2002; Obrochta et al., 2012; Darby et al., 2012).

This study shows evidence of the potential existence of a nearly monochromatic, minimally damped, periodic, inter-polar climate signal transfer via an analysis method (spectral deconvolution) that does not assume the presence of the THC. Preliminary modeling using the coupled sea-ice/ocean-temperature, Saltzman-based model, as modified by Rial (2011, 2012) shows markedly similar results when the model's coupling parameter allows for the characteristic pi/2 phase relationship (see Supplemental Figures 5,6). Further work will pursue a standardized, unified age model for oceanic sediment cores with a known uncertainty in pursuit of a better quantifying the major mechanisms of long-term climate information and energy transfer through the deep oceans, which in turn will allow for more detailed, accurate models. Creating a larger, globally-comparable, proxy database would improve understanding of polar climate interactions, better resolve the transfer path and the effects of regional variations on

climate signal transfer, as well as better informing us about the future impacts of changing THC temperature, path, and dissolved CO_2 concentrations.

Figures S1-S4
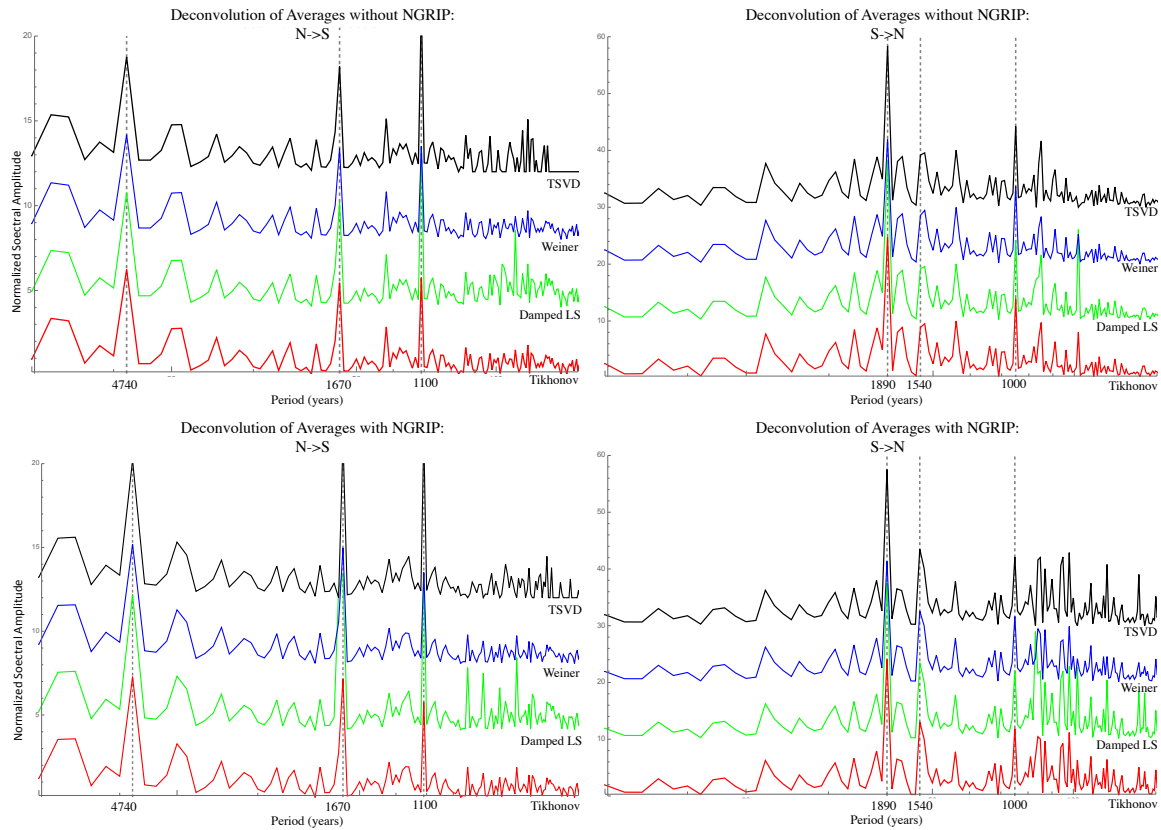
Supplemental Figure 2.1: Due to the prominent spectral hole in NGRIP, row one shows the spectra of the transfer functions of the deconvolution of the methane-matched northern cores averaged without NGRIP from all methane-matched southern cores averaged, north to south in column one and south to north in column two. Four methods of regularization are plotted to show robustness between methods. The second row shows the same, but with the NGRIP time series, showing that though NGRIP shows the strongest spectral hole at 1.67kyrs, all matched data sets produce the same peak. North to south transfer functions show peaks at periods of 4.75, 1.67, and 1.1kyrs. The south to north transfer function spectra contains significant peaks at 1.89, 1.54 and 1 kyrs, with smaller peaks at 2.5 and 1.4kyrs not highlighted, but above the 95% confidence interval for the dataset.
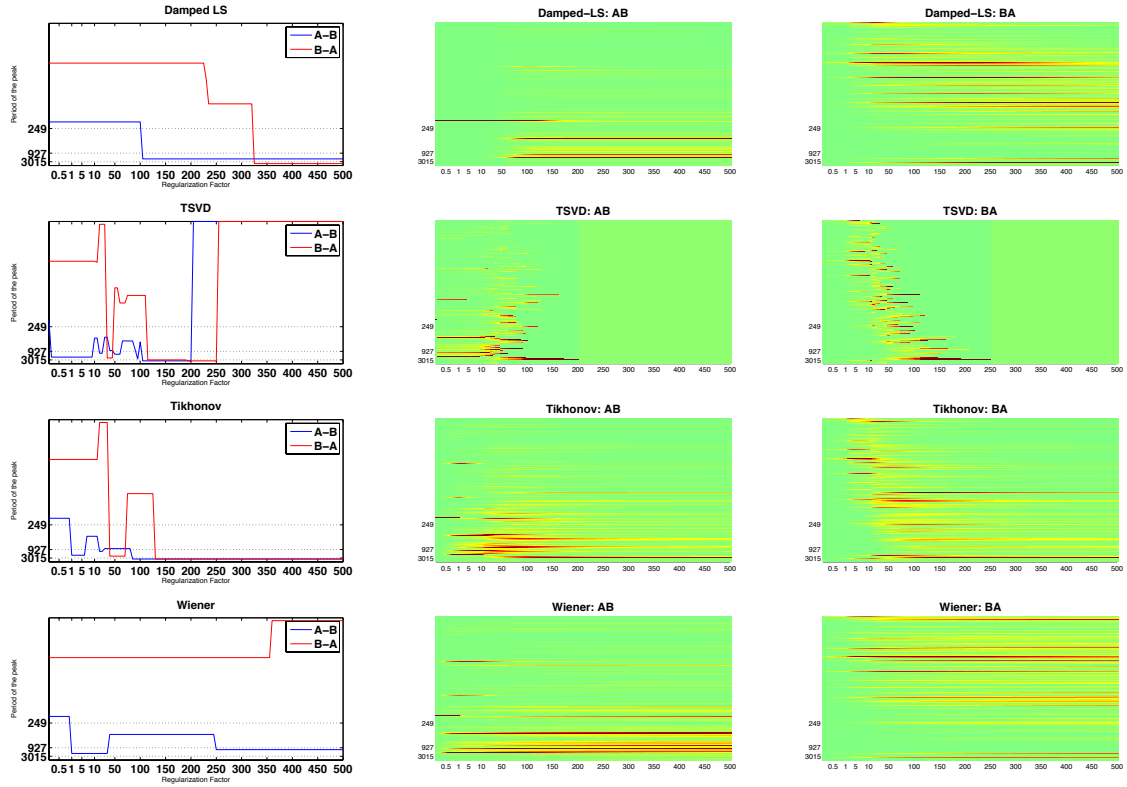
Supplemental Figure 2.2: Deconvolution regularization results for the DomeC and NGrip cores. The first column shows the value of the main power peak present at that regularization factor (along the x axis), while the second two columns show the entire spectrum of results (along the y axis) over the regularization factors of all 4 regularization methods, where red denotes significant peak values, in both directions in the south to north and north to south directions. The clear continuity of peaks in significant period ranges show the robustness of our results, while length of these signals also show the different effects of identical regularization factors across methods.

Spectra of south to north transfer functions

Spectra of north to south transfer functions
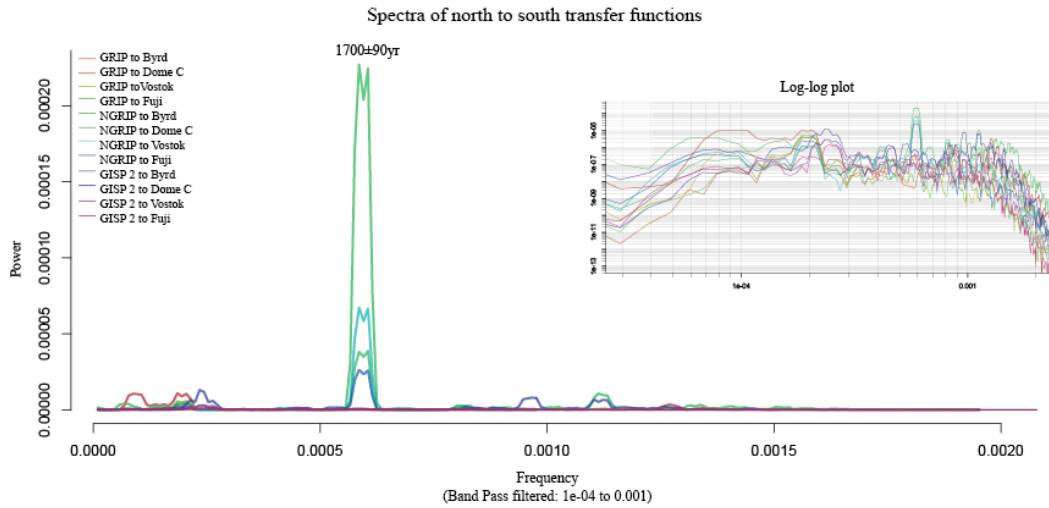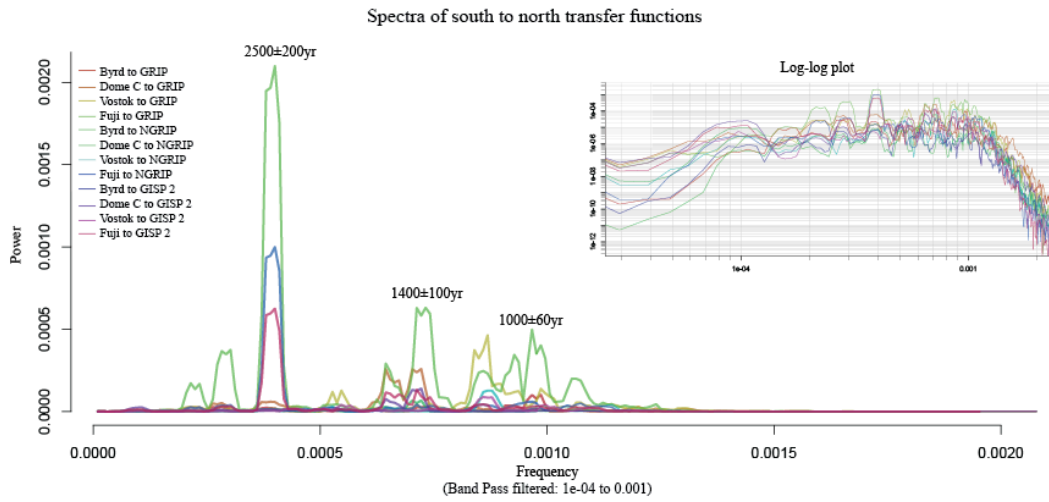
Supplemental Figure 2.3: Linear plots of Figure 1's multi-taper spectra of the DLS regularized, deconvolved transfer functions obtained from each of the pairs of records named. The inset shows the log-log plot from the main text for further signal-to-noise comparison. The spectra of the N-to-S transfer functions are strongly peaked at 1.7 ky, while the spectra of the S-to-N transfer functions show prominent power peaks at 2.5 ky, 1.4 ky and 1ky. The peaks appear robust for the entirety of the available record.
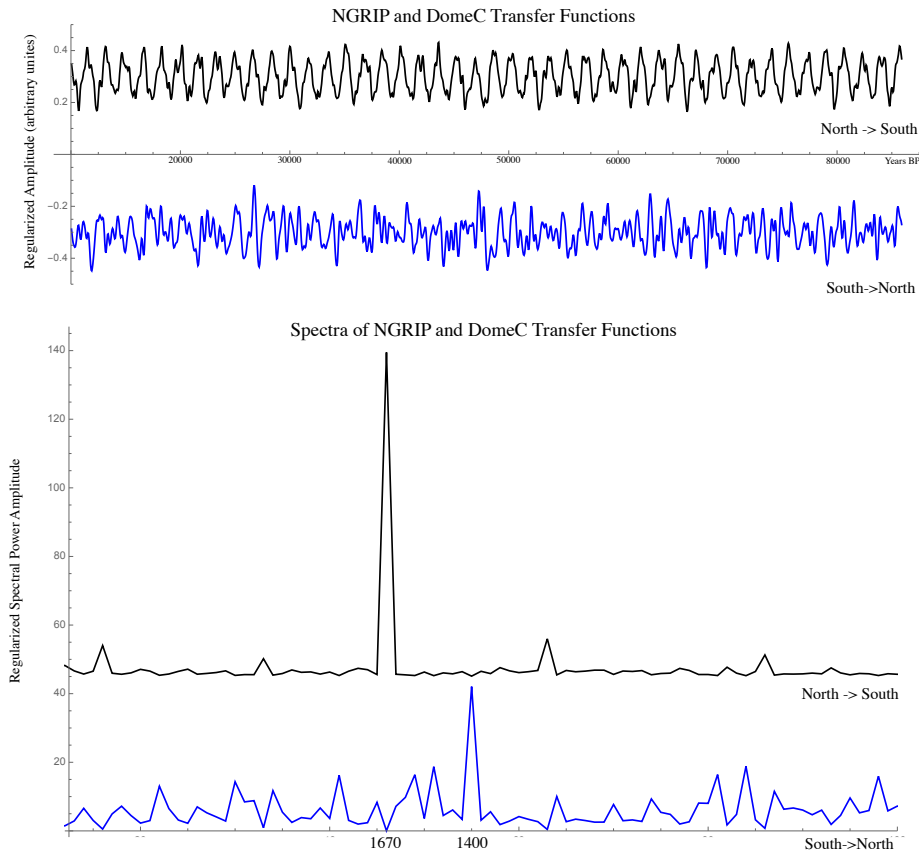
Supplemental Figure 2.4: The figure above shows the time series of one set of the transfer function spectra shown in the main text Figure 2, but makes use of FFT spectral decomposition for a better comparison with Supplemental Figure 1. FFT creates narrower spectral peaks, thus missing some of the possible power spreading but preserving significant frequency spikes. This pair is one of the simplest spectra, largely due to the use of NGRIP in the deconvolution, but is representative of the time domain transfer functions. The main spectral peaks for each spectra are centered at 1.67 and 1.4kyrs.

74
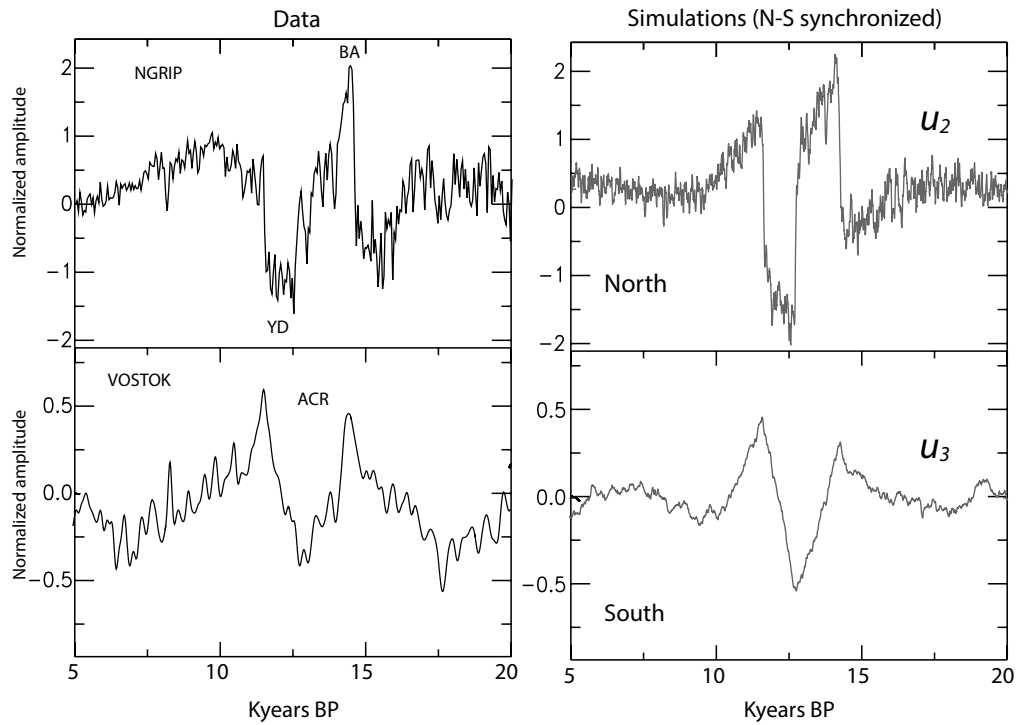
Supplemental Figure 2.5: Data and modeled data from the adapted Saltzman model as used in Rial and Saha (2011), including the coefficient of connection to represent synchronization. Shown here are 5-20 kyrs of data, demonstrating close fit through significant events.

Model Deconvolution Transfer Function

North from South

South from North

Transfer Function Spectra

Highlighted Periods: 3750, 1364,1250,833,625,600 yrs
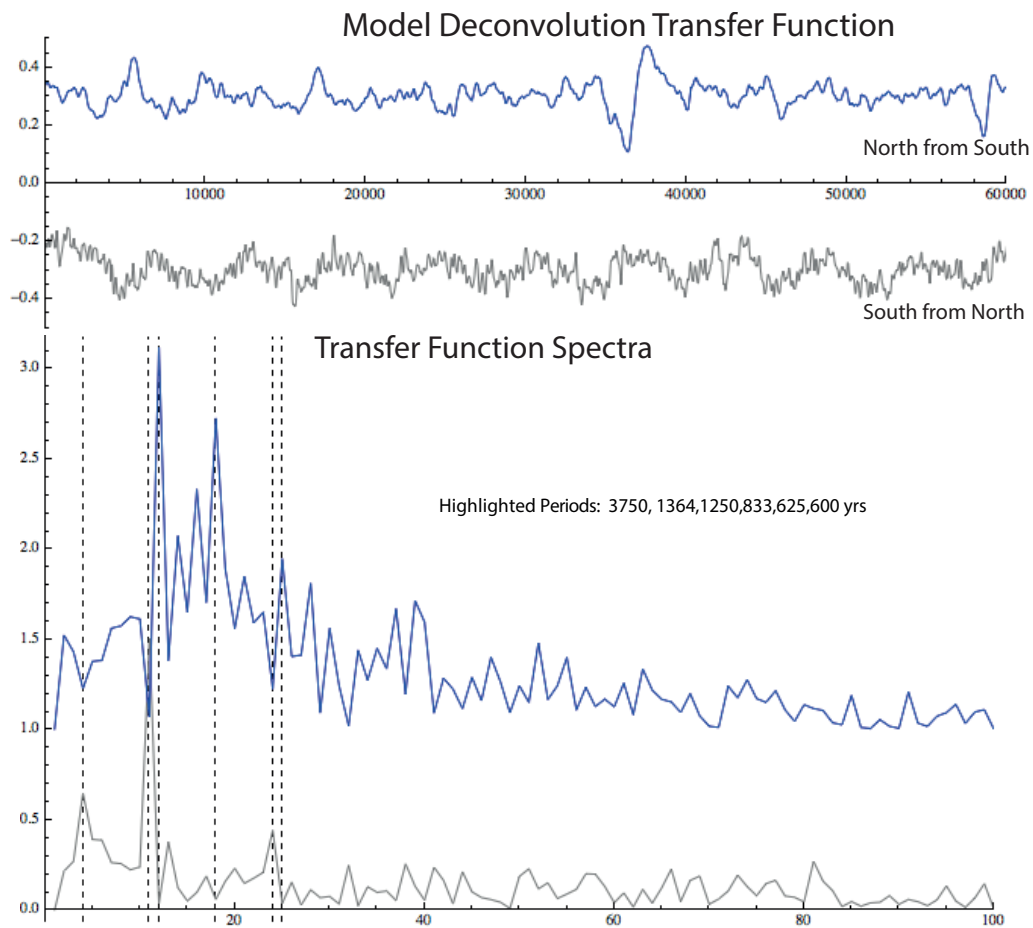
Supplemental Figure 2.6: Transfer functions and deconvolution spectra for the deconvolution of modeled data in Figure S5, with main spectral peaks highlighted. Without the assumption of a THC included in the model, frequencies within the range of the transfer functions seen in the data are recovered. These persist in all best fit runs of the model, indicating that in order to replicate the behavior seen in the records, a transfer of this period is needed, though the model lacks specific physical parameters to define how this transfer operates.

REFERENCES

Aster, R. C., B. Borchers, and C. H. Thurber. *Parameter estimation and inverse problems*. Academic Press, 2013.

Blunier, T., R. Spahni, J.M. Barnola et al. "Synchronization of ice core records via atmospheric gases." Climate of the Past Discussions 3.1 (2007): pp. 365-381.

Bond, Gerard, et al. "A pervasive millennial-scale cycle in North Atlantic Holocene and glacial climates." *Science* 278.5341 (1997): 1257-1266.

Bond, Gerard, et al. "Persistent solar influence on North Atlantic climate during the Holocene." *Science* 294.5549 (2001): 2130-2136.

Braun, Holger, et al. "Possible solar origin of the 1,470-year glacial climate cycle demonstrated in a coupled model." *Nature* 438.7065 (2005): 208-211.

Broecker, W.S. "Paleocean circulation during the last deglaciation: a bipolar seesaw?" *Paleoceanography*, 13 (2) (1998), pp. 119–121.

Bryan, F., *Parameter sensitivity of primitive equation ocean general circulation models.* Journal of Physical Oceanography, 1987. 17: p. 970-985.

Darby, D. A., et al. "1,500-year cycle in the Arctic Oscillation identified in Holocene Arctic sea-ice drift." *Nature Geoscience* 5.12 (2012): 897-900.

Dima, M., & Lohmann, G. (2009). Conceptual model for millennial climate variability: a possible combined solar-thermohaline circulation origin for the~ 1,500-year cycle. *Climate Dynamics*, *32*(2-3), 301-311.

EPICA Community Members. "One-to-one coupling of glacial climate variability in Greenland and Antarctica," *Nature*, 444 (2006), pp. 195–198.

Dimri, V., *Deconvolution and inverse theory: Application to geophysical problems*. Elsevier (1992).

Ditlevsen, P. D., Katrine K. Andersen, and Anders Svensson. "The DO-climate events are probably noise induced: statistical investigation of the claimed 1470 years cycle." *Climate of the Past* 3.1 (2007): 129-134.

Ganachaud, A., and Carl Wunsch. "Improved estimates of global ocean circulation, heat transport and mixing from hydrographic data." *Nature* 408.6811 (2000): 453-457.

Hinnov, Linda A., Michael Schulz, and Pascal Yiou. "Interhemispheric space–time attributes of the Dansgaard–Oeschger oscillations between 100 and 0ka." *Quaternary Science Reviews* 21.10 (2002): 1213-1228.

Keeling, C.D., and Timothy P. Whorf. "The 1,800-year oceanic tidal cycle: A possible cause of rapid climate change." *Proceedings of the National Academy of Sciences* 97.8 (2000): 3814-3819.

Kuhlbrodt, T., Rahmstorf, S., Zickfeld, K., Vikebø, F. B., Sundby, S., Hofmann, M., ... & Jaeger, C. (2009). An integrated assessment of changes in the thermohaline circulation. *Climatic Change*, *96*(4), 489-537.

Latif, M., et al., *Tropical stabilization of the thermohaline circulation in a greenhouse warming simulation.* Journal of Climate, 2000. 13(11): p. 1809-1813.

Munk, Walter, Matthew Dzieciuch, and Steven Jayne. "Millennial climate variability: Is there a tidal connection?." *Journal of Climate* 15.4 (2002): 370-385.

Obrochta, S. P., et al. "A re-examination of evidence for the North Atlantic "1500-year cycle" at Site 609." *Quaternary Science Reviews* 55 (2012): 23-33.

Oh, J., E. Reischmann, and J. A. Rial. "Polar Synchronization and the Synchronized Climatic History of Greenland and Antarctica." Quaternary Science Reviews 83 (January 1, 2014):, pp. 129–142.

Pestiaux, P., et al. "Paleoclimatic variability at frequencies ranging from 1 cycle per 10 000 years to 1 cycle per 1000 years: Evidence for nonlinear behaviour of the climate system." *Climatic Change* 12.1 (1988): 9-37.

Pikovsky, A., M. Rosenblum, J. Kurths. *Synchronization: A Universal Concept in Nonlinear Sciences.* Cambridge University Press (2001).

Rahmstorf, S.."Thermohaline Ocean Circulation." *Encyclopedia of Quaternary Sciences*, Edited by S. A. Elias. Elsevier, Amsterdam (2006).

Rial, J.A.. "Synchronization of polar climate variability over the last ice age: in search of simple rules at the heart of climate's complexity."Am. J. Sci., 312 (4) (2012), pp. 417–448.

Rial, J. A., and R. Saha. "Modeling Abrupt Climate Change as the Interaction Between Sea Ice Extent and Mean Ocean Temperature Under Orbital Insolation Forcing." *Abrupt Climate Change: Mechanisms, Patterns, and Impacts* (2011): 57–74.

Ridgwell, A., and S. Arndt, Why Dissolved Organics Matter: DOC in Ancient Oceans and Past Climate Change, in: Biogeochemistry of Marine Dissolved Organic Matter Eds. Hansell, D. A., and C. A. Carlson, Elsevier (2014).

Schmitz, W. J.. "On the interbasin-scale thermohaline circulation." *Reviews of Geophysics* 33, no. 2 (1995): pp. 151-173.

Steig, E.J.. "Climate change: the south–north connection," *Nature*, 444 (2006), pp. 152–153.

Stocker, T. F., and S. J. Johnsen, "A minimum thermodynamic model for the bipolar seesaw," *Paleoceanography*, *18*(4) (2003): pp. 1087.

Stouffer, Ronald J., et al. "Investigating the causes of the response of the thermohaline circulation to past and future climate changes." *Journal of Climate* 19.8 (2006): 1365-1387.

Usoskin, I. G.. "A history of solar activity over millennia." *arXiv preprint arXiv:0810.3972* (2008).

Verdière, C., A. M. Ben Jelloul, and F. Sévellec. "Bifurcation structure of thermohaline millennial oscillations." *Journal of climate* 19.22 (2006): 5777-5795.

Veres, D., L. Bazin, A. Landais, Mahamadou Kele, H. Toyé, B. Lemieux-Dudon, F. Parrenin et al. "The Antarctic ice core chronology (AICC2012): an optimized multi-parameter and multi-site dating approach for the last 120 thousand years." *Climate of the Past* 9, no. 4 (2013).

CHAPTER 3: SYNCHRONIZED DIPOLE-LIKE SEA SURFACE TEMPERATURE
OSCILLATIONS IN THE SOUTHERN HEMISPHERE[4]

Introduction: Dipole behavior of ocean-atmosphere variability has been widely studied due to

the apparent impact of these teleconnections on regional climates, including the monsoon

patterns associated with the Indian Ocean Dipole. This study presents evidence of previously

unstudied dipole modes identified via cross correlation analysis of two sea surface temperature

anomaly data sets, whose details are further informed by empirical orthogonal function analysis.

These dipoles have inter-annual periodicity, with seasonal and monthly variability. Here, a

dipole is defined as a quasi-periodic oscillation between positive and negative phases in sea

surface temperature. We derive a dipole mode index for each identified dipole in order to

quantify the relationship between sea surface temperature, wind, pressure and precipitation

proxies as we seek to characterize the internal dynamics and regional impacts of these systems.

The findings of this study provide a more precise understanding of the globally distributed sea

surface temperature anomaly teleconnections and their associated synchronized climate

dynamics, specifically significant precipitation anomaly patterns over South America and

Australia, using a novel combination of analysis methods.

Coupled ocean-atmosphere variability systems and teleconnections thereof have

traditionally been studied by defining and analyzing simplified climate indices (Talley, 2011).

---

[4] This chapter has been submitted to the International Journal of Climatology. The original citation is as follows:
Reischmann, E.R., E.K. Wise, J.A. Rial. Synchronized Dipole-like Sea Surface Temperature Oscillations in the
Southern Hemisphere, International Journal of Climatology. (Submitted)

These indices seek to establish basic time series characterizing dominant climate variability signals and may describe any number of proxies in a variety of couplings, including sea surface temperature (SST) and anomaly (SSTA); sea level pressure (SLP); precipitation; and horizontal or vertical wind patterns (U-wind or V-wind, respectively), amongst others (Stenseth, 2003). Widely-used indices include El Niño Southern Oscillation (ENSO) indices such as Niño 1, 2, 3, and 3.4; the North Atlantic Oscillation (NAO), the Pacific Decadal Oscillation (PDO), and many others (Trenberth and Hurrel, 1994, Hurrell, 1995; NOAA, 2015). The majority of these indices rely heavily on empirical orthogonal analysis of SST, with some correlation to the other climate indices already mentioned. SSTA in particular is often indicative of larger scale climate dynamics due to the direct impacts of changes of ocean-atmosphere boundary temperature differences on their heat and moisture exchange (Talley, 2011), as small deviations in this exchange can have widespread consequences for atmospheric circulation patterns (Ahrens, 2010).

Previous studies working with dipole identification and analysis have differed in the indices, time windows, and spatial windows used, as well as their analysis methods and filtering techniques. One of the first uses of the term dipole in climate studies proposed a meridional dipole between the northern and southern hemispheres using EOF analysis of 27 years of Atlantic basin SST data (Servain, 1991). Deser and Blackmon (1993) used the same method to show a dipole-like oscillation in SLP over the North Atlantic using 100 years of SST, SLP and surface air-temperature data. Venegas et al. (1994) coupled 40 years of SST and SLP data and implemented singular value decomposition (SVD) analysis to identify a South Atlantic dipole.

More recent studies frequently use modeled data to supplement observational data, or in place of observational data completely, leading to large, un-quantified uncertainties (Smith, 2008).

The Indian Ocean dipole (IOD) is one of the most widely studied of all currently identified dipoles. Its seasonal variations were first identified by Saji et al. (1999) via EOF analysis of a rectangular section of the Indian Ocean basin. Numerous further studies have sought to refine the dynamics and over-land impacts of this SSTA oscillation, using both EOF and SVD analysis (Behera et al., 2000; Behera and Yamagata, 2001; Moroika et al., 2012), all of which pointed to a distinct relationship between the dipole and monsoon patterns.

However, the accuracy of using EOF and SVD analysis to identify dipoles in general has been called into question due to the dependence of these methods on the spatial window chosen (Dommenget, 2002). As such, recent publications on dipole behavior have made use of alternate, spatially stable methods, such as cross correlation coefficient analysis (CCA). This method has been shown to identify dipoles both in the Antarctic region (Yuan and Martinson, 2000) and Asia (Xue, 2003). While this provides a spatially stable result, CCA must still be used thoughtfully. Like EOF and SVD methodologies, it is sensitive to the chosen time window and method of filtering, identifying only those patterns that are stable for the duration of the time analyzed.

In this study, we identify dipoles through correlation coefficient analysis of two global SSTA datasets composed of a synthesis of observational, satellite and model data. This is followed by a multi-proxy analysis of the larger system associated with two of the 16 significant SSTA dipoles and supported by EOF results following identification of the relevant special

windows. The SSTA datasets both span ~100 years of SSTA data, though higher latitudes and the Pacific rely more heavily on model estimations to supplement observational records. The dipoles themselves are specifically defined as pairs of 2° by 2° latitude/longitude squares of 11-month, running mean averages of SSTA, which have a continuous 180° phase shift relationship. This inverse, phase-locked coupling is characteristic of synchronized oscillators observed in many complex physical systems (Pikovsky, 2001), which motivates further investigation of the connections between the dipoles and allows for the use of some linear methods of analysis to better define the relationship between the poles. In addition, comparison of the dipole signals to precipitation shows a strong correlation to anomalous overland rainfall patterns, specifically in the region of the South American Monsoon and over northwest Australia.

Data and Methods: This study employed two different SST datasets composed of a synthesis of observational, satellite, and model data. We use the extended reconstructed SST V3b from Smith et al. (2008), which is a 2° by 2° latitude-longitude monthly average grid from January of 1854 to 2007 (NOAA_ERSST_V3 data is provided by the NOAA/OAR/ESRL PSD, Boulder, Colorado) and GISTEMP data from their website at http://www.esrl.noaa.gov/psd/ which is available in a 2° by 2° latitude-longitude monthly average from January 1880 to 2009. These datasets have been broadly employed for previous SST-related studies (Muñoz et al. 2010; Nnamchi et al. 2011; Kayano et al., 2013). Monthly, gridded, mean sea level pressure (SLP) and horizontal (U) zonal wind data sets are also used in order to assess how the dipole modes communicate via atmospheric energy transfer. These datasets were drawn from the 20th Century Reanalysis Data (Compo et al., 2011) provided by NOAA, which is available in a 2° by 2° grid of monthly averages from January 1871 to December of 2011 and use compositions of satellite

and historical data, accounting for negative climate trends noted in previous studies (Smith, 2003). Some bias is noted from cloud cover at high latitudes, though this is specifically noted as most prevalent in the northern latitudes (Compo et al. 2011).

To supplement our understanding of the implications of these dipole proxies beyond the ocean, we analyzed regional precipitation data. This data is provided by the Global Precipitation Climatology Centre (GPCC, 1901-2010) and the University of Delaware (UDel_AirT_Precip, 1901-present, as found on their website at http://www.esrl.noaa.gov/psd/). This work does not seek to identify new dipoles in the precipitation data, but rather to quantify the correlations between the two dipoles' dipole mode index (DMI) (calculated following the procedures published by Saji et al. (1999), Yu et al. (2000), Beherea and Yamagata (2001), Muñoz et al. (2012), and Nnamchi et al. (2011)) and each point within the precipitation data. This allows for a simple demonstration of the potential wider impacts of these teleconnections.

For all variables (SST, SLP and U-Wind), we computed monthly anomalies as the difference between the monthly average for each year and the climatological value for the month. The anomaly time series are then standardized by dividing the monthly time series by the corresponding monthly standard deviation for each grid point. The strong, high frequency components of the monthly time series are removed by calculating 11 month running means (5 months before and after the considered month), negating seasonal influences. A high-pass filter is also applied to remove trends longer than 8 years, as resolution of these trends are questionable based on the duration of reliable observational data. Given the location of this study, we define reliable as the duration of satellite observations (1979-present). This shorter

window is analyzed to ensure that the observed dipoles are not the result of model influence in either data set. Overall, we focused on oscillations with periods of 2 to 7 years, which is commensurate with the period of the strongest, previously defined, SST oscillations, such as the El-Niño Southern Oscillation.

Each global set of SSTA time series is then phased shifted by 180° and subjected to point by point cross correlation coefficient analysis with each individual un-shifted point, in search of statistically significantly (as determined by Monte Carlo simulations), inversely correlated, grid points, excluding continuous fields of correlation surrounding individual points. Sixteen dipoles with a correlation coefficient of above 0.6 were identified using this method. For further analysis of the teleconnection characteristics of these dipole modes, we defined the dipole mode index (DMI) of each pair (See Fig S14). We apply principal component analysis on 9 SSTA time series (one central, eight surrounding) per dipole end. The difference of the first principal components of the two ends is then calculated and the resulting time series is labeled the DMI for the dipole. This simple DMI time series allows for cross-dipole comparisons, as well as comparisons to atmospheric variables and pre-existing climate indices by condensing the information from the entire dipole into a single time series.

Having identified and condensed sixteen significant dipoles, we chose two for in depth study, prioritized for their potential temporal extension and significant correlation with precipitation anomalies. This further analysis includes EOF analysis of the SSTA of their respective ocean basins, as well as cross correlation and EOF analysis of the other proxies listed above with respect to their DMI's. Similar analysis has been performed for all dipoles and may

be found in Appendix II, along with short descriptions of the other dipoles in relation to pre-existing climate indices.

Results: The two dipoles chosen for further study range over the South Pacific (hereafter the South Pacific Dipole Oscillation, or SPDO) and the South Indian Ocean (hereafter the South Indian Dipole Oscillation, or SIDO) (Figures 1; S1 for EOF). While we are able to identify their continued stability for the duration of the record and consistent phase relationships using CCA, spatially constrained EOF analysis shows that the first EOF mode of the oscillation explains 30% of the total SSTA variance for SPDO and 20% for SIDO. Both show a northwest to southeast oscillating pattern, and are present in both reanalysis datasets in CCA, EOF, post-satellite, and seasonal data analysis (See Figures S1-5). However, the physical characteristics of these dipoles and their behaviors differ not only from each other, but also from other teleconnections identified in previous publications, despite some shared areas of influence.
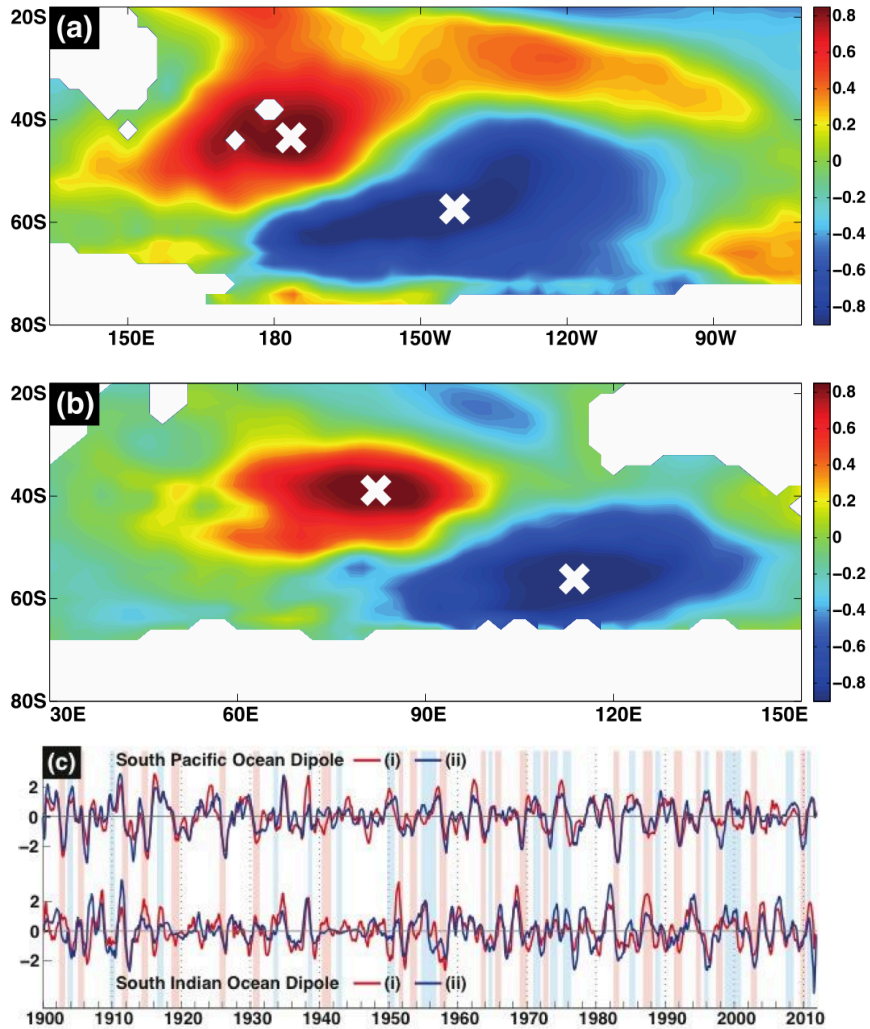
Figure 3.1. Correlation coefficients between the DMI and SSTA (ERSST). White crosses mark points of maximum negative correlation coefficients, and are referred to as dipole centers, after analysis of the global data series. This figure shows the defined dipole mode indices explain the majority of SSTA around the dipole centers. In order to ensure that this is not an artifact or chance occurrence in the dataset, we also employed a different dataset, GISST, shown in Figure S2 and only post-satellite readings, Figure S3 (c) SSTA time series that are most negatively correlated over the South Pacific Ocean (top) and South Indian Ocean (bottom). The time series are chosen in each box in (a) and (b). Time series picked in the boxes (ii) (blue lines) are multiplied by -1 for visual comparison. The maximum negative correlation coefficients between two time series from each box (marked in (a) and (b)) are -0.82

and -0.68 for SPDO and SIDO respectively. Red and blue shades represent the times of El Niño and La Niña events respectively.

SPDO is defined by two centers of oscillation over the southern Pacific Ocean, ranging from off the southeast coast of New Zealand to approximately the edge of the polar front, 20° further east (Figure 1). It remains strongly present in each stacked month for the duration of the record when studied via EOF analysis (see Figure S4). SPDO is also characterized by its consistent correlation of a positive SLP anomaly directly between the poles when there is a positive DMI (i.e. a positive thermal anomaly over the NW pole, negative over the SE), and a negative SLP anomaly over the southeastern region of the dipole when the DMI is negative (See Figures S6-7). This also correlates to the occurrence of a westerly zonal wind along the boundary of the SLP anomalies (See Figure S6). However, the relationship between ocean and atmosphere behaviors is relatively weaker in the Austral winter, most likely do to the weakening of the thermal energy of the system.

All of these characteristics clearly define prominent internal characteristics, but, given its location in the Pacific, it is worth noting that SPDO does not have a significant correlation with Niño 3.4. SPDO's DMI shows a correlation coefficient of -0.47, which is below the level of dipole significance (0.6 for this data set), but still the strongest correlation coefficient between the DMI and a previously defined climate index. A tested AR1 model further supports the independence of the internal oscillation of the system from the present influence of the El Niño oscillation, following the example of Shakun and Shaman (2009) (see Supplemental for details).

A full discussion of comparisons between SPDO and previously published climate indices can be found in the supplemental material.

The same set of correlation coefficients and interactions is defined for SIDO, although there are significant differences in the seasonal and inter-proxy behaviors of this dipole from those of SPDO. SIDO is defined as spanning the region from within the southern Indian Ocean (~40°S and 85°N) to below Australia (~60°S and 115°E) (See Figure 1). It also shows seasonal variation, but unlike SPDO, SIDO's own internal, SSTA oscillation drops below the significance level in the stacked December record. However, it is present all other months, with slight variation in placement and shape. Positive DMI (warming over the NW, cooling over the SE) correlates to a high SLP anomaly between the two centers of the dipole, with a negative anomaly formed near Antarctica (see Figure S8). The positive pressure system correlates with westerly wind anomalies along 60°S over the SE pole of SIDO and easterly wind anomalies over the NW pole (see Figure S8). SIDO's DMI also shows a seasonally dependent level of correlation to these atmospheric measurements, though, with relative weakening in August-October. The relationship does not dip below the level of significance (See Figure S9).

The combined locations of SIDO and SPDO necessitate comparison to the Antarctic Circumpolar Wave, as it is described in Haarsma et al. (2000) as a resonate wave of pressure zones around the continent. However, a correlation coefficient test of both DMI's and the index associated with the wave shows no significant correlation (see Figure S10).

As mentioned earlier, other oscillating climate indices with similar periodicities were considered and analyzed in relation the these DMI's, including the Pacific Decadal Oscillation, the North Atlantic Oscillation, and the Southern Oscillation Index. None of these were found to have a significant correlation coefficient, even when tested for a time lag. The Southern Oscillation Index had the highest level of correlation with both oscillators: 0.44 with SPDO at a four month time lag and -0.48 with SIDO at a six month lag.
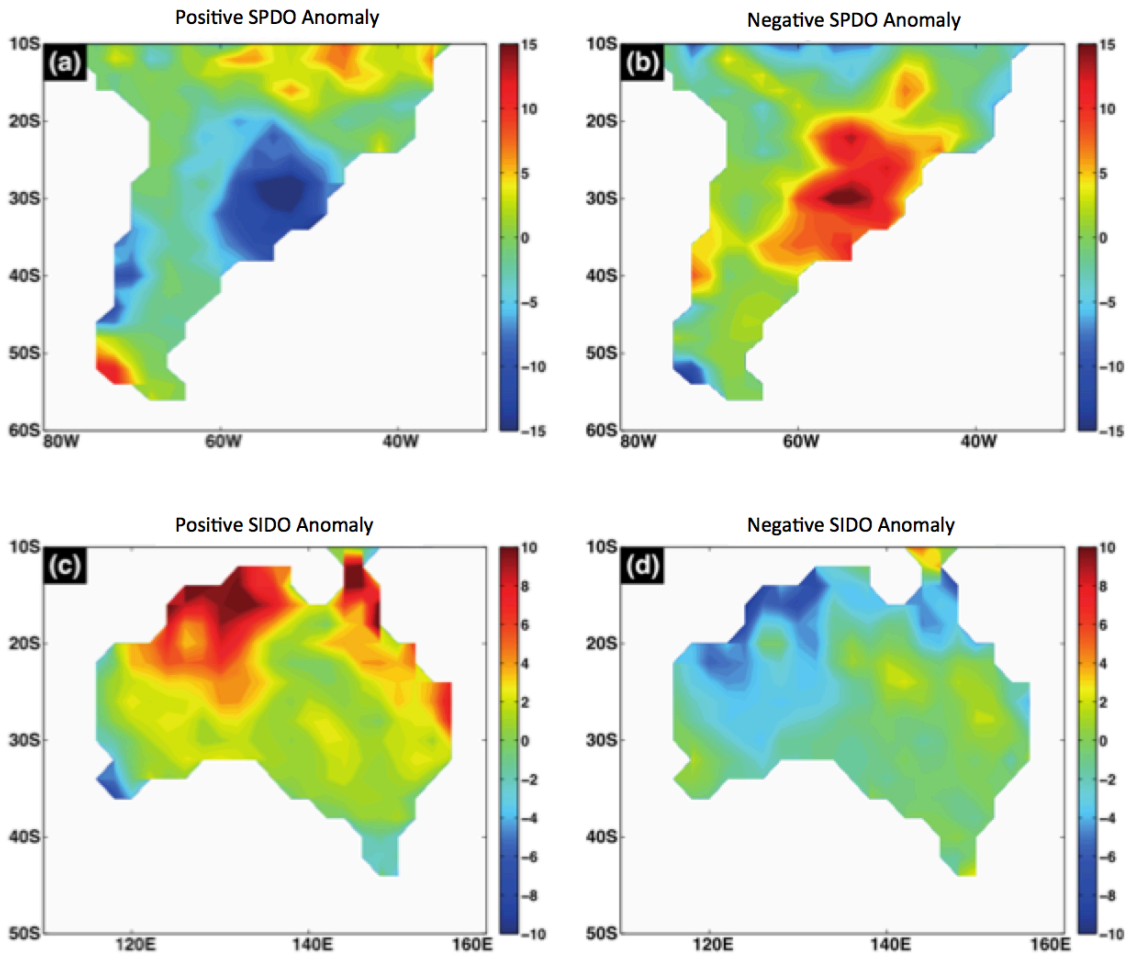
Figure 3.2. Precipitation (GPCC) composition (in cm) during the positive and negative dipole events. The events are selected when DMI values are greater than 2 or less than -2. Standard deviation of precipitation anomaly is 4.75cm over South America, 7.76cm over Australia. Figure S11 shows the same analysis as Figure 2, but uses the University of Delaware precipitation data.

These dipoles are made more important in the context of their impacts in teleconnected regions. Here we used the GPCC and UDel precipitation data sets in order to look at the correlations between the DMI and precipitation over land. While this analysis does not prove causation, it is

worth noting that both dipoles have extremely strong correlations to regional anomalies, with anomalous precipitation patterns in years of strong dipole activity.

An ~15cm precipitation anomaly over a large region of southeastern South America correlates with periods of strong SPDO DMI. During SPDO's positive DMI peaks, there is anomalously low precipitation recorded, and vice versa (Figures 2a and 2b, Figure S11a and S11b). The standard deviation of this region over the entire record is 4.75cm in the GPCC data set (4.81cm in the UDel), making this anomaly strongly statistically significant. This region's rainfall has been previously studied in relation to two major atmospheric anomalies, as well as the ENSO pattern. The South Atlantic Convergence Zone (SACZ), a pressure and wind system with seasonal and sub-monthly (8-day periodicity) modes of variability, has been associated with strengthened and weakened South American Monsoons [Barros et al. 2002, Marengo et al. 2010]. The Pacific-South American Patterns (PSA) have also been associated with blocking or enhancing the SACZ's influence on the monsoonal patterns (Mo and Paegle, 2001; Irving and Simmonds, 2016). Both the SACZ and the PSA are studied on time scales significantly different from ours, but may suggest how a SSTA teleconnection may be connected to precipitation, perhaps via some modulation of PSA2, a sub system of PSA with a monthly to seasonal variability and a direct connection to ENSO.

Northwestern Australia recorded an ~10cm precipitation anomaly in years of strong SIDO DMI. Years of positive DMI are again associated with a negative precipitation anomaly. The standard deviation of the region for the length of the record is 7.45cm (7.81 in UDel) (Figure 2c and 2d, Figure S11c and S11d). This region of Australia is less studied than the southwestern

quadrant of Australia, which has the most notable rainfall anomalies. These anomalies have been associated with numerous nearby pressure teleconnections, which are seasonally associated with SSTA gradient changes in the Indian Ocean (Murphy et al., 2007, Ummenholfer et al., 2009). However, due to a noted increase in rainfall over the northwestern region accompanying the overall drought of the western regions, studies of the connection of precipitation to external forcing via SST, pressure, and winds have been published (Wang et al., 2009; Shi et al., 2008). These studies focus on precipitation time series first, and demonstrate a connection to La Niña patterns, eastern, equatorial, Indian Ocean monsoonal influences, as well as atmospheric aerosol content on seasonal and decadal scales (Shi et al., 2008, Rotstayn et al. 2007). While several publications mention the seasonal importance of the Indian Ocean SSTA gradients, these mostly focus on a monthly to seasonal temporal scale, and do not delve into connections near Antarctica.

Again, these correlations do not imply a causal relationship in either case. Still, the strong correlations of these DMI's with anomalous rainfall covering the regions of the South American Monsoon and an area of significant rainfall in Australia mean that further understanding the influences and patterns of the DMI's have the potential to help predict significant drought and flooding, as well as better refine precipitation models in these areas.

Discussion and Conclusions: In this study, we demonstrated the distinct, internal oscillations of a pair of previously unidentified dipoles and quantified their correlated relationships with wind, pressure and precipitation data sets. The two dipoles discussed here are only one pair of 16 total dipoles identified by the combined methods demonstrated above. These dipoles are found in all

ocean basins, with distinct structures of interactions, sharing only the characteristic, persistent 180° phase shift relationship in SSTA. Given that recent papers have suggested that previously identified teleconnections are responsible for the cooling of the equatorial Pacific and possibly the observed "pause" in global warming (Kosaka, 2013; Held 2013; Steinman, 2015), further study of these new dipole teleconnections is vital for our understanding of global climate dynamics. Indeed, continued study of the precipitation correlations identified here is likely to improve both long and short term forecasts and planning for those living in these areas of synchronous, anomalous rainfall.

In future research, we will seek to quantify and explain the physical mechanisms responsible for these patterns, as well as to extend our analysis to paleoclimate data sets, such as high-resolution lake sediment cores, ice cores, and coral proxies. These will be used to analyze dipole stability and potential impacts on these patterns from anthropogenic sources. A preliminary analysis of the potential energy transfer functions of the two dipoles in this paper has already been completed, but the results show numerous non-unique spectral peaks (see Figure S13). Together, these will lead to a better understanding of over-land effects of as many dipoles as possible, the stability of these dipoles over time, and any changes in their behavior that may be associated with human or natural systems. Any generalized set of conditions that allow for these sustained, synchronized oscillations to develop on a sub-decadal scale will help refine more accurate climate models, as well as precipitation forecasts.
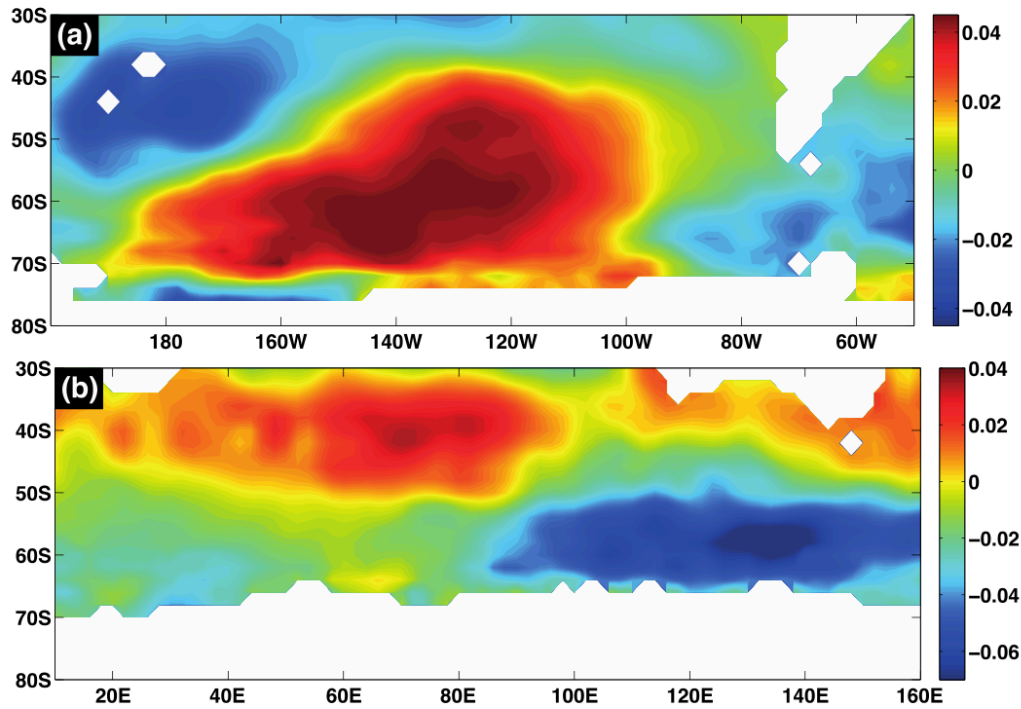
Figure S3.1. Identification of 1st EOF of the dipole regions. (a) EOF analysis on the SSTA (11 months running mean, 112 years monthly data) over South Pacific and (b) over South Indian Ocean. EOF is applied to the SSTA over the corresponding region and the figures represent the first EOF mode of each ocean basin. The time series are chosen in each box in (a) and (b). The maximum negative correlation coefficients between two time series from each box (marked in (a) and (b)) are -0.82 and -0.68 for SPDO and SIDO respectively.
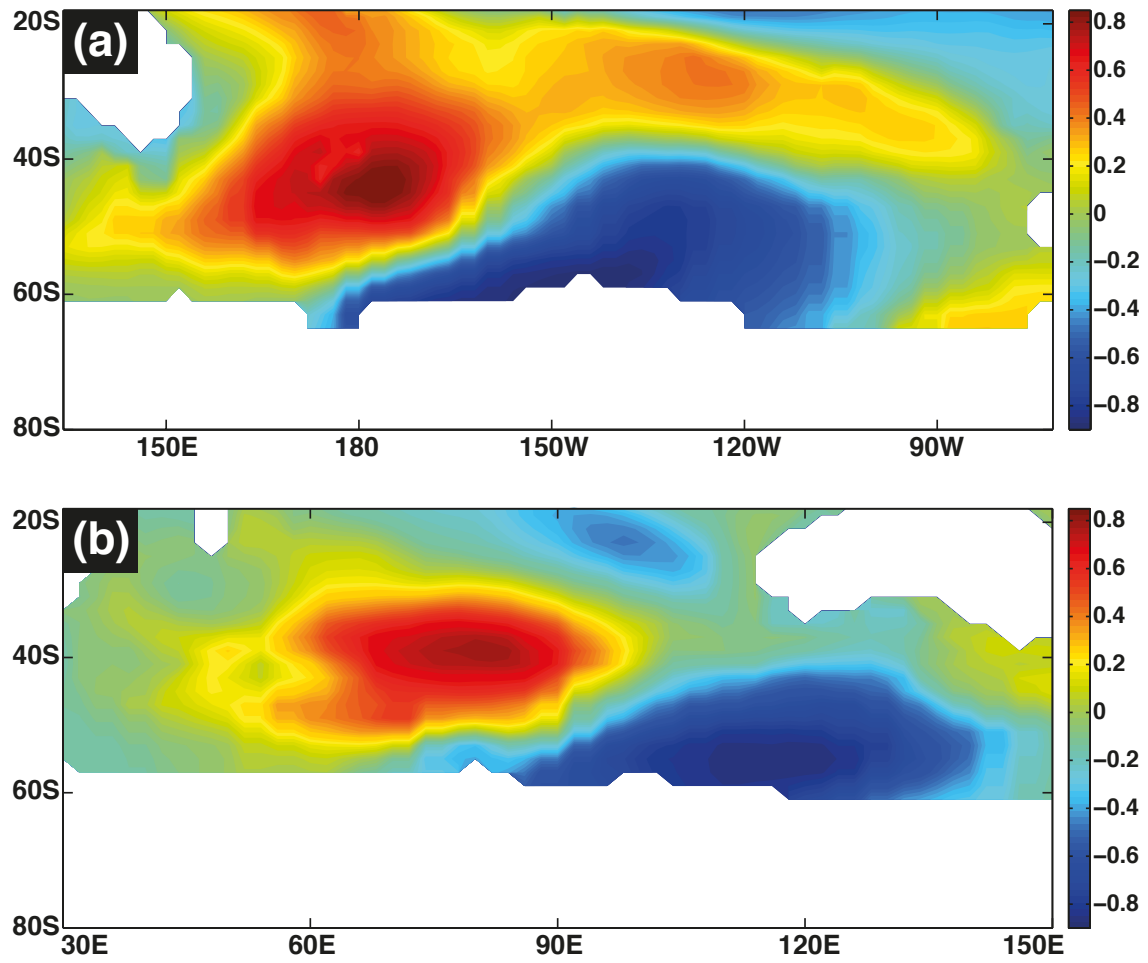
Figure S3.2. Correlation coefficients between the DMI and SSTA (GISST). (a) SPDO and (b) SIDO.
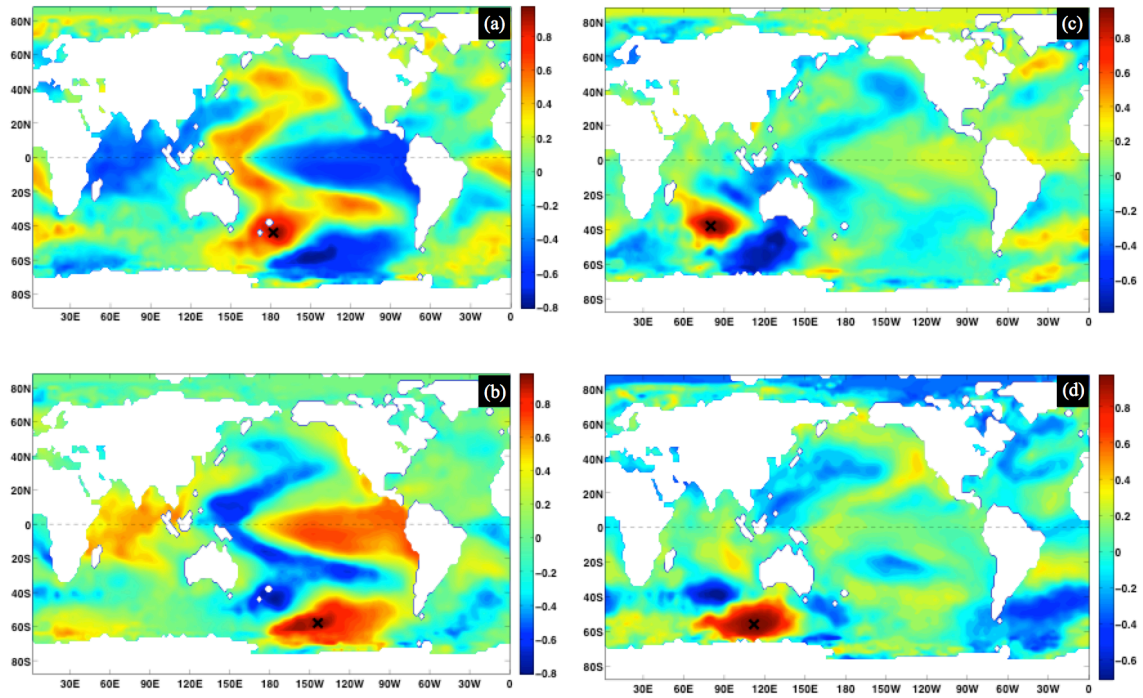
Figure S3.3: Correlation coefficient analysis results between DMI and SST for SPDO in (a) and (b);

SIDO in (c) and (d) for satellite era data only (specifically from 1979 to 2011).
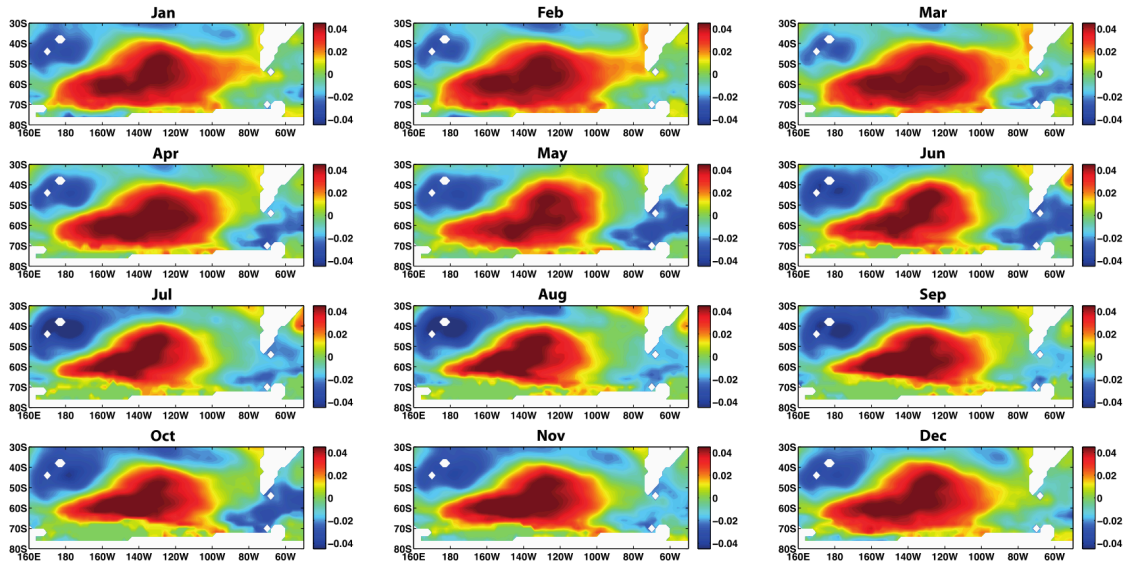
Figure S3.4. EOF analysis of SSTA (ERSST) over the South Pacific Ocean for each month, demonstrating the monthly variability and persistence of SPDO.
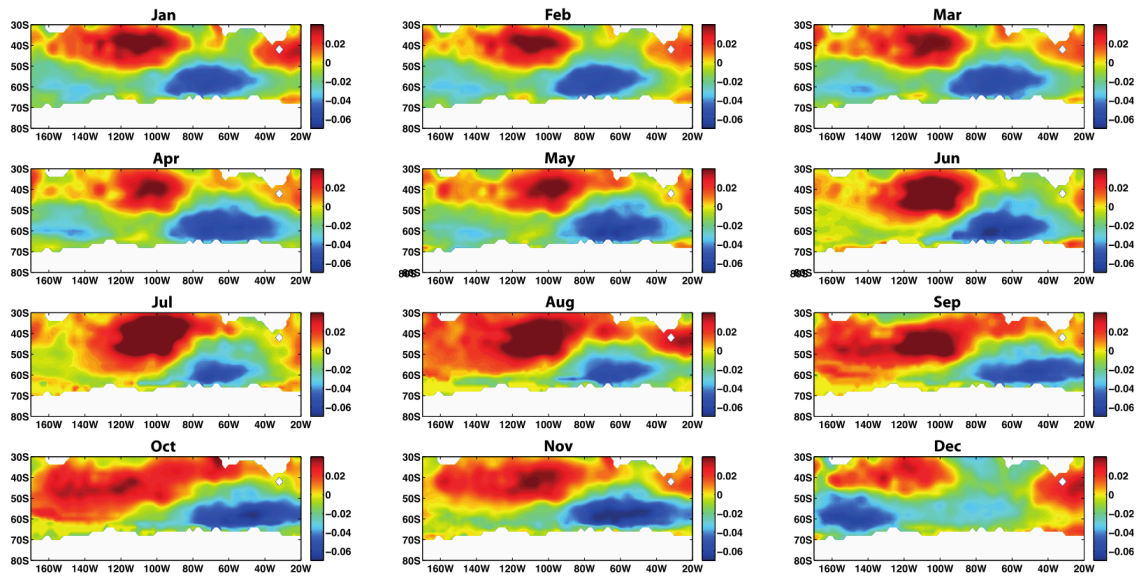
Figure S3.5. EOF analysis over the South Indian Ocean for each monthly average, demonstrating the monthly variability and persistence of SIDO, as well as its near disappearance in December.
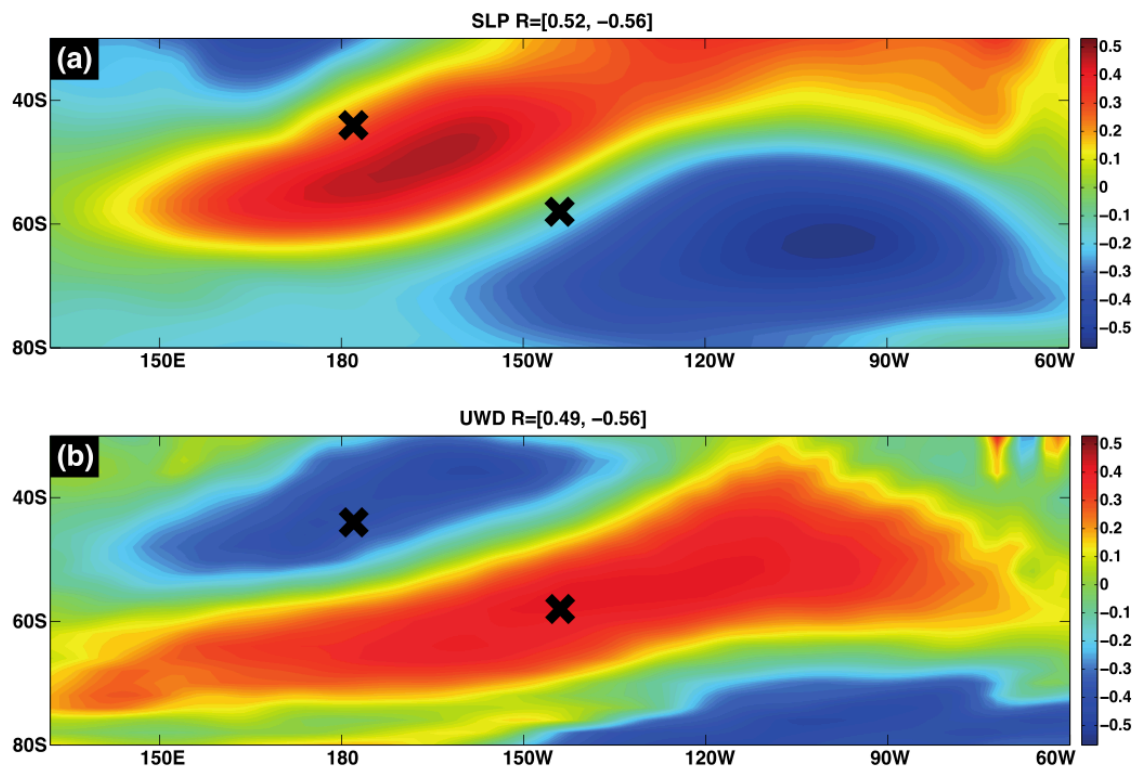
Figure S3.6. (a) Correlation coefficients between SPDO's DMI and SLPA in interannual time scale. Black crosses are marked to show the dipole centers. The values in parenthesis in the titles are the maximum correlation coefficients between DMI and SLPA within the presented spatial domain. (b) Same as (a) but showing correlation coefficients between SPDO's DMI and U-Wind.
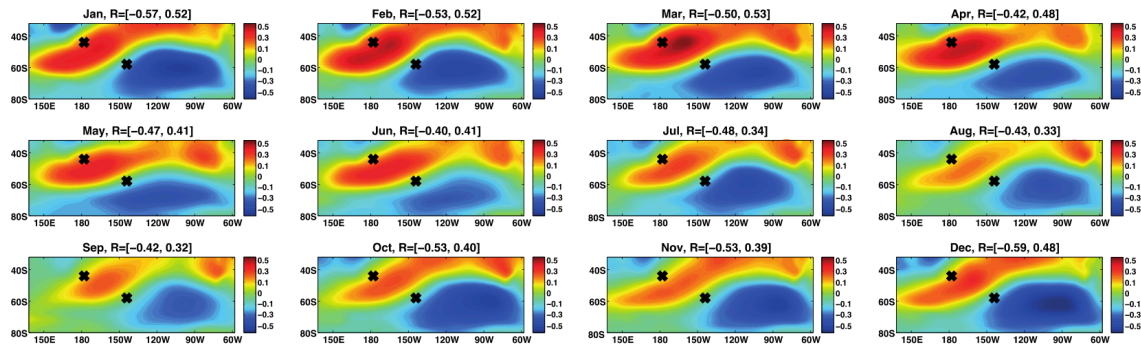
Figure S3.7. Correlation coefficients between SPDO's DMI and SLPA in each month over the South Pacific Ocean. Each figure shows one month and the values in parenthesis in the titles are the maximum correlation coefficients between DMI and SLPA within the presented spatial domain.
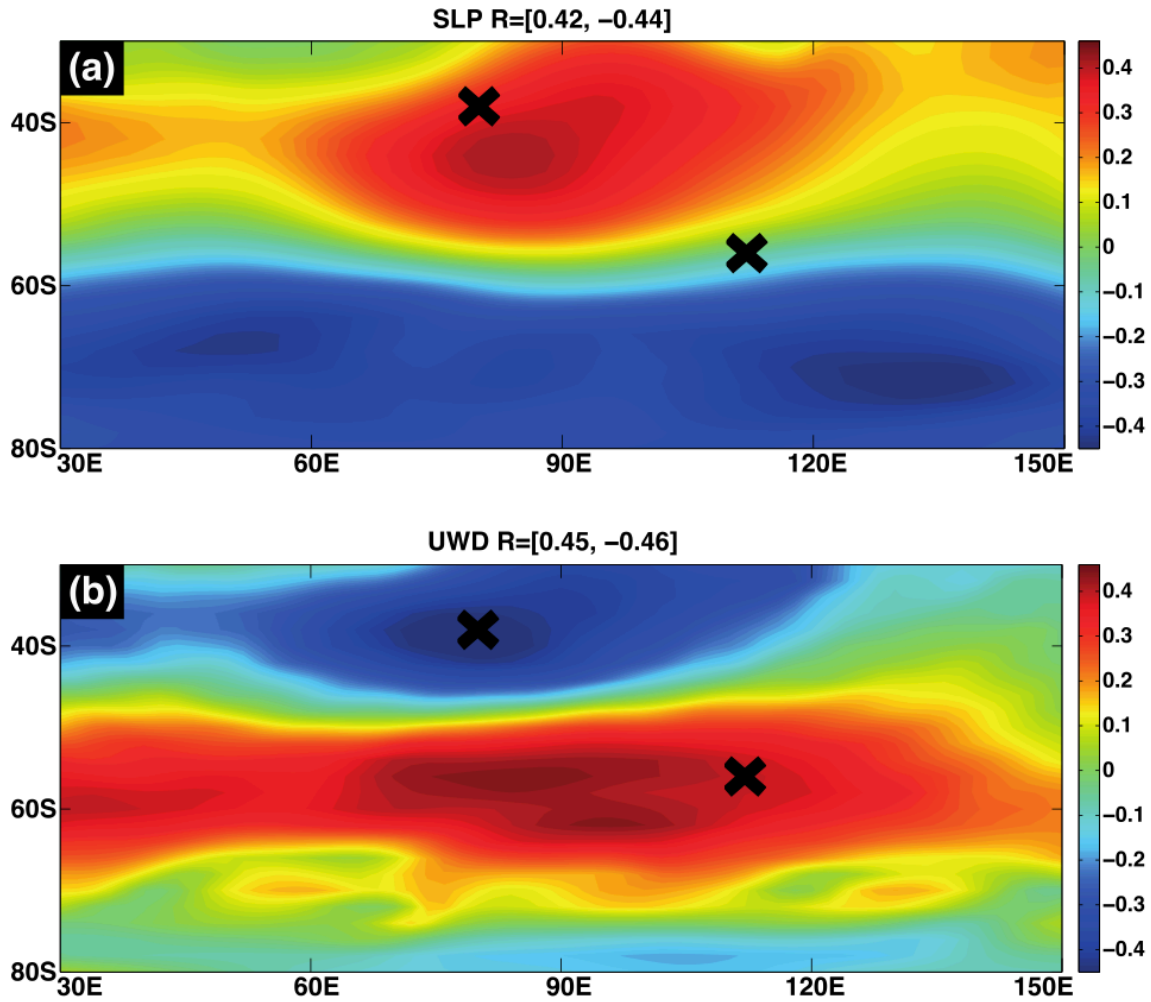
Figure S3.8. (a) Correlation coefficients between SIDO's DMI and SLPA in the interannual time scale. Black crosses are marked to show the dipole centers. The values in parenthesis are the maximum correlation coefficients between the DMI and SLPA within the present spatial domain. (b) Same as (a) but using correlation coefficients between SIDO's DMI and U-Wind.
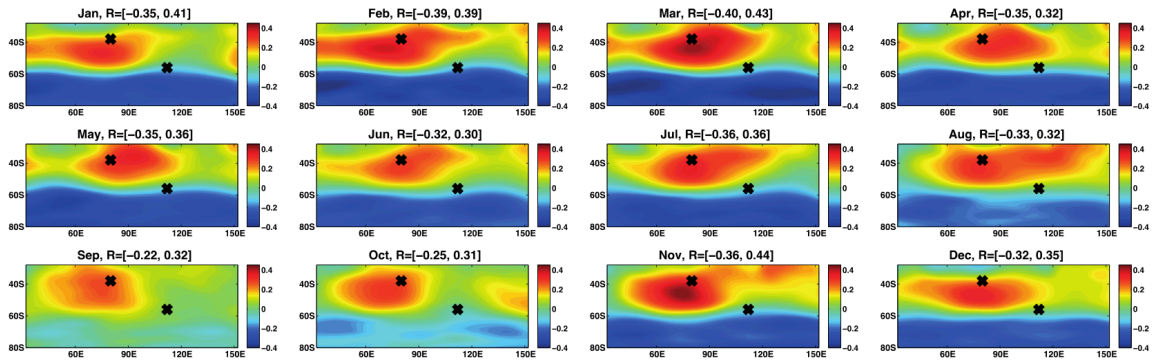
Figure S3.9. Correlation coefficients between SIDO and SLPA in each month over the South Indian Ocean. Each figure shows one month and the values in parenthesis in the titles are the maximum correlation coefficients between DMI and SLPA within the presented spatial domain.
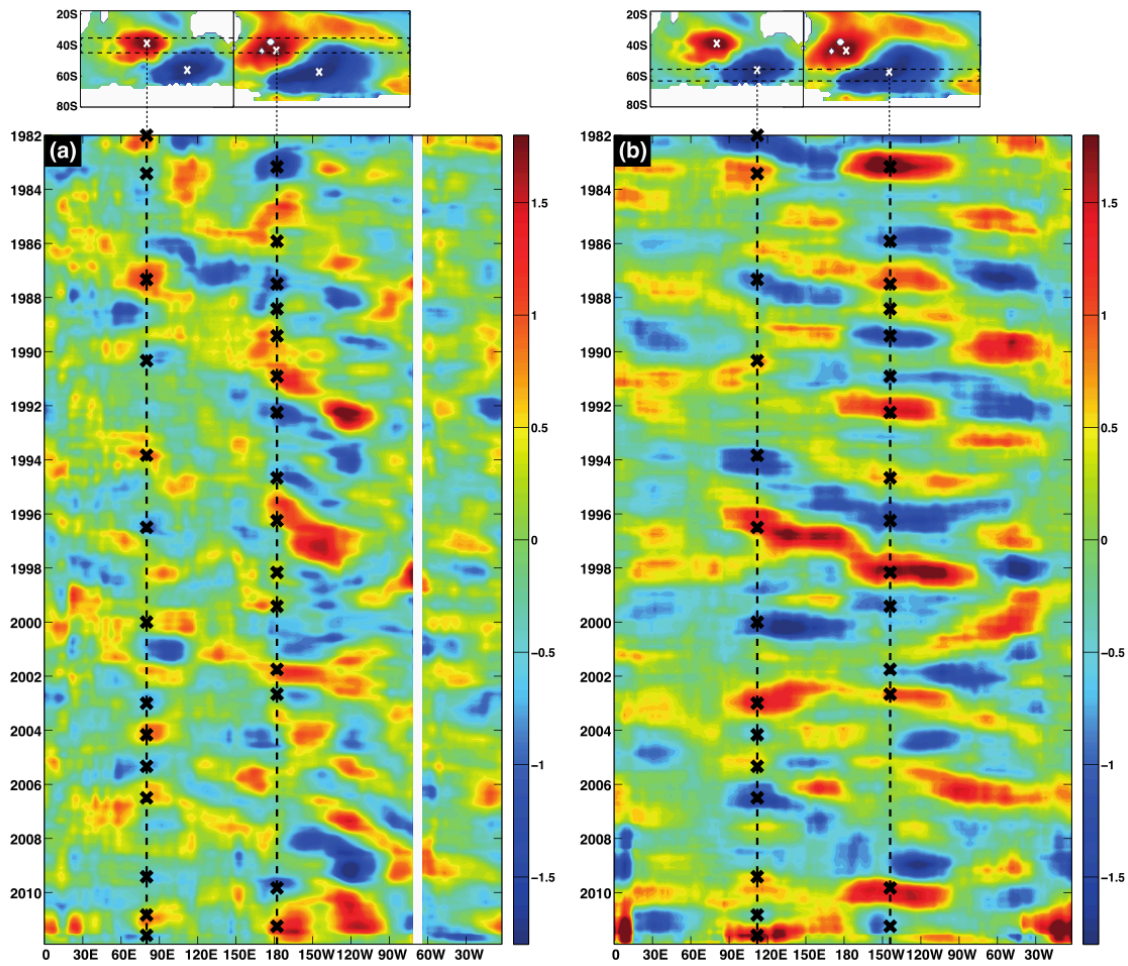
Figure S3.10. SSTA for the most recent 30 years: averaged SSTA over (a) 38-42°S (latitude band of the north-side pole locations), (b) 58-62°S (latitude band of south-side pole locations). Dotted line shows the longitude of the locations of the poles. Cross marks show the times of strong dipole occurrences.
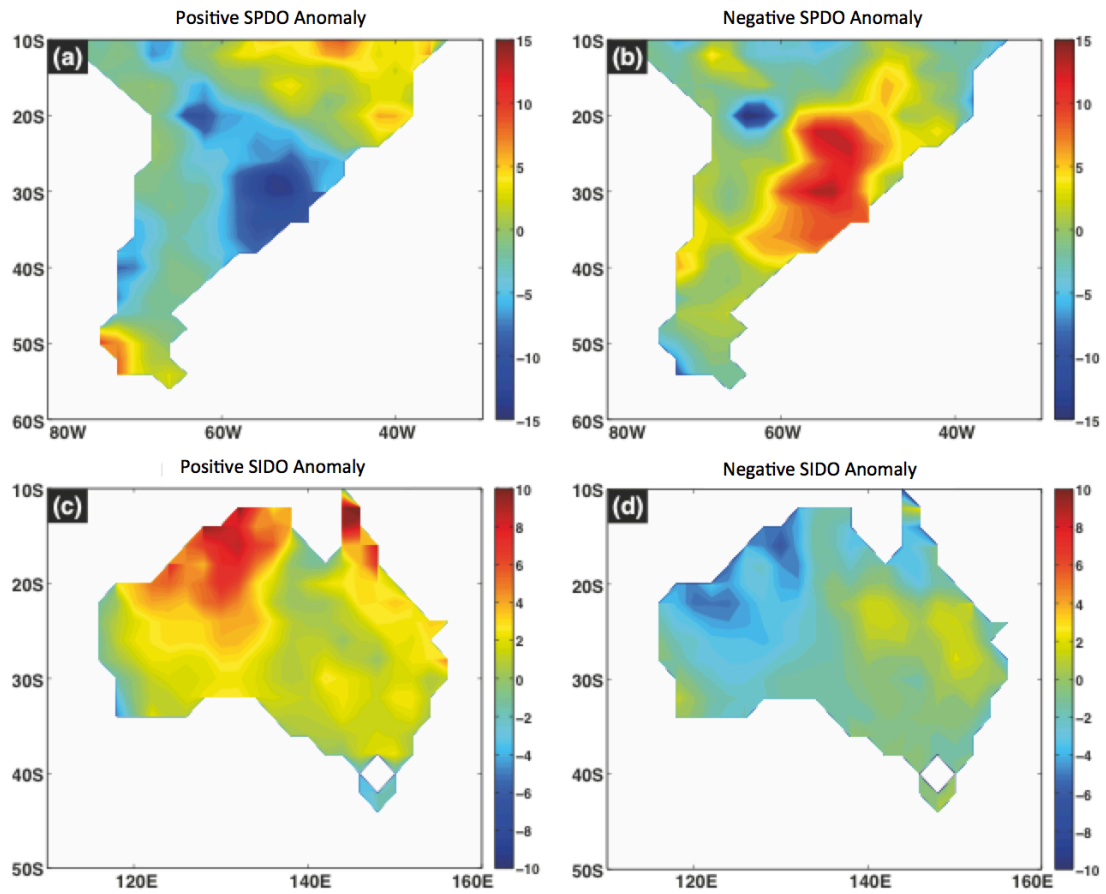
Figure S3.11. Precipitation (University of Delaware) composition (in cm) during the positive and negative dipole events. The events are selected when DMI values are greater than 2 or less than -2. Standard deviation of precipitation anomaly is 4.81cm over South America, 7.45cm over Australia.
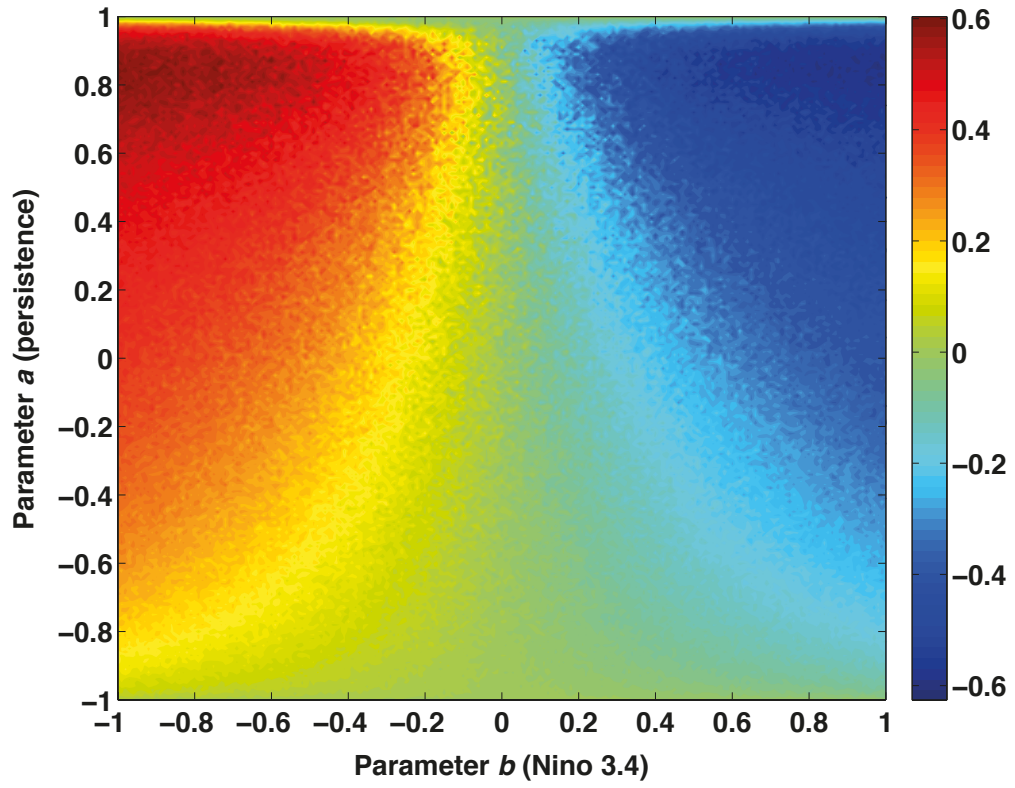
Figure S3.12. Correlation between DISP DMI and generated DISP DMI from AR1 model.
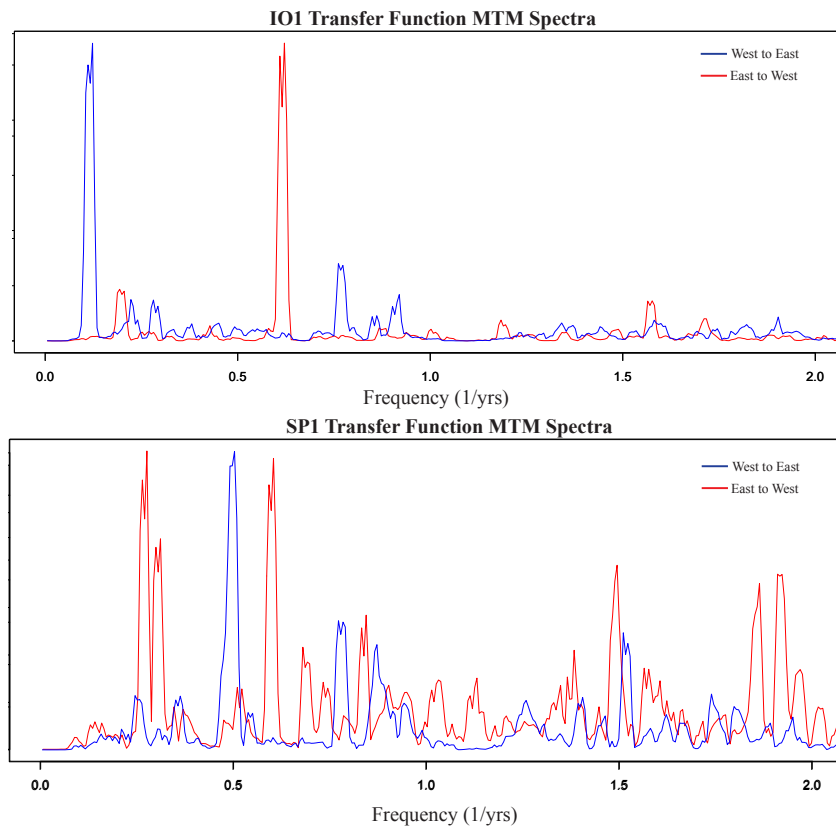
Figure S3.13: Spectra of transfer functions for the SIDO and SPDO (top and bottom, respectively), found via deconvolution of the filtered time series shown in Fig. 1. While the SIDO transfer functions show strong, singular peaks, the SPDO do not, and neither set show spectra with periodicities that can be directly linked to specific atmospheric or oceanic frequencies in their vicinity.
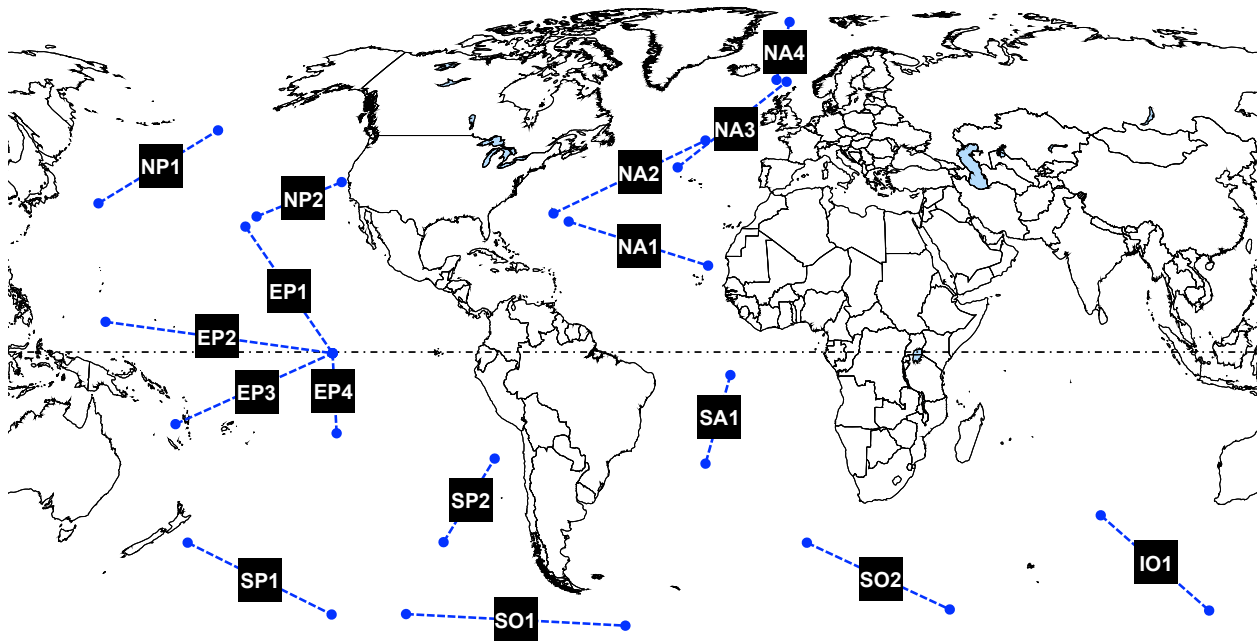
Figure S3.14: Locations of the sixteen dipole modes found in this study. Each dipole consists of two centers of maximum negative correlation, each of which is marked with a dot.
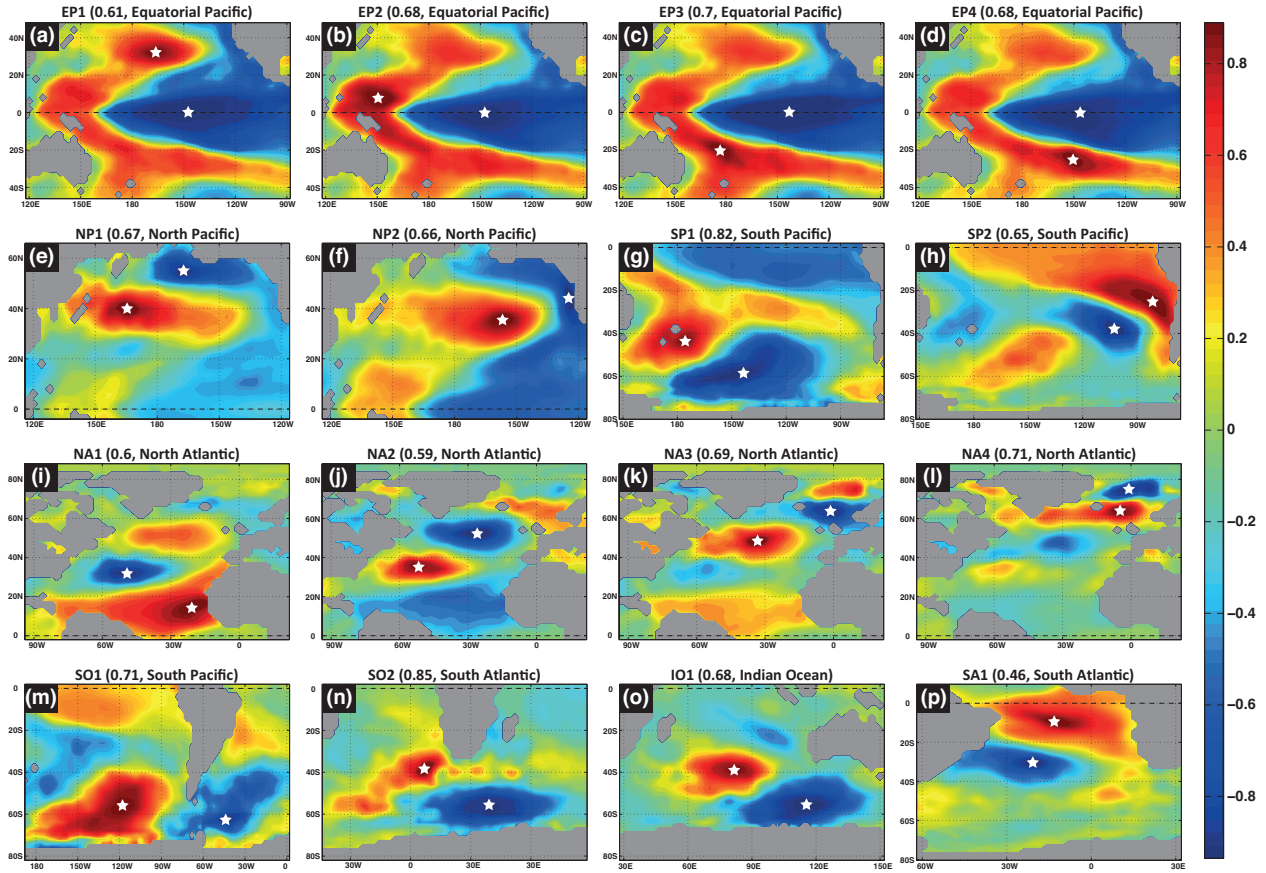
Figure S3.15: An exhaustive search of the correlation coefficients of sea surface temperature anomaly (SSTA) time series over the ~100 years of known SST history on a 2° x 2° grid resulted in the detection of sixteen, synchronized, oscillating dipole systems with a π radians phase shift (dipoles with correlation ~ -1), over this time period in the geographic regions shown. Each center of an anti-correlated dipole pair is marked with a white star. The correlation coefficient between the time series in the marked centers is given for each map (multiplied by -1). For each identified dipole, a dipole mode index (DMI) is calculated from the first principal components (PC-1) of a small surrounding neighborhood, consisting of nine time series. The correlation coefficient between the DMIs and the SSTA time series in the entire grid are then computed and displayed in the maps (scale on right of figure). We can see the center locations, strength, and area of each dipole from this figure.
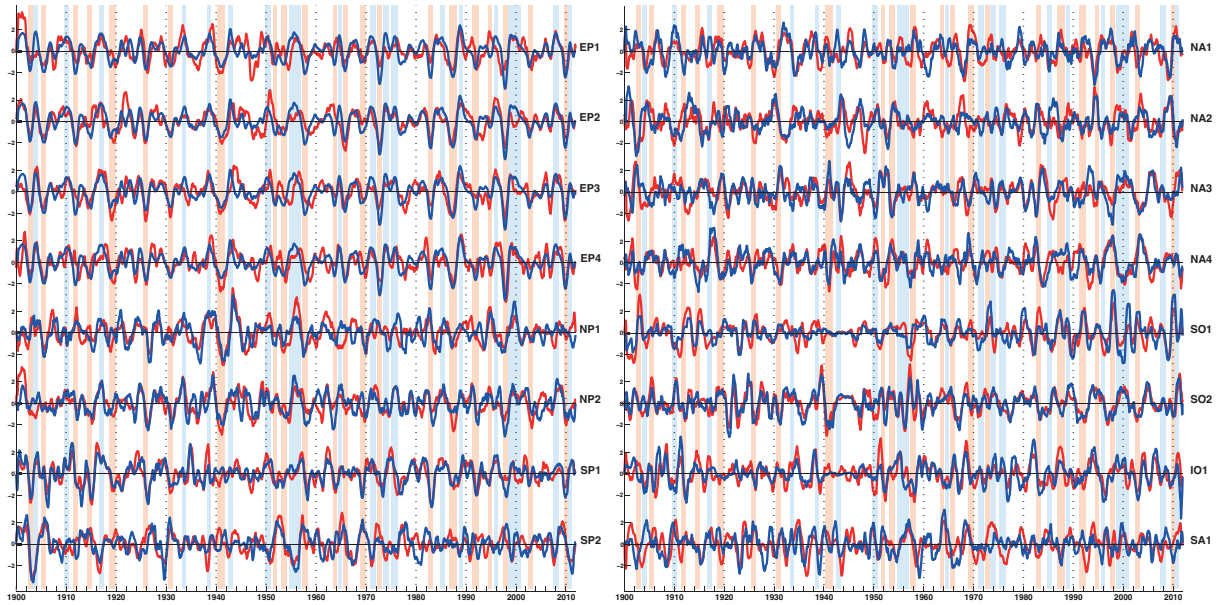
Figure S3.16: SSTA time series of the dipole centers that were marked with white stars in figure 2. The blue lines represent the SSTA time series of the dipole centers within the blue colored areas from Figure 2 for each dipole, and the red lines denoting those in the red areas. The blue lines are multiplied by -1 for the comparison of the time series of the dipoles. Blue and red shades represent the years of El Nino and La Nina respectively (Since the time series over the Nino 3.4 region are inversed, the EP1-EP4 have negative anomalies when El Nino occurs).

REFERENCES

Ahrens, C. D., 2010: *Essentials of Meteorology: An Invitation to the Atmosphere*, 6th ed. Cengage Learning, 528 pp.

Barros, V., Doyle, M., González, M., Camilloni, I., Bejarán, R., & Caffera, R. M. (2002). Climate variability over subtropical South America and the South American monsoon: a review. *Meteorologica*, *27*(1-2), 33-57. DOI: 10.5194/cp-12-1681-2016

Behera, S. K., P.S. Salvekar, and T. Yamagata, 2000: Simulation of interannual SST variability in the tropical Indian Ocean, J. Climate, **13**, 3487-3499. DOI: 10.1175/1520-0442(2000)013

Behera, S. K, and T. Yamagata, 2001: Subtropical SST dipole events in the southern Indian Ocean. Geophys. Res. Lett., **28**, 327–330. DOI: 10.1029/2000GL011451

Compo, G. P., and Coauthors, 2011: The Twentieth Century Reanalysis Project. Quarterly J. Roy. Meteorol. Soc., **137**, 1-28. DOI: 10.1002/qj.776

Connolley, W.M., 2002: Long-term variation of the Antarctic Circumpolar Wave. J. Geophys. Research: Oceans (1978-2012), **107** (C4), SOV 3-(1-12). DOI: 10.1029/2000JC000380

Deser, C. and M. L. Blackmon, 1993: Surface climate variations over the North Atlantic ocean during winter: 1900–1989. J. Climate, **6**, 1743–1753. DOI: 10.1175/1520-0442(1993)

Dommenget, D., M. Latif, 2002: A cautionary note on the interpretation of EOFs. J. Climate, **12**, 216-225. DOI: 10.1175/1520-0442(2002)

Garreaud R. and D. S. Battisti, 1999: Interannual (ENSO) and interdecadal (ENSO- like) variability in the Southern Hemisphere Tropospheric Circulation. J. Climate, **12**, 2113–2123. DOI: 10.1175/1520-0442(1999)

Haarsma, R. J., F. M. Selten, J. D. Opsteegh, 2000: On the mechanism of the Antarctic Circumpolar Wave. J. Climate, **13**, 1461-1480. DOI:10.1175/1520-0442(2000)013

Held, I. M., 2013: Climate science: The cause of the pause. Nature, **501**, 318-319. DOI: 10.1038/501318a

Hurrell J.W., 1995: Decadal trends in the North Atlantic Oscillation and relationship to regional temperature and precipitation. Science, **269**, 676–679. DOI: 10.1126/science.269.5224.676

Irving, D., & Simmonds, I. (2016). A new method for identifying the Pacific-South American pattern and its influence on regional climate variability. *Journal of Climate*, (2016). DOI: http://dx.doi.org/10.1175/JCLI-D-15-0843.1

Kayano, M. T., R. V. Andreoli, and R. A. Ferreira de Souza, 2013: Relations between ENSO and the South Atlantic SST modes and their effects on the South American rainfall. Int. J.

Climatol., **33**, 2008–2023. DOI: 10.1002/joc.3569

Kosaka, Y., S. P. Xie, 2013: Recent global-warming hiatus tied to equatorial Pacific surface cooling. Nature, **501**, 403-407. DOI: 10.1038/nature12534

Marengo, J. A., Liebmann, B., Grimm, A. M., Misra, V., Silva Dias, P. L., Cavalcanti, I. F. A., ... & Saulo, A. C. (2012). Recent developments on the South American monsoon system. *International Journal of Climatology*, *32*(1), 1-21. DOI: 10.1002/joc.2254

Mo, K. C., & Paegle, J. N. (2001). The Pacific–South American modes and their downstream effects. *International Journal of Climatology*, *21*(10), 1211-1229. DOI: 10.1002/joc.685

Morioka, Y., T. Tozuka, S. Masson, P. Terray, J. Luo, and T. Yamagata, 2012: Subtropical dipole modes simulated in a coupled general circulation model. J. Climate, **25**, 4029–4047. http://dx.doi.org/10.1175/JCLI-D-11-00396.1

Muñoz E., C. Wang, and D. Enfield, 2010: The Intra-Americas springtime sea surface temperature anomaly dipole as fingerprint of remote influences. J. Climate, **23**, 43–56. http://dx.doi.org/10.1175/2009JCLI3006.1

Murphy, B. F., & Timbal, B. (2008). A review of recent climate variability and climate change in southeastern Australia. *International journal of Climatology*, *28*(7), 859-879. DOI: 10.1002/joc.1627

NOAA, Climate Indices: Month Atmospheric and Ocean Time Series. http://www.esrl.noaa.gov/psd/data/climateindices/list/ (Accessed December 10, 2015).

Nnamchi, H. C., J. Li, and R. N. C. Anyadike 2011: Does a dipole mode really exist in the South Atlantic Ocean? J. Geophys. Res., **116**, D15104. DOI: 10.1029/2010JD015579

Pikovsky, A., M. Rosenblum, J. Kurths 2001: *Synchronization: A Universal Concept in Nonlinear Sciences*. Cambridge University Press, 432 pp.

Qiu, B., and F. F. Jin, 1997: Antarctic circumpolar waves: An indication of ocean-atmosphere coupling in the extropics. Geophys. Res. Lett., **24**, 2585–2588. DOI: 10.1029/97GL02694

Rial. J.A. , 2012: Synchronization of polar climate variability over the last ice age: in search of simple rules at the heart of climate's complexity. Am. J. Sci., **312** (4) 417– 448. DOI: 10.2475/04.2012.02

Rotstayn, L. D., and Coauthors, 2007: Have Australian rainfall and cloudiness increased due to the remote effects of Asian anthropogenic aerosols? *J. Geophys. Res.*, **112.**D09202, DOI:10.1029/2006JD007712

Servain, J., 1991: Simple climatic indices for the tropical Atlantic Ocean and some applications. J. Geophys. Res., **96**(C8), 15137–15146. DOI: 10.1029/91JC01046

Saji, N. H., B. N. Goswami, P. N. Vinayachandran, and T. Yamagata, 1999: A dipole mode in the tropical Indian Ocean. Nature, **401**, 360–363. http://dx.doi.org/10.1038/43854

Shakun, J. D., and J. Shaman, 2009: Tropical origins of North and South Pacific decadal variability, Geophys. Res. Lett., **36**, L19711, DOI:10.1029/2009GL040313.

Shi, G., Cai, W., Cowan, T., Ribbe, J., Rotstayn, L., & Dix, M. (2008). Variability and trend of North West Australia rainfall: observations and coupled climate modeling. *Journal of Climate*, *21*(12), 2938-2959. http://dx.doi.org/10.1175/2007JCLI1908.1

Smith, T. M., R. W. Reynolds, 2003: Extended reconstruction of global sea surface temperatures based on COADS data (1854-1997). J. Climate, **16**, 1495-1510. http://dx.doi.org/10.1175/1520-0442(2003)016<1495:erogss>2.0.co;2

Smith, T. M., R. W. Reynolds, T. C. Peterson, and J. Lawrimore, 2008: Improvements to NOAA's Historical Merged Land–Ocean Surface Temperature Analysis (1880– 2006). J. Climate, **21**, 2283–2296. http://dx.doi.org/10.1175/2007JCLI2100.1

Steinman, B. A., M. E. Mann, S. K. Miller, 2015: Atlantic and Pacific multidecadal oscillations and Northern Hemisphere temperatures. Science **347**, 988-991. DOI: 10.1126/science.1257856

Stenseth, N.C., G. Ottersen, J.W. Hurrell, A. Mysterud, M. Lime, K. S. Chan, N. G. Yoccoz, B. Ådelandsvik, 2003: Studying climate effects on ecology through the use of climate indices: the North Atlantic Oscillation, El Niño Southern Oscillation and beyond. Proc. R. Soc. Lond. B (270), 2087-2096. DOI: 10.1098/rspb.2003.2415

Talley, L. D., G. L. Pickard, W. J. Emery, J. H. Swift, 2011; *Descriptive Physical Oceanography: An Introduction*. Academic Press, 560 pp.

Trenberth, K. E., and J. W. Hurrell, 1994: Decadal atmosphere-ocean variations in the Pacific. Climate Dyn., **9**, 303-319. DOI: 10.1007/BF00204745

Ummenhofer, C. C., Sen Gupta, A., Taschetto, A. S., & England, M. H. (2009). Modulation of Australian precipitation by meridional gradients in East Indian Ocean sea surface temperature. *Journal of Climate*, *22*(21), 5597-5610. http://dx.doi.org/10.1175/2009JCLI3021.1

Venegas, S., L. Mysak, and D. Straub, 1996: Evidence for interannual and interdecadal climate variability in the South Atlantic. Geophys. Res. Lett., **23**, 2673– 2676. DOI: 10.1029/96GL02373

Yu, J., T. Liu, and C. R. Mechoso, 2000: An SST Anomaly Dipole In The Northern Subtropical Pacific And Its Relationships With ENSO, Geophys. Res. Lett., **27**(13), 1931-1934.

DOI: 10.1029/1999GL011340

Yuan, X. and D. G. Martinson, 2000: Antarctic Sea Ice Extent Variability and Its Global Connectivity. J. Climate, **13**, 1697–1717. http://dx.doi.org/10.1175/1520-0442(2000)013<1697:ASIEVA>2.0.CO;2

Wang, B., Huang, F., Wu, Z., Yang, J., Fu, X., & Kikuchi, K. (2009). Multi-scale climate variability of the South China Sea monsoon: a review. *Dynamics of Atmospheres and Oceans*, *47*(1), 15-37.23 http://dx.doi.org/10.1016/j.dynatmoce.2008.09.004

Wang, F., 2010: Subtropical dipole mode in the Southern Hemisphere: A global view. Geophys. Res. Lett., **37**, L10702. DOI: 10.1029/2010GL042750

White W. B., and R. G. Peterson, 1996: An Antarctic circumpolar wave in surface pressure, wind, temperature, and sea-ice extent. Nature, **380**, 699–70. DOI: 10.1038/380699a0

White, W. B., S. Chen, and R. G. Peterson, 1998: The Antarctic Circumpolar Wave: A Beta Effect in Ocean–Atmosphere Coupling over the Southern Ocean. J. Phys. Oceanogr., **28**, 2345–2361. http://dx.doi.org/10.1175/1520-0485(1998)028<2345:TACWAB>2.0.CO;2

Xue, Feng, Pinwen Guo, and Zhihao Yu: Influence of interannual variability of Antarctic sea-ice on summer rainfall in eastern China. *Advances in Atmospheric Sciences* 20.1 (2003): 97-102. DOI: 10.1007/BF033420

CHAPTER 4: IN SEARCH OF INTERMEDIATE, INTER-PROXY COMPARISONS: A
NOTE ON COMPLEXITIES OF AGE MODELS

Introduction:

Since the beginning of work studying the paleoclimate, the search for a unified age model
has been a constant problem. Early work was limited to major climate events, and even then,
only those younger than the Last Glacial Maximum (Catt and Candy, 2014). This limited
duration, millennial-scale resolution data was not capable of resolving global climate phase shifts
on a sub-Milankovitch timing, much less provide information on teleconnections in the ancient
climate, as there was no method of determining instantaneous events across any distance. While
significant advances have been made since this time (Walker, 2005; Noller et al., 2011; Lowe
and Walker, 2015), the question of timing and resolution of various age models remains largely
unresolved due to the nature of the proxy datasets available (Telford et al., 2003). The impacts of
unknown or poorly constrained errors in the proxy records are especially problematic when
investigating synchronization via instantaneous phase relationships, as detailed in Chapter One.
Here, we will discuss the strengths and weaknesses of available age models in the context of
searching for evidence of a mechanism of connections between the polar climates via a
collection of 161 intermediate oxygen isotope, ocean sediment core datasets, 80 Holocene, multi-
proxy datasets, with a specific focus on the study of inter-polar communication.

As mentioned in Chapter Two, while we may have strong evidence that the polar
climates are synchronized for the duration of the proxy record, and that they communicate via an

energy transfer with an ~1.67 kyr periodicity, the method of communication is still unknown. The simplest answer indicates a transfer of climate signal (via heat, dissolved gas, or other conserved water property) through the thermohaline circulation, as it remains largely isolated at depth. Tracing signal transfer in the deep ocean could provide further evidence for this hypothesis. Sediment cores with the same δ^{18}O paleoclimate proxy are available across the world's oceans, although their distribution is sporadic and therefore not ideal for a thorough study of paleo-ocean circulation. Moreover, the age models of these data series are often not published with clear error values, due partially to the nature of dating these ocean sediment cores, and partially to the age of some of the cores collected.

For this investigation, we collected 160, published, sediment core, δ^{18}O, climate proxy datasets, all available via NOAA. The full details of these, including core names, original publications, and author names are found in Table 1, along with details about the physical characteristics of the cores.

A Review of Commonly Used (and Misused) Age Models:

The methods of dating δ^{18}O paleoclimate proxy records can be broadly separated into isochronology (or radiometric chronometry), astrochronology, and sediment deposition rate models/layer counting, each of which come with their own particular challenges.

The latter is the most traditional method of age estimates, and may be used to great effect in some datasets. Early sediment cores (those pre-dating the 1970's) were often dated under the assumption of continuous sediment deposition rates, or some mostly stable model of deposition rates for the duration of the record. This is the case for at least one very important data set: the Shackleton and Opdyke (1973) core from the equatorial Pacific (V28238). This core showed a

continuous record of 700kyrs of oxygen isotopes, past the Brunhes-Matuyama geomagnetic boundary, allowing for one clear anchor-point in its age/depth model. For all intermediate dates, a constant sedimentation rate of $1.71*10^{-3}$ cm/a was assumed. Due to its continuous nature, this core was also used to calibrate other sediment cores, via visual matching and tuning. This has, of course, proved to be not an accurate manner of dating, but did reveal the first evidence of the Marine Isotope Stages (Bassinot et al., 1994). Several of the cores originally matched to the Shackleton core have not been updated. On the other hand, ice core chronologies, have been largely based on layer counting, which is used to great effect in the annually resolved, GICC05 dataset (Andersen et al., Rasmussen et al., 2006). Indeed, the resolution of this dataset has led to its use to calibrate a large number of other paleoclimate time series that show similar shapes over the period of observation, including a wide variety of sediment cores (Petersen et al., 2013, Schulz et al., 1998, Zhao et al., 2006). These cases assume an instantaneous, global response to orbital forcing, a problem which will be further discussed in the context of astrochronology. However, the GICC05, Greenland based age model comes with its own set of errors, based on depth and obscuring of clear layers. This error ranges from decadal at the sub 10ka mark to potentially around 1.9kyrs at 47ka, increasing the farther back in time the measurement is (Blockley et al., 2012). The AICC2012 age model, centered around Antarctic ice core chronologies, corrects for some of this potential error by improving modeling of ice compaction and movement, as well as augmenting itself with isotope dating methods and fixed markers where possible, but these additions come with their own additional potential error (Veres, 2013).

Isochronology includes radiocarbon dating (^{14}C Calibration), uranium-thorium (U-Th), and argon-argon (Ar-Ar) dating, and was largely developed in the 1950s and 60s. While these

techniques have advanced dramatically since they began, there are still a number of technical constraints, including standardizing lab equipment and methodologies, and, in the case of radiocarbon dating, a continually updated compilation radiocarbon calibration curve, which is regularly adjusted to reflect updates in our understanding of the paleoatmosphere's ^{14}C content (Lowe and Walker, 2015, Reimer et al., 2009, 2013). Moreover, for marine sediment cores, radiocarbon dates (which are only able to extend ~40ka) are largely impacted by marine reservoir effects (i.e., the effect of oceans acting as ^{14}C reservoirs in two layers, that due to surface mixing and atmospheric CO_2, and the deep ocean, which is isolated for long enough to have its own decay signature) and have been shown to be easily contaminated by modern ^{14}C during collection and processing (Beta Analytic; Yan et al. 2002). In general, the assumption is that U-Th dates come with multi-centennial to millennial error bars (Thompson and Goldstein, 2006, Stevens et al., 2007). Radiocarbon dates may be constrained to decadal uncertainties by some authors, especially in the more recent dates that can be calibrated via tree-ring or lake sediment chronologies, but are more often assumed to also be at least on the centennial scale, sometimes on the millennial scale, with errors compounding since the time of initial measurement (Ascough et al. 2005; Lowe et al., 2007; Austin et al., 2011; Lowe and Walker, 2015). Since 2002, IntCal, a working group sponsored by PAGES, has been responsible for maintaining older ^{14}C measurements, standardizing laboratory practices, and allowing external groups to update their own databases via the CALIB software package. However, in order to correct older data, the original ^{14}C measurements, from depth to curve to reservoir assumptions must be available, which is not always possible.

Astrochronology, the final major category of dating methodologies used in sediment records, is the use of the much more easily predicted and modeled orbital cycles that are largely

responsible for the amount of solar energy the Earth receives over time. This method of dating isotopic records dates back to 1976, at which point Hays et al. published the first study linking climate proxy oscillations to changes in astronomic forcing. Following this revelation, Imbrie et al. (1984) created a global benthic marine record stack, and tuned the records to the Milankovitch forcing. Other researchers did so on a more regional scale, hoping to preserve structural differences in the proxy records, but not temporal ones (Gibbard and West, 2000). Most recently, Lisiecki and Raymo (2005) gather 57 benthic sediment records, removed all previous age models from these cores and fit them to orbital forcing models. While this time series does span 5 million years, and has been widely used to discuss the timing of major changes in the paleoclimate (including the Mid Pleistocene Transition), this blind tuning is problematic. There is no way to definitively constrain error bounds for dates (Blaauw, 2012; Nowaczyk et al.; 2013), all nonlinear feedbacks, noise and responses in the climate system have been ironed out (Meyers and Hinnov, 2010), there is still no universally agreed upon way to tune the complex proxy records to the complex orbital forcing records (Lourens et al., 2010), and the practice of checking astronomically tuned series with isotope dating is still a work in progress, with error ranges given between 7 and 24ka (Channell et al., 2010). Milankovitch forcing is still absolutely the predominant driver of paleoclimate oscillations, as it provides the global climate system's major external energy source. However, the implementation of a flat global tuning, without careful study of different regions sensitivity to different Milankovitch cycles, may remove vital timing and rate information from the paleoclimate proxies, as well as introducing poorly described errors.

Overall, the ideal age model for any paleoclimate proxy record depends on the length, sampling frequency, and physical nature of the record. Currently, ice cores and tuning of local records to ice cores has the best described error of the age models mentioned, but is not widely applicable for our dataset. Radiocarbon dating also has a fairly well understood error range per sample, but only extends ~40ka, with few samples available. This does make astronomical tuning appealing, as it can be implemented for any record with an appropriate sample rate. However, on its own, astrochronolgy suppresses information about regional response variations and does not have a known error bound.

Available Records:

While NOAA maintains an online copy of published Paleoclimate datasets, with notes on their location, proxy type, and general indications of length, the database itself is not easily searchable by a number of parameters, including sampling rate and age model, and does not maintain the datasets in a standard format. In order to better understand what data is actually publicly available, with error bars, all $\delta^{18}O$ proxy records on the database were downloaded and preliminarily indexed by location. The global coverage is not ideal, as most cores are focused around large research institutions, with off shore New England, southern California, and Japan showing extremely thorough coverage, both in number of cores and resolution of samples. While useful in terms of looking at much longer periods in climate oscillations, none of these areas extend far enough to track a continuous signal transfer, and are often not deep enough to show signs of the deep ocean circulation.

Of the 160 available $\delta^{18}O$, ocean sediment core proxy records available, 81 have some radiocarbon data, with an average of 10 dated layers per an average length of 110,713 years, 36

of which have no published error values. 8 cores have been tuned to the Shackleton age model, and 86 have been tuned to SPECMAP. The specifics of the methods of tuning used in both the Shackleton and SPECMAP calibrated cores, including the strength of tuning parameters, and chosen tie points (often including MIS transitions, DO events, or other high frequency changes in the paleoclimate) are noted when available, but are not all available for any given core. Two have fixed dates based on paleomagnetics and all have some features tuned to ice core ages or MIS dates. Only 5 have any uranium-thorium dates, all of which extend beyond one million years. 57 of the included cores were used to create the LR04 stack age model, but only three of the cores in this database are currently tuned to the LR04 chronology. As mentioned earlier, the LR04 chronology does not include any isotopic dates or fixed points, and is solely based on a linear, globally instantaneous, response to orbital forcing (Lisiecki and Raymo, 2005).
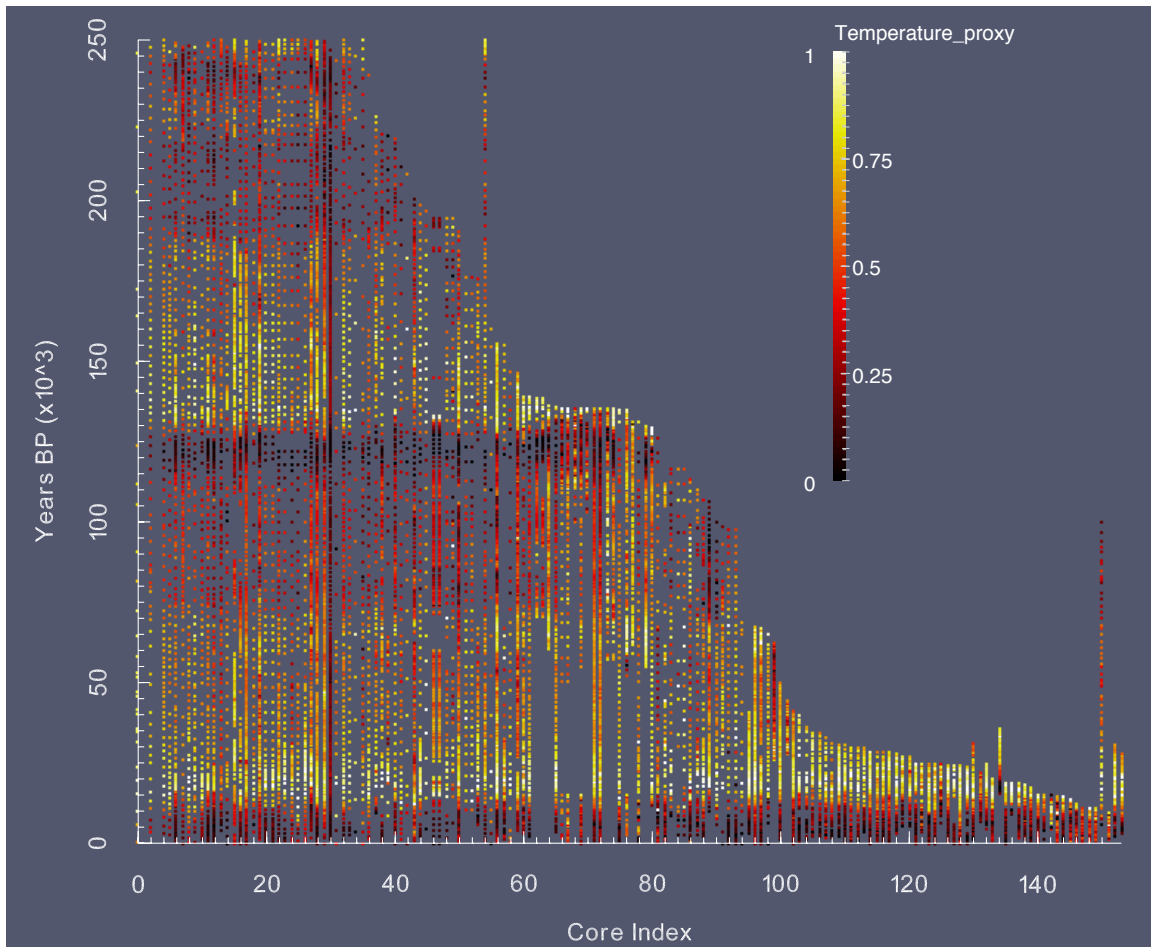
Figure 4.1 A plot of all 160 datasets, organized by length and truncated at 250kyrs for the purpose of showing the varying sampling rates, trend variations and coverages of these datasets.

When all of these datasets are plotted together (see Fig 1 and 2), obvious patterns emerge, despite these widely varying age models. Some clear, long term agreement, on the 10ky scale is seen. However, there are also distinct outliers at higher frequencies. In order to better show these outliers, the datasets have been plotted against the LR04 stack [Liesicki and Raymo, 2005] in Figure 2. While Figure 1 organizes the datasets by a simple index based on number of samples and length of time series, Figure 2 clusters the datasets based on their locations. This was done in the hopes of revealing any regional anomalies, such as those noted by Skinner and Shackleton (2005) when they observed an ~3.9 ky delay between Atlantic and Pacific benthic oxygen

122

signals following the last termination, among others (Ziegler et al., 2010; Caballero-Gill, 2012; An et al., 2011; Caley et al., 2013).
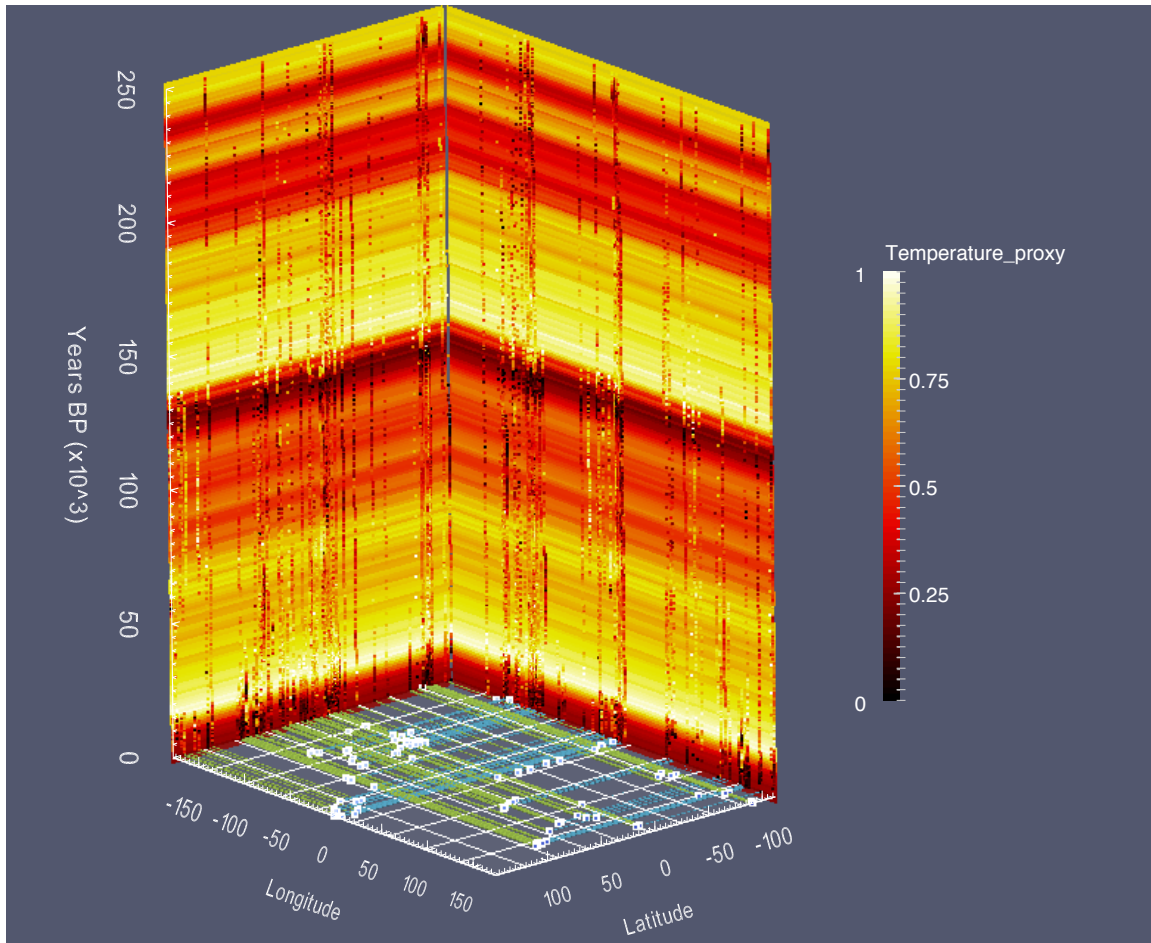
Figure 4.2. The database cores have been plotted on a long-lat map along the base of the figure, and then projected on the 250kyr, temporal z access against the LR04 climate signal to show the differences between the orbitally tuned global climate proxy and regionally organized datasets. Unfortunately, due to age model uncertainties in both the global and local signals, no definite statements can be made about the demonstrated outliers.

However, no consistent regional delay is apparent, either in this figure, or within the time series themselves. In part, this may be due to the vastly different sampling rates even within

regional groups. It is only compounded by age model uncertainties. A selection of a different age

model cores from regions thought to show delayed signal arrival is seen in Figure 3.
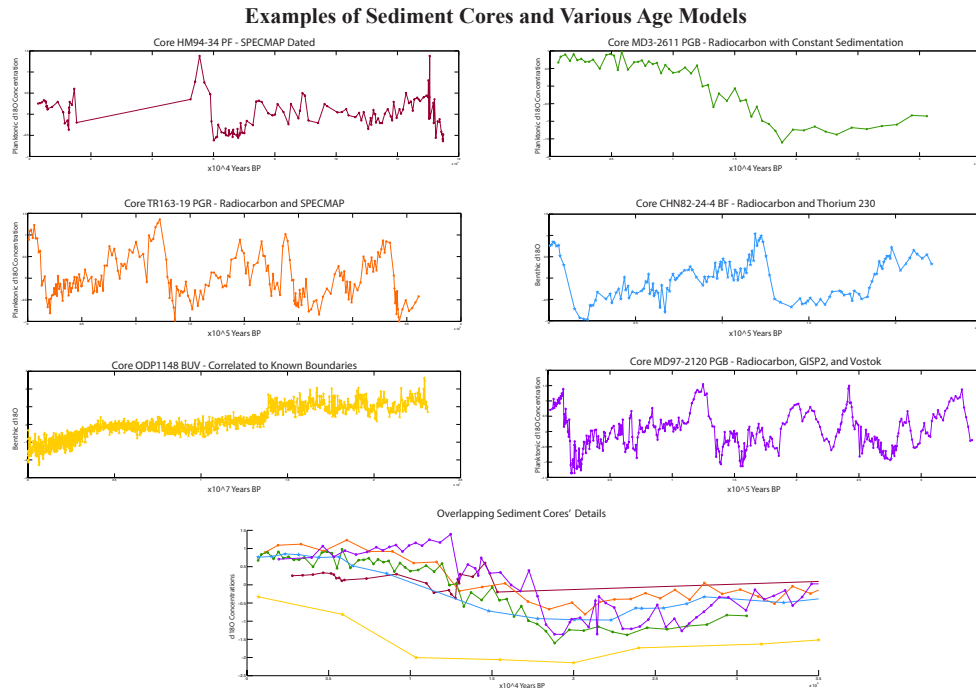
Figure 4.3: Examples of six of the 160 sediment cores, each of which rely predominantly on different age models. While they may appear compatible plotted concurrently, when plotted together, the problems of sampling rate and potential age model error are apparent, as a slight shift in any single point would greatly change the peak to trough phase relationships of the cores present.

Part III: Discussion and Conclusions

As has become clear in the above sections, even careful analysis of this large collection of sediment cores struggles to reliably resolve centennial to millennial scale phase relationships, as would be necessary to confirm or dismiss the thermohaline's signal transfer as the mechanism of polar connection. This is even more apparent when considering that the majority of available

datasets have been tuned to SPECMAP (in varying manners), inducing varying degrees of a flat phase relationship where possible. Still, several attempts have been made to circumvent the problem of age models while working within the database.

The first was an attempt to use only cores with two proxy datasets that would therefore be dated on the same age model. This is possible in cases where both planktonic and benthic $\delta^{18}O$ proxies are available for similar numbers of core slices, and exists in a total of 17 cores of the 160. In these cases, we hoped to resolve differences in surface ocean $\delta^{18}O$ signal and deep ocean circulation $\delta^{18}O$ signal. While this is a known phenomenon (Shackleton et al., 2000), it was not resolvable in these cores. This was largely due to an overall low sampling rate. However, more recent publications indicate that such cores will be publicly available in the near future.

The second attempt limited the age range of our datasets to the Holocene and added further, non-sediment data, including ice cores, lake sediments, and speleothems. While these datasets did allow for some intermediate measurements, the differences in proxy measurement types (chemically and physically), the inland nature of these signals and still sporadic sampling rates created uncertainties too large to be significantly compared individually. Following the example of the PAGES 2k group, the Holocene datasets were sorted into regional groups for the sake of comparison, but no stable phase differences were observed.

However, the database itself has been compiled specifically to be searched based on numerous age model constraints, is easily updateable with new age models, and will be of great use for other paleoclimate and paleoocean projects in the future. For now, several groups have been organized to facilitate the discussion between investigators collecting paleoclimate data and those analyzing it, on several scales. This ranges from the aforementioned PAGES 2k group, whose work is high frequency (ideally annual to decadal resolution proxy data for all continents)

but short scale; to the IsoAstro group whose work is on the million to hundred million year scale and seeks to provide a standard code set for entering age models such that they can be easily replicated across labs (Meyers et al., 2014); to the continued efforts of the IntCal working group mentioned earlier. These groups each focus on different aspects of multi-proxy collection and analysis, from combining annual, decadal, and centennial data trends in the past 2ky, to better constraining lab standards for Ar-Ar and U-Th dating, to careful continuous integration of new ^{14}C dating methods and reservoir information. While ocean sediment cores specifically have not been the focus of similar scrutiny, future work will follow their models, as well as making use of publications, meetings, and standards set by these groups.

FILE_NAME	PUBLICATION	COORDINATES		PROXY	LENGTH (yrbp)	AVG_SAMPLING (kyr)	MAX_SAMPLING (kyr)	TUNING_SCALE
M5A-43JC PSGR	Benway, H.M. et al, 2006	7.85583	-83.60833	Planktonic d18Osw g.rub	28290	0.247	1.95	Shackleton
M5A-43JC PVGR	Benway, H.M. et al, 2006	7.85583	-83.60833	Planktonic d18O g.rub	28290	0.234	1.3	Shackleton
M5A-43JC PVND	Benway, H.M. et al, 2006	7.85583	-83.60833	Planktonic d18O n.duter	28290	0.226	0.65	Shackleton
MD3-2611 PGB	Calvo, E. et al, 2007	-36.73333	136.55	Planktonic d18O g.bull	30601	0.534	1.221	
ODP984 PNP	Came, R.E. et al, 2007	61.43333	-24.08333	Planktonic d18O n.pachy	11099.5	0.079	0.239	
TR163-31 BCW	Chapman, M. et al, 1999	3.61667	-83.96667	Benthic d18O c.wuell	129990	0.577	1.38	
GH93 PGU	Crusius, J. et al, 1999	39.57195	139.4408	Planktonic d18O g.umbil	14970	0.316	1.57	
KT94-15 PGU	Crusius, J. et al, 1999	39.57195	139.4408	Planktonic d18O g.umbil	20240	0.293	0.8	SPECMAP
ODP981 BCW	Draut, A.E. et al, 2003	55.46667	-14.65	Benthic d18O c.wuell	3190200	2.25	16.7	
ODP980 BCW (Flower)	Flower, B.P. et al, 2000	55.485	-14.70167	Benthic d18O c.wuell	1003200	0.897	6.17	
JPC76 PGB	Friddell, J.E. et al, 2003	34.2711	-120.0728	Planktonic d18O g.bull	10968	0.008	0.134	
JPC76 PNP	Friddell, J.E. et al, 2003	34.2711	-120.0728	Planktonic d18O n.pachy	10968	0.008	0.134	
HM57-7 BF	Fronval, T. et al, 1997	68.43333	-13.86667	Benthic d18O forams	135100	2.383	35.5	SPECMAP
HM57-7 PF	Fronval, T. et al, 1997	68.43333	-13.86667	Planktonic d18O forams	135100	1.577	35.5	SPECMAP
HM71-19 BF	Fronval, T. et al, 1997	69.48333	-9.51667	Benthic d18O forams	135100	0.704	4.5	SPECMAP
HM71-19 PF	Fronval, T. et al, 1997	69.48333	-9.51667	Planktonic d18O forams	135100	1.287	40	SPECMAP
HM94-34 BF	Fronval, T. et al, 1997	73.76667	-2.53333	Benthic d18O forams	135100	0.837	3.81	SPECMAP
HM94-34 PF	Fronval, T. et al, 1997	73.76667	-2.53333	Planktonic d18O forams	134950	1.033	37.16	SPECMAP
ODP644 BF	Fronval, T. et al, 1997	66.6667	4.56667	Benthic d18O forams	131350	5.556	2.65	SPECMAP
ODP644 PF	Fronval, T. et al, 1997	66.6667	896	Planktonic d18O forams	131350	0.388	1.8	SPECMAP
HM52-43 BF	Fronval, T. et al, 1997	63.51667	-0.073333	Benthic d18O forams	14700	0.4	0.69	SPECMAP
HM52-43 PF	Fronval, T. et al, 1997	63.51667	-0.073333	Planktonic d18O forams	14700	0.4	0.69	SPECMAP
NH15P BBS	Ganeshram, R. et al, 1998	22.68333	-106.2727	Benthic d18O boliv.sp	120000	1.519	13.9	SPECMAP
NH8P BBS	Ganeshram, R. et al, 1998	22.38639	-107.0717	Benthic d18O boliv.sp	50200	0.35	0.4	SPECMAP
NH22P BUV	Ganeshram, R.S. et al, 1998	23.51778	-106.5178	Benthic d18O uvige	139000	1.267	5.8	SPECMAP
MD2-2551 PGR	Hill, H.W. et al, 2006	26.94611	-91.34611	Planktonic d18O g.rub	44461	0.036	0.092	
ODP704A PNP	Hodell, D.A. et al, 2000	-46.88334	7.41667	Planktonic d18O n.pachy	663080	1.589	17.6	SPECMAP
TN057-6 BCS	Hodell, D.A. et al, 2000	-42.90139	8.9	Benthic d18O cibid	438580	1.464	17.66	SPECMAP
TN057-6 PGB	Hodell, D.A. et al, 2000	-42.90139	8.9	Planktonic d18O g. bull	438580	1.464	17.66	SPECMAP
T5710-11 PNP	Hodell, D.A. et al, 2000	-47.1	5.91667	Planktonic d18O n.pachy	194630	0.896	39.46	SPECMAP
TN057-10-11 PNP	Hodell, D.A. et al, 2000	-47.1	5.91667	Planktonic d18O n.pachy	194630	0.891	39.46	SPECMAP
ODP982 BCW	Hodell, D.A. et al, 2010	57.50139	-15.8675	Benthic d18O c.wuell	8837700	3.774	596.8	Shackleton
ODP1060 BUP	Hoogakker, B.A.A. et al, 2007	30.7667	-74.4667	Benthic d18O u.pereg	62461.3	0.143	1.021	
RC11-120 PF (Imbrie)	Imbrie, J. et al, 1992	-43.51667	79.86667	Planktonic d18O forams	293000	1.602	8	Shackleton
CHN82-24-4 BF	Imbrie, J. et al, 1992	42	-33	Benthic d18O forams	220800	1.595	6.3	
RC13-110 BF	Imbrie, J. et al, 1992	0	96	Benthic d18O forams	609700	2.745	9.77	SPECMAP
RC13-229 BF	Imbrie, J. et al, 1992	-26	11	Benthic d18O forams	597700	3.637	12.6	SPECMAP
RC27-61 PF	Imbrie, J. et al, 1992	17	60	Planktonic d18O forams	434000	3.263	11	SPECMAP
V19-27 BF	Imbrie, J. et al, 1992	-0.46667	-82.06667	Benthic d18O forams	377800	2.007	8.6	SPECMAP
V19-30 BF	Imbrie, J. et al, 1992	-3	-83	Benthic d18O forams	340300	0.627	4.3	SPECMAP
K-11 BF	Imbrie, J. et al, 1992	72	2	Benthic d18O forams	65000	1.477	6.467	Shackleton
ODP1094 PF	Kanfoush, S.L. et al, 2002	-53.2	5.1	Planktonic d18O forams	443684	0.475	25.565	SPECMAP
KNR31 BCS	Keigwin, L.D. et al, 1994	28.245	-74.44	Benthic d18O cibid	138710	0.917	4.884	SPECMAP
KNR31 BNU	Keigwin, L.D. et al, 1994	28.245	-74.44	Benthic d18O n.umbon	138710	0.917	11.41	SPECMAP
HU73-031-7 PNP	Keigwin, L.D. et al, 1995	42.97833	-55.24833	Planktonic d18O n.pachy	20410	0.333	0.97	
V17-178 PNP	Keigwin, L.D. et al, 1995	43.48333	-54.86667	Planktonic d18O n.pachy	15420	0.32	0.826	
HU73-011-1 PNP	Keigwin, L.D. et al, 1995	43.21	-60.41	Planktonic d18O n.pachy	15400	0.164	2.533	
V17-178 PGR	Keigwin, L.D. et al, 1995	43.48333	-54.86667	Planktonic d18O g.rub	13765	0.494	0.826	
HU73-031-7 PGR	Keigwin, L.D. et al, 1995	42.97833	-55.24833	Planktonic d18O g.rub	12400	0.333	1.32	
V21-40 PGR	Koutavas, A. et al, 2003	-1.21667	-89.675	Planktonic d18O g.rub	34642	1.045	1.915	
V21-40 PGS	Koutavas, A. et al, 2003	-1.21667	-89.675	Planktonic d18O g.sacc	34642	1.045	1.915	
V19-28 PGR	Koutavas, A. et al, 2003	-2.36667	-84.65	Planktonic d18O g.rub	32991	0.802	2.252	
V19-28 PGS	Koutavas, A. et al, 2003	-2.36667	-84.65	Planktonic d18O g.sacc	31269	0.869	3.708	
R13-140 PGR	Koutavas, A. et al, 2003	-2.86667	-87.75	Planktonic d18O g.rub	30750	0.813	1.323	
V19-27 PGR	Koutavas, A. et al, 2003	-0.46667	-82.06667	Planktonic d18O g.rub	29840	0.908	1.538	
V19-27 PGS	Koutavas, A. et al, 2003	-0.46667	-82.06667	Planktonic d18O g.sacc	29840	0.968	1.538	
R11-238 PGR	Koutavas, A. et al, 2003	-1.51333	-85.81667	Planktonic d18O g.bull	28240	0.778	1.176	
RC8-102 PGR	Koutavas, A. et al, 2003	-1.41667	-86.85	Planktonic d18O g.rub	27070	0.867	1.555	
RC8-102 PGS	Koutavas, A. et al, 2003	-1.41667	-86.85	Planktonic d18O g.sacc	27070	0.834	1.555	
V21-30 PGS	Koutavas, A. et al, 2003	0.95	-89.35	Planktonic d18O g.sacc	22390	0.296	1.143	
R13-140 PGS	Koutavas, A. et al, 2003	-2.86667	-87.75	Planktonic d18O g.sacc	3750	0.813	1.323	
R11-238 PGS	Koutavas, A. et al, 2003	-1.51333	-85.81667	Planktonic d18O g.sacc	778	0.778	1.176	
ODP806B PGR	Lea, D.W. et al, 2000	0.31729	159.357	Planktonic d18O g.rub	470000	2.329	16.4	SPECMAP
TR163-19 PGR	Lea, D.W. et al, 2000	2.255	-90.95111	Planktonic d18O g.rub	361000	1.739	6	SPECMAP
TR163-19 BUS	Lea, D.W. et al, 2002	2.255	-90.95111	Benthic d18O uvige	361000	3.243	7.3	SPECMAP
TR163-22 BUS	Lea, D.W. et al, 2006	0.51667	-92.4	Benthic d18O u.sent	135100	0.321	1.2	Shackleton
TR163-22 PGR	Lea, D.W. et al, 2006	0.51667	-92.4	Planktonic d18O g.rub	135100	0.318	1.1	Shackleton
MD2-2529 PGR	Leduc, G. et al, 2007	8.20556	-84.12194	Planktonic d18O g.rub	88167	0.296	1.608	LR04
PL07-39PC PGB	Lin, H-L. et al, 1997	10.7	65.94167	Planktonic d18O g.bull	21243	0.111	0.393	
ODP769A PGR	Linsley, B.K., 1996	8.78559	121.2942	Planktonic d18O g.rub	149467	0.451	3.9	SPECMAP
R13-110 PND	Lyle, M. et al, 2002	0	-96	Planktonic d18O n.duter	622990	2.584	8.69	SPECMAP
V19-27 BCS	Lyle, M. et al, 2002	-0.46667	-82.06667	Benthic d18O cibid	377800	2.007	8.58	SPECMAP
V19-30 PND	Lyle, M. et al, 2002	-3	-83	Planktonic d18O n.duter	340300	0.628	3.85	SPECMAP
INMD114 BUV	Lyle, M. et al, 2002	8.8	-138.99	Benthic d18O uvige	312660	6.43	175.73	SPECMAP
RC10-62 PND	Lyle, M. et al, 2002	3.2	-101.4333	Planktonic d18O n.duter	256000	0.339	10.4	SPECMAP
Y71-10 PND	Lyle, M. et al, 2002	-6.6333	-106.95	Planktonic d18O n.duter	239000	2.667	33	SPECMAP
INMD114 PND	Lyle, M. et al, 2002	8.8	-138.99	Planktonic d18O n.duter	219960	4.305	39.5	SPECMAP
R13-115 PND	Lyle, M. et al, 2002	-1.38333	-104.5	Planktonic d18O n.duter	210500	3.541	8.59	SPECMAP
Y71-3-2 BUV	Lyle, M. et al, 2002	7.28333	-85.25	Benthic d18O uvige	176000	3.523	5.76	SPECMAP
Y71-3-2 PND	Lyle, M. et al, 2002	7.28333	-85.25	Planktonic d18O n.duter	176000	3.312	5.76	SPECMAP

Table1A

FILE_NAME	PUBLICATION	COORDINATES		PROXY	LENGTH (yrbp)	AVG_SAMPLING (kyr)	MAX_SAMPLING (kyr)	TUNING_SCALE
W84-14 PND	Lyle, M. et al, 2002	0.95	-138.95	Planktonic d18O n.duter	147000	3.956	110	SPECMAP
RC11-120 PGB	Mashiotta, T.A. et al, 1999	-43.51667	79.86667	Planktonic d18O g.bull	290700	3.2	10.7	SPECMAP
E11-2 PNP	Mashiotta, T.A. et al, 1999	-56.07306	-115.0931	Planktonic d18O n.pachy	106320	0.899	2.01	SPECMAP
ODP980 BF	McManus, J.F. et al, 1999	55.485	-14.70167	Benthic d18O forams	512210	0.766	8.89	SPECMAP
ODP980 PF	McManus, J.F. et al, 1999	55.485	-14.70167	Planktonic d18O forams	512210	0.59	4.45	SPECMAP
OPD849 BF	Mix, A.C. et al, 1995	0.18333	-110.5183	Benthic d18O forams	4978185	3.518	111.86	Shackleton;SPECMAP
OPD846 BF	Mix, A.C. et al, 1995	-3.095	-90.81834	Benthic d18O forams	1834900	2.632	21.58	Shackleton;SPECMAP
TT013-PC72 BCW	Murray, R.W. et al, 2000	0.10111	-139.4	Benthic d18O c.wuell	1045269	3.67	12.39	SPECMAP
ODP1170A BCW	Nuernberg, D. et al, 2004	-47.15056	146.0497	Benthic d18O c.wuell	450545	1.916	11.77	SPECMAP
MD2-2575 PGR	Nuernberg, D. et al, 2008	29.0167	-87.11889	Planktonic d18O g.bull	399670	0.574	2	LR04
MD2-2575 BUP	Nuernberg, D. et al, 2008	29.0167	-87.11889	Benthic d18O uvige	339670	0.594	5.32	LR04
MD2-2575 PGC	Nuernberg, D. et al, 2008	29.0167	-87.11889	Planktonic d18O g.crass	22239	0.147	0.679	
KT90-9 BEB	Oba, T. et al, 2004	41.11667	143.5167	Benthic d18O e.bat	24852	0.529	2.034	
KT90-9 PGB	Oba, T. et al, 2004	41.11667	143.5167	Planktonic d18O g.bull	24852	0.624	2.034	
MD1-2421 PGB	Oba, T. et al, 2004	36.01667	141.7833	Planktonic d18O g.bull	24850	0.327	0.85	
MD1-2421 PGI	Oba, T. et al, 2004	36.01667	141.7833	Planktonic d18O g.infla	24850	0.244	0.94	
MD1-2421 BBA	Oba, T. et al, 2004	36.01667	141.7833	Benthic d18O b.acule	24470	0.397	8.62	
K943 PGB	Oba, T. et al, 2004	38.88333	143.3667	Planktonic d18O g.bull	24400	0.317	0.969	
K943 BUS	Oba, T. et al, 2004	38.88333	143.3667	Benthic d18O u.sent	24119	0.831	2.846	
MD1-2421 BUS	Oba, T. et al, 2004	36.01667	141.7833	Benthic d18O u.sent	21320	0.272	1.32	
K90-9 BEB	Oba, T. et al, 2004	42.45	144.3167	Benthic d18O e.bat	18903	0.461	2.236	
K90-9 BUA	Oba, T. et al, 2004	42.45	144.3167	Benthic d18O u.akita	18903	0.549	2.236	
K90-9 PGB	Oba, T. et al, 2004	42.45	144.3167	Planktonic d18O g.bull	18903	0.48	1.665	
JPC8 BCW	Oppo, D.W. et al, 2001	61	-25	Benthic d18O c.wuell	135100	0.539	4.104	SPECMAP
JPC8 PNP	Oppo, D.W. et al, 2001	61	-25	Planktonic d18O n.pachy	135100	0.462	4.104	SPECMAP
ODP980 BCW (Oppo)	Oppo, D.W. et al, 2003	55.485	-14.70167	Benthic d18O c.wuell	9873	0.085	0.235	
MD97-2120 PGB	Pahnke, K. et al, 2003	-45.53444	174.9308	Planktonic d18O g.bull	340830	0.944	2.42	Shackleton
MW91-15 PGR	Patrick, A. et al, 1997	-0.02306	158.9411	Planktonic d18O g.rub	29840	0.82	1.26	
TR163-31 PGR	Patrick, A. et al, 1997	-3.62	-83.97334	Planktonic d18O g.rub	24650	0.665	1.91	
NIOP464 PND	Reichart, G.J. et al, 1998	22.25056	63.58361	Planktonic d18O n.duter	226000	1.95	7.5	Lourens
NIOP497 PND	Reichart, G.J. et al, 1998	17.45	57.95111	Planktonic d18O n.duter	175700	2.26	58.9	Lourens
NIOP455 PND	Reichart, G.J. et al, 1998	23.55056	65.95	Planktonic d18O	116700	2.505	5.7	Lourens
RC11-120 PF (Rickaby)	Rickaby, R.E.M. et al, 1999	-43.51667	79.86667	Planktonic d18O	139000	1.425	3	SPECMAP
RC11-120 PGB 2	Rickaby, R.E.M. et al, 1999	-43.51667	79.86667	Planktonic d18O g.bull	139000	1.425	3	SPECMAP
MD88-769R PGB	Rickaby, R.E.M. et al, 1999	-46.06667	90.11667	Planktonic d18O g.bull	136020	0.464	1.47	SPECMAP
E49-19R PGB	Rickaby, R.E.M. et al, 1999	-43.88694	90.1	Planktonic d18O g.bull	283670	12.177	27.08	SPECMAP
R12-225 PGR	Rickaby, R.E.M. et al, 1999	-53.64833	-123.1167	Planktonic d18O g.bull	208000	8.667	26	
E48-22R PGB	Rickaby, R.E.M. et al, 1999	-39.9	85.42	Planktonic d18O g.bull	196700	4.922	7.63	SPECMAP
E49-18R PGB	Rickaby, R.E.M. et al, 1999	-46.05	90.16667	Planktonic d18O g.bull	129490	1.047	2	SPECMAP
MD97-2141 PGR	Rosenthal, Y. et al, 2003	8.78333	121.2833	Planktonic d18O g.rub	146440	0.083	5.38	SPECMAP
M35003-4 PGR	Ruehleman, C. et al, 1999	12.08333	-61.25	Planktonic d18O g.rub	28440	0.334	0.75	
ODP999A PGR	Schmidt, M.W. et al, 2004	12.75	-78.73333	Planktonic d18O g.rub	135900	1.193	2.82	SPECMAP
VM28-122 PGR	Schmidt, M.W. et al, 2004	11.5667	-78.41667	Planktonic d18O g.rub	68960	0.412	0.82	SPECMAP
GeoB10285 PGB	Schneider, R.R. et al, 1995	-20.10333	9.185	Planktonic d18O g.bull	219400	1.844	4	SPECMAP
GeoB10163 PGB	Schneider, R.R. et al, 1995	-11.76722	11.68167	Planktonic d18O g.bull	200600	0.74	3.1	SPECMAP
GeoB10083 PGR	Schneider, R.R. et al, 1995	-6.58167	10.31833	Planktonic d18O g.rub	190500	0.892	5.1	SPECMAP
RC17-177 PF	Shackleton, N.J. 1987	2	159	Planktonic d18O forams	69000	4.059	9.87	SPECMAP
ODP677 BF	Shackleton, N.J. et al, 1990	1.2	-83.73333	Benthic d18O forams	100000	1.918	6	SPECMAP
ODP677 PF	Shackleton, N.J. et al, 1990	1.2	-83.73333	Planktonic d18O forams	10000	1.741	3	SPECMAP
RS147-GC07 PGB	Sikes, E.L. et al, 2009	-45.15	146.2833	Planktonic d18O g.bull	40020	0.658	5.581	SPECMAP
RS147-GC07 BCS	Sikes, E.L. et al, 2009	-45.15	146.2833	Benthic d18O cibid	36197	1.122	5.581	SPECMAP
74KL PGR	Sirocko, F. et al, 1993	14.32111	57.34694	Planktonic d18O g.rub	24570	0.307	0.5	
TR163-19 PGM	Spero, H.J. et al, 2003	2.255	-90.95111	Planktonic d18O g.menar	361000	2.902	7.3	SPECMAP
TR163-19 PGS	Spero, H.J. et al, 2003	2.255	-90.95111	Planktonic d18O g.sacc	361000	3.428	8.5	SPECMAP
TR163-19 PND	Spero, H.J. et al, 2003	2.255	-90.95111	Planktonic d18O n.duter	361000	2.812	7.3	SPECMAP
TR163-19 PGR	Spero, H.J. et al, 2003	2.255	-90.95111	Planktonic d18O g.rub	169700	1.606	6	SPECMAP
EW9504-04 BCM	Stott, L.D. et al, 2000	32.28333	-118.4	Benthic d18O c.mckan	198380	2.281	7.06	SPECMAP
EW9504-02 BCM	Stott, L.D. et al, 2000	31.25	-117.5833	Benthic d18O c.mckan	194310	2.749	10.6	SPECMAP
EW9504-02 PGB	Stott, L.D. et al, 2000	31.25	-117.5833	Planktonic d18O g.bull	194310	2.68	9.46	SPECMAP
EW9504-04 PGB	Stott, L.D. et al, 2000	32.28333	-118.4	Planktonic d18O g.bull	155180	2.559	53.95	SPECMAP
EW9504-09 BCM	Stott, L.D. et al, 2000	32.86667	-119.9667	Benthic d18O c.mckan	135080	1.72	7.43	SPECMAP
EW9504-08 BCM	Stott, L.D. et al, 2000	34.8	-118.8	Benthic d18O c.mckan	130980	2.176	6	SPECMAP
EW9504-08 PGB	Stott, L.D. et al, 2000	34.8	-118.8	Planktonic d18O g.bull	126320	2.331	10.33	SPECMAP
EW9504-09 PGB	Stott, L.D. et al, 2000	32.86667	-119.9667	Planktonic d18O g.bull	113230	1.581	7.43	SPECMAP
EW9504-05 PGB	Stott, L.D. et al, 2000	32.48333	-118.1333	Planktonic d18O g.bull	112240	2.103	10.95	SPECMAP
EW9504-05 BCM	Stott, L.D. et al, 2000	32.48333	-118.1333	Benthic d18O c.mckan	107020	1.417	5.89	SPECMAP
AHF16832 BCM	Stott, L.D. et al, 2000	31.6667	-118.1833	Benthic d18O c.mckan	48590	0.885	2.44	SPECMAP
MD2181 PGR	Stott, L.D. et al, 2002	6.3	125.8333	Planktonic d18O g.rub	67592	0.083	0.694	
MD2181 PGS	Stott, L.D. et al, 2002	6.3	125.8333	Planktonic d18O g.sacc	67097	0.345	4.184	
A7 PGR	Sun, Y. et al, 2005	28.01361	126.0164	Planktonic d18O g.rub	18193	0.075	0.1475	
A7 PGR 2	Sun, Y. et al, 2005	28.01361	126.0164	Planktonic d18O g.rub	17677	0.074	0.15	
ODP1143 BCW	Tian, J. et al, 2002	9.36194	113.2853	Benthic d18O c.wuell	98500	2.052	13.839	MIS
ODP1148 BUV	Tian, J. et al, 2008	18.83611	116.5656	Benthic d18O uvige	23103000	14.724	92.7	
ODP982 BCS	Venz, K.A. et al, 1999	57.50139	-15.8675	Benthic d18O cibid	97788	2.081	2.481	Shackleton;MIS
ODP982 PGB	Venz, K.A. et al, 1999	57.50139	-15.8675	Planktonic d18O g.bull	97788	2.081	2.481	Shackleton;MIS
17940-1_2 PGR	Wang, L. et al, 1999	20.11667	117.3833	Planktonic d18O g.rub	41132	0.056	0.266	
R657 PGB	Weaver, P.P.E. et al, 1998	-42.5333	-178.4917	Planktonic d18O g.bull	160150	8.008	12.4	
Q200 BF	Weaver, P.P.E. et al, 1998	-45.995	172.025	Benthic d18O forams	116700	5.429	19.737	SPECMAP
Q200 PF	Weaver, P.P.E. et al, 1998	-45.995	172.025	Planktonic d18O forams	116700	3.677	5.865	SPECMAP
MD03-2707 PGR	Weldeab, S. et al, 2007	2.50194	9.39472	Planktonic d18O g.rub	155420	0.165	1	

Table 1B

REFERENCES

An Z, Clemens SC, Shen J, et al. 2011. Glacial-interglacial Indian summer monsoon dynamics. Science 333: 719–723.

Andersen KK, Svensson A, Rasmussen SO, et al. 2006. The Greenland Ice Core Chronology 2005, 15–42 ka. Part 1: construct- ing the time scale. Quaternary Science Reviews 25: 3246–3257.

Ascough P, Cook G, Dugmore A. 2005. Methodological approaches to determining the marine radiocarbon reservoir effect. Progress in Physical Geography 29: 532–547.

Austin WEN, Telford RJ, Ninnemann US, et al. 2011. North Atlantic reservoir ages linked to high Younger Dryas atmospheric radiocarbon concentrations. Global and Planetary Change 79: 226–233.

Beta Analytic, "Marine Radiocarbon Resevoir Effect, AMS Dating." http://www.radiocarbon.com/marine-reservoir-effect.html. Accessed 08/01/2016.

Blaauw M, Bakker R, Christen JA, et al. 2007. A Bayesian framework for age-modelling of radiocarbon-dated peat deposits: case studies from the Netherlands. Radiocarbon 49: 357–367. Bassinot, Frank C., et al. "The astronomical theory of climate and the age of the Brunhes-Matuyama magnetic reversal." *Earth and Planetary Science Letters* 126.1-3 (1994): 91-108.

Blockley SPE, Lane CS, Hardiman M, et al. 2012. Synchronisation of palaeoenvironmental records over the last 60,000 years, and an extended INTIMATE event stratigraphy to 48,000 b2k. Quaternary Science Reviews 36: 2–10.

Catt J, Candy I (eds). 2014. *The History of the Quaternary Research Association.* Quaternary Research Association London.

Caballero-Gill RP, Clemens SC, Prell WL. 2012. Direct correlation of Chinese speleothem d18O and South China Sea planktonic d18O: transferring a speleothem chronology to the benthic marine chronology. Paleoceanography 27, doi:10.1029/2011PA002268

Caley T, Malaiz_e B, Kageyama M, et al. 2013. Bi-hemispheric forcing for Indo-Asian monsoon during glacial terminations. Quaternary Science Reviews 59: 1–4.

Channell JET, Hodell DA, Singer BS, et al. 2010. Reconciling astrochronological and 40Ar/39Ar ages for the Matuyama-Brunhes boundary and late Matuyama Chron. Geochemistry, Geophysics, Geosystems 11: doi:10.1029/2010GC003203

Gibbard PL, West RG. 2000. Quaternary chronostratigraphy: the nomenclature of terrestrial sequences. Boreas 29: 329–336.
Hays JD, Imbrie J, Shackleton NJ. 1976. Variations in the earth's orbit: pacemaker of the Ice Ages. Science 194: 1121–1132.

Imbrie J, Hays JD, Martinson DG, et al. 1984. The orbital theory of Pleistocene climate: support from a revised chronology of the marine d18O record. Terminations. In Milankovitch and Climate Berger A, Imbrie J, Hays J, et al. (eds). Reidel: Dordrecht; 269–306.

Lisiecki LE, Raymo ME. 2005. A Pliocene-Pleistocene stack of globally distributed benthic d18O records. Paleoceanography 20, PA1003, doi: 10.1029/2004PA001071
Lowe J, Walker M. 2015. Reconstructing Quaternary Environments (3rd ed.). Routledge: London.

Lowe JJ, Blockley S, Trincardi F, et al. 2007. Age modelling of late Quaternary marine sequences in the Adriatic: towards improved precision and accuracy using volcanic event stratigraphy. Conti- nental Shelf Research 27: 560–582.

Lowe JJ, Rasmussen SO, Bjo€rck S, et al. 2008. Synchronisation of palaeoenvironmental events in the North Atlantic region during the Last Termination: a revised protocol recommended by the INTI- MATE group. Quaternary Science Reviews 27: 6–17.

Lourens LJ, Becker J, Bintanja R, et al. 2010. Linear and non-linear response of late Neogene glacial cycles to obliquity forcing and implications for the Milankovitch theory. Quaternary Science Reviews 29: 352–365.

Meyers SR, Hinnov LA. 2010. Northern hemisphere glaciation and the evolution of Plio-Pleistocene climate noise. Paleoceanography 25, doi:10.1029/2009PA001834

Meyers, Stephen R., Bradley S. Singer, and Mark D. Schmitz. "Exploring Radioisotopic Geochronology and Astrochronology." *Eos* (2015).

Noller JS, Sowers JS, Sowers JM, et al. 2011. Quaternary geochronolo- gy: methods and applications. American Geophysical Union, AGU Reference Shelf Series, Vol. 4 (published on-line, doi:10.1029/ RF004p0001)

Nowaczyk NR, Haltia EM, Ulbricht D, et al. 2013. Chronology of Lake El'gygytgyn sediments - a combined magnetostratigraphic, palaeoclimatic and orbital tuning study based on multi-parameter analyses. Climate of the Past 9: 2413–2432.
Petersen SV, Schrag DP, Clark PU. 2013. A new mechanism for Dansgaard-Oeschger cycles. Paleoceanography 28: 24–30.

Rasmussen SO, Andersen KK, Svensson AM, et al. 2006. A new Greenland ice core chronology for the last glacial termination. Journal of Geophysical Research 111: doi:06110.01029/ 02005JD006079.

Reimer, Paula J., et al. "IntCal09 and Marine09 radiocarbon age calibration curves, 0-50,000 years cal BP." *Radiocarbon* 51.4 (2009): 1111-1150.

Reimer, Paula J., et al. "IntCal13 and Marine13 radiocarbon age calibration curves 0-50,000 years cal BP." (2013).

Schulz H, von Rad U, Erlenkueser H, et al. 1998. Correlation between Arabian Sea and Greenland climate oscillations of the past 110,000 years. Nature 393: 54–57.

Shackleton NJ, Opdyke ND. 1973. Oxygen isotope and palae- omagnetic stratigraphy of equatorial Pacific core V28-238: oxygen isotope temperatures and ice volume on a 105 and 106 year scale. Quaternary Research 3: 39–55.

Skinner LC, Shackleton NJ. 2005. An Atlantic lead over Pacific deep- water change across Termination I: implications for the application of the marine isotope stage stratigraphy. Quaternary Science Reviews 24: 571–580.

Stevens T, Armitage SJ, Lu H, et al. 2007. Examining the potential of high sampling resolution OSL dating of Chinese loess. Quaternary Geochronology 2: 15–22.

Telford RJ, Heegaard E, Birks HJB. 2004. All age-depth models are wrong: but how badly ? Quaternary Science Reviews 23: 1–5.

Thompson WG, Goldstein SL. 2006. A radiometric calibration of the SPECMAP timescale. Quaternary Science Reviews 25: 3207–3215.

Veres, D., L. Bazin, A. Landais, Mahamadou Kele, H. Toyé, B. Lemieux-Dudon, F. Parrenin et al. "The Antarctic ice core chronology (AICC2012): an optimized multi-parameter and multi-site dating approach for the last 120 thousand years." *Climate of the Past* 9, no. 4 (2013).

Walker M. 2005. Quaternary Dating Methods. John Wiley & Sons: Chichester.

Yan, Zheng, et al. "Challenges in radiocarbon dating organic carbon in opal-rich marine sediments." *Radiocarbon* 44.1: 123-136.
Zhao M, Huang C.-Y, Wang C-C, et al. 2006. A millennial-scale U37K0 sea-surface temperature record from the South China Sea (8˚N) over the last 150 ka: monsoon and sea-level influence. Palaeogeography Palaeoclimatology Palaeoecology 236: 39–55.

Ziegler M, Lourens LJ, Tuenter E, et al. 2010. Precession phasing offset between Indian summer monsoon and Arabian Sea produc- tivity linked to changes in Atlantic overturning circulation. Paleo- ceanography 25: doi:10.1029/2009PA001884

APPENDIX 1: CHAPTER ONE SUPPLEMENTAL INFORMATION

The Supplemental Information for Chapter 1 is as follows:

Supplemental Materials

Section 1:

1. Frequency modulation

1.1 Forced linear climate oscillator To illustrate how the 413ky eccentricity can frequency modulate the ~100ky glaciations we recall the simple, conceptual representation of a climatic oscillator[8, 18] where a linear extent of the ice sheet, $L(t)$, satisfies an equation of the form $L'' + \Omega^2 L = 0$. Here, $\Omega = (1/C_L C_T)^{1/2}$ is the angular frequency of one predominant mode of oscillation (e.g., $\Omega \sim 2\pi/100$ky) of the ice sheet, C_T is the ocean's thermal overturning time, and C_L the ice sheet's response time (thermal inertia).

The oscillator is externally forced by assuming that C_L is proportional to a critical dimension of the ice sheet[18] and will respond to external orbital forcing (413ky eccentricity in this case) through the feedback that makes the natural frequency Ω a time function dependent on the amplitude of the orbital forcing cycle. That is, we write $C_L(t) = C_L(1 + \Delta C_L/C_L \cos\omega\, t)$ with $\Delta C_L \ll C_L$ and $\omega = 2\pi/413$ky to represent amplitude modulation. Substituting into the original equation gives $L'' + \Omega^2 [1 + 2(\Delta\Omega/\Omega)\cos\omega\, t]L = 0$, a Mathieu differential equation whose solutions $L(t) \sim A \sin[\Omega t + (\Delta\Omega/\omega)\sin\omega\, t + \varphi]$, with A and φ integration constants, are frequency modulated functions[8, 21]. The function $Fm(t)$ described in Methods and in Figs. 1 and S1 is chosen to have this form. The ratio $\varepsilon = \Delta\Omega/\omega$ is an observable called the frequency modulation index, or FMI (see   Methods). Fig. S1 shows the signals and corresponding correlation coefficients between the frequency modulated signal $Fm(t)$ and the LR04 data as FMI increases (see Methods). Three examples that

include the signals and the inset show how the correlation coefficient varies for the physically plausible range of ε. Starting at ε=0.0, the initial amplitude and initial derivative of *Fm(t)* are very similar to that of the filtered data, but the rest of the time series is not. As ε increases *Fm(t)* approaches the data as the correlation coefficient increases until it reaches a maximum of 0.775 at ε = 1.75. This value compares well with ε = 1.72 that can be directly estimated from the data (see Methods). Spectral evidence of frequency (phase) modulation on the data is shown in Figs. S2-S4. Fig. S2 shows evidence for frequency (phase) modulation in the spectrum of the untuned benthic stack LR041, 19, 20 in the form of side-lobes separated from the main ~100ky 'carrier' by integer multiples of the modulating frequency (1/413ky, or 2.42x10-6 yr-1). In contrast, the spectrum of the tuned LR04 stack clearly shows how the tuning process obliterated the frequency modulation evidence while likely introducing substantial power in the 1/41ky frequency band. Fig. S3 compares the multitaper23 power spectra of the untuned, low-pass LR04 stack and that of the *ad hoc* signal *Fm(t)*. Both spectra display side- lobes at 125ky, 77ky, 64.5ky and 55.5ky. In *Fm(t)*, the side-lobes are caused by frequency modulation. Notice that in neither spectra there is statistically significant power at the frequency 1/413ky of the modulating signal that in *Fm(t)* is the rectified cosine shown in Fig. 1d of the main text. In both figures S2 and S3 the power spectrum of the theoretical eccentricity forcing is displayed for comparison.

1.2 Forced nonlinear ice volume model. Results using a nonlinear model of ice volume/ocean temperature/carbon dioxide evolution are shown in Fig. S4. Slightly modified here and fully described in Saltzman's (Ch. 15, page 284), in dimensionless variables the model is written as:

$$x'=-x-vx$$

$$y'=pz+ry-sy^2-y^3+A \, ||\cos(\omega_m t-\psi)|| \qquad\qquad (S-1)$$

$$z'=-q(x+z)$$

The variable x represents global ice volume, y is the atmospheric concentration of CO_2 and z is mean ocean temperature. In Fig. S4 a close fit to the data and to the timing of most glacial terminations (within age uncertainty) obtains as the model given by equations S-1 is forced with the 1/413ky rectified cosine that simulates the eccentricity function (see Fig. 1d) with amplitude A=1. This value of the eccentricity forcing's amplitude is small as compared to the amplitude of the unforced and forced functions (note the amplitude scale in Figure S4 is the same for the forced and unforced cases). This indicates that the actual forcing by the 413ky eccentricity could be small and still produce the frequency modulation effect shown. Comparison of the power spectra of the original free oscillation (dashed) and the forced model clearly show the effect of synchronization on the natural frequencies (peak frequencies are shifted to lower frequencies due to synchronization) and frequency modulation is evidenced by the strong sidelobes at 128ky, 79ky, 65ky and 55ky, consistent with the observed (Figs. S2, S3). We note that the 413ky peak (not shown) is two orders of magnitude smaller than that at 98ky, which is also consistent with the observations. Long-term energy transfer as shown in Fig 4a for the actual data is not reproduced by the model which only simulates the last ~1My and includes no mechanism for nonlinear energy transfer as observed. On the other hand, the model captures the amplification that occurs when the frequency detuning is of the order of 20% to 10% of the forcing frequency or one of its harmonics, or when the forcing level increases, as will be shown shortly. The model's quadratic and cubic nonlinearities closely reproduce the saw- tooth shape of the LR04 waveform over the last 0.8My (Fig. S4) and shows that frequency modulation is responsible for

the 125ky—82ky variation in duration of the glaciation cycles which within age uncertainty fit the timing of the terminations4 (Roman numerals). The implication is that only forcing with the simulated 1/413ky eccentricity is needed to closely reproduce the major features of the record. Further, transformation of the forcing 413ky amplitude into frequency modulation of the natural oscillation of the climate system is consistent with the power transfer from the 1/413ky band to the 1/100ky band displayed by Fig. 4.

1.3 The missing 413ky power: In Figs. S2 and S3 the spectrum of the theoretical orbital eccentricity exhibits a strong peak at 1/413ky because the eccentricity forcing has the form of a rectified sinusoid of period ~100ky that is in turn amplitude-modulated by the longer 413ky signal, which also has the form of a rectified sinusoid. This combination produces a spectrum with a strong peak at 1/413ky of amplitude slightly greater than the 1/100ky peak. In contrast, the spectrum of the LR04 stack shows negligible power at 1/413ky (compared to 1/100ky power) and at the same time a wide bandwidth associated with the carrier (~1/100ky), evidence of frequency modulation (Fig. S2, top panel). This is expected of a frequency modulated sinusoid, and there is no reason to expect that the climate's natural oscillations in the ~100ky band should be rectified sinusoids, unless they are linearly following the forcing and thus acquiring the 100ky forcing waveform. If they did, the LR04 spectrum should have a strong peak at 413ky, which it does not, as shown in Figs S2, S3.

Figs. 2,3, S9, S10 suggest that the ~100ky glacial cycles are of internal origin, and that when forced by the 413ky eccentricity forcing undergo frequency modulation, as shown in Fig. S4.

2. Nonlinear synchronization

The response of a multi-period nonlinear oscillator to multi-frequency forcing is very complex and theoretical results available mostly from engineering research [Nayfeh and Mook,

135

1995] show that resonance between a natural period can occur not just to a single forcing frequency but to linear combination of forcing frequencies. For instance, since 1/95ky – 1/125ky ~ 1/413ky, a natural period of the climate close to 95ky could resonate with the combination forcing frequency 1/125ky–1/413ky = 1/181ky. For a complex climate system many other combinations can certainly occur.

Figs. S6-S8 show details of the analysis summarized in Fig. 3. The behavior of the relative phase between the modulator and the eccentricity forcing over the last 5My (Fig. S9) suggests that phase lock began around 1.1-1.2Ma (see main text). Fig. S10 shows the phase, phase difference function $\Delta\Phi(t)$ and spectrogram of the LR04 stack from 0My to 5My. The decrease of $\Delta\Phi(t)$was nearly monotonic for ~4My, with an average rate of decrease of 2 cycles per million years. The modern ice ages started around 3.6Ma [Mudelsee and Raymo, 2005].

Fig. S11 shows the nonlinear effect of synchronization in the spectral domain as a function of an external forcing which is a simulated 413ky eccentricity signal. The figure is based on calculations performed with model S-1described above, where to obtain the fit of the LR04 record a 1/413ky forcing level of A=1.0 was sufficient.

Similar results are well known for the synchronization of nonlinear oscillators to periodic external forcing [Gonzalez-Miranda, 2004]. The intermediate process where many different spectral peaks appear (e.g., Fig S11) should not be confused with the side-lobes created by frequency modulation of the 1/100ky frequency band. The latter happen for large detuning and do not produce amplification (see Fig. S4). The side-lobes shown in Fig. S11 occur for small detuning and very small levels of forcing, and are unstable to small changes in forcing amplitude, and thus unlikely to appear in the data. For A equal or greater than the largest values shown in the figure there is amplification of the signal at the forcing frequency and the side-lobes

disappear. Power gain or amplification is measured by the ratio of the spectral peaks P1 (forcing frequency) to P0 (natural frequency). In the model, amplification of the order of 300% to 1000% is not unusual when the natural frequency of the climate system is within 15% - 10% of the forcing frequency or one of its harmonics. We find similar spectral amplification relationships (not shown) for natural frequencies in the ~100ky band forced by the 97ky component of eccentricity.

One implication of the above discussion is that natural periods of oscillation of the climate system that happen to be close to the Milankovitch cycles (or their linear combinations) are most amplified by the astronomical forcing through forced synchronization (e.g., Fig S11). The climate system's natural free oscillations are likely a function of, among many others, the dimensions, relaxation times, and thermal inertia of the combined elements of the climate, though why exactly they are in the frequency bands they appear to be is beyond our grasp.

3. Effect of amplitude modulation

As mentioned in the main text the LR04 proxy record shows amplitude modulation so that an error could be made by extracting the frequency modulator without having first eliminated the effect of amplitude modulation. Fortunately, the degree of amplitude modulation is low (parameter *a* in equation 2 is 0.25) and the usual method of extracting the amplitude modulator [Lathi and Ding, 2009] can be used successfully. Not removing the amplitude modulation would only produce a second order effect and would not affect our conclusions.

4. Effect of noise

Intuitively, the presence of noise makes synchronization seem improbable14. However, nonlinear systems (including chaotic oscillators) though subject to large noise fluctuations can still synchronizeS5. The 1.2My synchronization interval is reasonably longer than the period of

the external forcing, and shows statistically significant different distribution of $\Delta\Phi(t)$ before and after 1.2Ma. These characteristics strongly suggest effective synchronization [Anishchenko et al., 2002] is not significantly affected by noise.

APPENDIX 2: CHAPTER TWO SUPPLEMENTAL INFORMATION

The Supplemental information for Chapter 2 is as follows:

Supplementary Materials:

Age Model Details and Reasoning

While both AICC2012 (Veres et al., 2013) and Brooks et al.'s (Blunier et al., 2007) methane matched age models involve cores from both poles, the methane matched age model's focus on synchronizing dates between the polar climates makes it the most ideal for cross comparison analysis, despite being somewhat older than the AICC2012 work, and its larger uncertainties in absolute age. The AICC2012 model does make use of some methane matching via a single northern core (NGRIP), which has a large gap in the middle of its gas record. It also establishes relative tie points via three volcanic events, and an overall parallel chronology using the layer-counting GICC05 age model for NGRIP and DATICE Bayesian inverse modeling software (Veres et al., 2013). The methane matched model as published by Brooks makes use of gas data from GISP2 and GRIP in the north, as well as Vostok and Byrd in the south, using Monte Carlo simulations to find the highest correlation coefficient for the available gas time series. The use of all of these cores allows for a larger number of near continuous gas samples to be established at both poles and aligned. These are then matched to Schwander's absolute age model, which is noted as having centennial scale uncertainty in this case (Blunier et al., 2007). While further Monte Carlo analysis has been used to extend this methane matching to NGRIP (as well as Fuji and DomeC in the south) (Oh et al., 2014), the spectra of this core is characterized by a strong spectral hole that is not duplicated in the other northern cores. As such, using this core as the only tie point for the deconvolutions results in potentially biased spectra for both age models. We

are able to accommodate this using the other available cores in the methane matched age model (see Supplemental Figure 1).

However, the AICC2012 record does not allow for equivalent stacking. In addition, the focus of the AICC2012 dataset was to provide a more accurate absolute chronology in the south, with the addendum of matching this to the GICC05 age model in the north. This results in the further altering of the southern cores between cross-polar tie points, including shifts of cross-polar methane records and thus larger variation in relative phases (Veres et al., 2013). The reliance on absolute dates in the southern cores as opposed to relative dates between the poles increases after 60 kyra, over a third of the available record (especially given that the Holocene is not included in the methane matched age model). Indeed, the authors of the AICC2012 model noted millennial scale differences in the relative event chronology from previous, Greenland focused, age models (Veres et al., 2013). This is suggested to be due to potentially poorly understood thinning behavior and glacial dynamics near the bedrock of Greenland. Further work to extend this model into northern cores, with more focus on the glacial dynamics, more stacked methane records and cross-core event comparisons, or further improvements to the absolute dating of the methane matched records would improve the accuracy of our results. Overall, the focus of the AICC2012 model on absolute dating of the southern records does not currently make it preferable to the methane matched age model for an analysis of the relationship between the polar climates.

Materials and Methods: The data used in this paper is available through NOAA and the cited resources in the Supplemental Section: Age Model Details. Details of the extension of the methane matched age models and the butterworth filters applied to select for sub-Milankovitch

climate signals follow Oh et al. (2014). The resulting time series were then paired and deconvolved, using the water level, Weiner, Damped Least Squares (DLS), Tikhonov and Truncated Singular Value Decomposition regularization methods, as well as a wide span of regularization factors (see Supplemental Figures 1, 2 for details) to ensure peak stability for a range of regularizations. Specifically, we used Mathematica, Matlab, and R codes for deconvolution, using standard code packages in Mathematica and Matlab to confirm results in R. The resulting spectra were plotted in log log and linear plots for clearer interpretation.

APPENDIX 3: CHAPTER THREE SUPPLEMENTAL INFORMATION

The Supplemental Information for Chapter 3 is as follows:

Supplemental Discussion of ENSO and ACW:

The ACW, as mentioned in the main text, is a natural candidate for a uniting, driving mechanism for these oscillators, given that it is the largest, consistently identified oscillating phenomenon encompassing the entirety of the region studied in this paper. However, its robustness and persistence prior to 1984 have been questioned [Connolley 2002]. Despite this, our analysis shows no significant correlation between the dipoles and this oscillation index. The El Niño – Southern Oscillation (ENSO) also has a quasi-periodic behavior with a comparable periodicity and significant global climate impacts, and has higher correlation coefficients than the ACW for both dipoles. However, following the example of Shakun and Shaman [2009] in their work to establish the independence of the South Pacific Decadal Oscillation from the Pacific Decadal Oscillation, an AR1 model method may be used with the appropriate extensions to show that SPDO and SIDO are not subsumed by the ACW or any other previously published climate oscillation, though they do appear to interact with ENSO.

To begin discussing the differences between our dipoles and these previously identified teleconnections, we note several key works that clearly define the physical characteristics of both the ACW and ENSO systems. The ACW was first identified and defined by White and Peterson [1996] as anomalies in sea level pressure, wind stress, sea surface temperature, and sea-ice extent around Antarctica as caused by SST anomalies in the western, subtropical, South Pacific, spreading south and east in the ocean on an inter-annual scale. Qiu and Jin [1997] disputed this characterization and provided evidence that the ACW oscillations are better defined as the result of instability in the Antarctic Circumpolar Current (ACC) and the corresponding atmospheric

reactive behavior, instead of being directly forced by tropical ENSO activity. White et al. [1998] later published an article describing the covariance of SST and SLP anomalies in the Antarctic region, which created a spiral pattern in the Southern Ocean. This structure aligns with our dipoles, in that one oscillating center is found in the positive anomaly area we defined, while the other is in the negative, for both of our dipoles. This may suggest a pumping structure either driving the wave or resulting from the wave, but allows for how both teleconnecting structures may be active at once. However, our results indicate that the anomalies defined as dipoles in this paper are not smoothly transitioning around the ACC, as a simple wave pattern would require, but instead clearly oscillate at two distinct positions without any apparent direct connection (see Supplemental Figure S10). This indicates that they are synchronized through more intermediate systems, potentially smaller variations in pressure and wind. This indirect atmospheric connection better characterizes the observed behavior than a direct oceanic signal.

While the foregoing clearly separates the SPDO and SIDO dipoles from the ACW, other teleconnected systems located in the southern Pacific an Indian Oceans have been identified in previous publications. While not all patterns can be addressed here, the most relevant of these systems include the work of Garreaud and Battisti [1999] on the variability of the Southern Hemisphere tropospheric circulation and its connection to the interannual variability in the South Pacific basin around 30°S. Their analysis was confined to latitudes lower than 40°S, and thus does not include the full region of our study, or our dipoles. Behera and Yamagata [2001] did identify a subtropical SST dipole in the southern Indian Ocean known as the Indian Ocean Subtropical Dipole (IOSD), which is visible in the first PC of our EOF analysis, most clearly in February. However, stable, dipole-like oscillation is not seen for this system if the spatial range of the data is extended, and it remains relatively weak when compared to SIDO. Wang [2010]

and Moroika et al. [2012] both published links between SST anomalies within the southern ocean region of this study, and average rainfall events in Africa, though neither made clear use of defined dipole behavior in their investigations. Wang [2010] proposed unifying SST dipoles to represent a global climate mode throughout the southern, subtropical oceans, using latitudes below 45°S only. Moroika et al. [2012] confined their regional consideration to the southern Indian and southern Atlantic Oceans, with a direct comparison to the Southern African Rainfall Index (SARI) which averages rainfall anomalies south of 10°S from 1960-2008. Our study analyzes a much wider range of latitudes in both datasets, and clearly notes the dynamics of SSTA oscillations, providing a more comprehensive understanding of the larger interactions of the connections with the global climate system and previously identified indices.

As noted in the main text, we followed the procedures detailed in the work of Shakun and Shaman [2009] to define the independence of the SPDO and PDO indices. While their work focused on the decadal variations of the southern Pacific, our work confined the range of frequencies studied to inter-annual, sub decadal variations of the SSTA, due to the length and sampling rate of reliable data available. Specifically, we consider only the time recorded by satellite observation (1979-2011) to be unbiased, though the entire length of both data sets were used for the previously detailed analysis. We then modified the AR1 model, which took into account direct forcing from ENSO but no forcing from the PDO, in order to introduce a lag in connection with ENSO. The modified model is as follows:

$$Y_i = aY_{i-1} + bNino3.4 + \xi$$

Wherein Y is SPDO's DMI, i represents the time step, a and b are forcing amplitude on the data, and ξ is the random noise variable. Correlation coefficients between observed SPDO DMI and the DMI generated by the model to inspect the impacts of El Niño on the SPDO. Figure S12

144

shows that while some correlation between model and data can be achieved with minimal influence from the internal oscillation dynamics of the system or ENSO 3.4, in order to best fit the data, or even create a significant correlation coefficient, the two forcing parameters are required to be near 1. This shows a definite interaction between SPDO and ENSO, but also clearly demonstrates the independence of the internal oscillations of the SPDO system, indicating a self-organized, synchronized, mechanism for the dipole. SIDO also demonstrates this behavior, with less dependence on ENSO. The existence and importance of this internal oscillation of these systems supports the hypothesis that both oscillating dipole systems result from synchronizations of weakly interacting, nonlinear, climate oscillators, which have organized from some unknown initial state. Given that this stable phase relationship is often used to identify teleconnections, it is possible that some, if not all, previously identified, linked climate oscillators may be the result of this phenomenon.

Overall, while there are clear connections to previously identified climate oscillations, SPDO and SIDO are demonstrably independent of these behaviors and thus characterizing their internal dynamics and regional influences adds to our understanding of the global climate.

16 Dipole Summary:

a. Equatorial Pacific Region

The Equatorial Pacific is largely dominated by dipoles that show a clear relationship to El-Niño. Specifically, dipoles EP1-EP4 have one center fixed at Niño 3.4, while the other centers form a loose horseshoe shape surrounding the Niño 3.4 region. This term has been used previously (Ropelewski and Halpert, 1987) to describe the shape of climate behavior in this region, but our analysis shows the exact centers of oscillation, as well as making use of SST

145

proxies where previous studies used sea surface pressure and precipitation (Ropelewski and Halpert, 1987; Langenbrunner and Neelin, 2013). Figure 4 shows the dipoles in their normal mode, meaning it is cold over the equator, and shows the distinctive shape while also pinpointing the exact locations of our dipoles in contrast to the large regions usually used to create the shape. These differences will be discussed in more detail later. However, one may also question the uniqueness of these results after establishing this difference, since it appears that all 4 of these dipoles are directly related to El Niño patterns.

However, despite the fact that the strength of El Niño is defined by the combined results of several climate indexes (including Niño 3.4 and the southern oscillation index), the overall effects of El Niño are stronger when the temperature gradient between Niño 3.4 and the adjacent ocean is larger. Thus our use of the SSTA proxies gives a more direct insight into El Niño's behavior, as it allows us to look directly at the severity of the gradient oscillations across the entire structure of the system.

This observation reveals several groupings of the dipoles, all of which demonstrate distinct teleconnection patterns when compared to other dipoles in the group or even to the external climate indices, despite sharing one center of oscillation. Firstly, they all have a characteristic frequency of DMI, with a period of about 5.3 years. Secondly, one may divide them into two groups based on their locations: those centers located in the northern hemisphere are also to the north-west of Niño 3.4, while those located in the southern hemisphere are all to the south-west of Niño 3.4. Most likely, this arrangement is due to the trade winds, which, under ordinary modes (non-El Nino mode), create upwelling of cooler, deep ocean water in the eastern Pacific while also driving this cooler water to the central Pacific along the equator. This in turn forces the usual warmer water to the northern and southern sides of the western Pacific (Ahrens, 2010).

146

Finally, one of the most interesting characteristics to consider in the dipoles of the Equatorial Pacific is how they relate to the Pacific Decadal Oscillation. Obviously, they have very different frequencies of oscillation, but there are strong correlation coefficients that are unique to each dipole, once again illustrating the distinctive nature of these teleconnections. For example, EP1 and the PDO have a correlation coefficient of 0.57, which is well above the level of statistical significance for this analysis. However, while EP2 and the PDO do have a correlation coefficient of 0.45, EP2 shows much stronger relations to other dipoles in the west equatorial Pacific region. Thus, despite the single fixed center for these dipoles, EP1 is more closely connected to climate variations in the North Pacific/North America area, while EP2 is most strongly related to the western equatorial Pacific, adding additional complexity to the arrangement of dipole teleconnections in this region.

b. North Pacific Region

There are only two dipole modes found over the range of the North Pacific basin, which we have named NP1 and NP2. NP1 oscillates between the Bering Sea and off the coast of Japan, while NP2 is off the coast of Washington/Oregon and near the middle of the basin at a slightly lower latitude. The periods of their DMIs are approximately 5.3 years, which may lead the reader to assume that they are a manifestation of the North Pacific Oscillation (NPO), NPGO or PDO. However, our results once again indicate clear differences between the characteristics used to define the NPO and those we see in the behavior of our dipoles. The specifics of this are expanded later on in the discussion.

Our results begin to demonstrate that NP1 has no statistically significant relationship to El Niño. NP2 does show a correlation coefficient of 0.51 to Niño 3.4, but also has a far stronger interaction to all four of the equatorial Pacific dipoles: 0.74 with EP1, 0.6 with EP2, 0.65 with

EP3, and 0.6 with EP4. Both EP2 and EP3 require a forward time shift of 4 months in this case, meaning that these equatorial oscillations most closely precede and predict the behavior of the northern oscillation by four months. Not only that, but the four equatorial dipoles show higher correlation coefficients with NP2 than they do with El Niño itself.

The locations of these four oscillators (Illustrated in Figure 3) are of interest, given the split of timing relationships – EP1 and EP4 are as east as possible, while EP2 and EP3 seem to lead from the west. This division is yet another source of information about how these dipoles have been formed and how they continue to function, although the physical implications that this pattern has for the system will require a different method of study to understand fully.

c. South Pacific Region

The South Pacific Region also holds two dipole oscillators, here called SP1, which ranges from off southeast New Zealand to about the polar front 20° further east, and SP2, which starts near the coast of northern Peru and is linked a point nearly parallel with the southern tip of the country, though much further out. Despite their proximity, they are not significantly correlated. Moreover, SP1 has a period of oscillation of 5.3 years, while SP2 has one of 4.1 years. While other proxies have shown a pattern similar to SP1 (Mo and Higgins, 1998), SP1 is demonstrably more complex, showing clear maximum correlation with EP1 (0.53), EP2 (0.57), and EP4 (0.49) with the application of a four-month time shift (SP1 following), while EP3 requires no time shift at all for a correlation of 0.56. This suggests that SP1 is connected to El Nino with 4 months delay but is directly connected to the SW center of EP3 without any time lag at all.

The placement of SP1 also suggests a connection to the Antarctic Circumpolar Wave (ACW) as part of a much larger system, but this will also be discussed more fully after all

dipoles have been presented. Meanwhile, SP2 shows a strong relationship to many of the El Niño influenced systems, but leads them by four months for the highest correlation coefficients. This includes Niño 3.4 itself, which has a 0.44 correlation coefficient, as well as EP2 (-0.45), EP3 - 0.47), and EP4 (-0.42). This suggests that this dipole could be seen as a precursor of El Niño, making it potentially useful for forecasting, but at the very least an indicator of the complexity of the teleconnections and examples of synch studied here.

d. North Atlantic Region

The North Atlantic Region shows four dipole modes, creating one of the most complex ocean basin dipole patterns. Labeled NA1-NA4, the system contains several different periods of oscillation: 4.1, 3.2, 4.1, and 5.1 respectively. Once again, a teleconnection pattern has been previously identified in the region, this time called the North Atlantic Tripole. In this case, the variety of published, hypothesized, oscillating centers for this phenomena make it difficult to confirm or deny that this feature is entirely separate from our NA1 and NA2. However, it is worth pointing out that NA1 and NA2 do share a center of oscillation, an oscillating period, and nearly the same internal correlation coefficient, all of which suggest that they could be considered as a tripole. Still, for the purposes of this paper, they may just as easily be considered as a set of dipoles. The advantages to considering them as such are that we may keep a consistent method with the rest of our analysis, while also considering the different regional impacts of both dipoles.

Due to the overlapping nature of all four of these dipoles, though, there is a high degree of inter-dipole correlation. Still, they present as independent not only in period but also in their directions: those dipoles located in the subtropics create NW-SE diagonals, while those above the subtropics are arranged on a SW-NE bias. In addition to this, NA2 specifically shows a high

correlation with NAO (0.45), an oscillation based on surface sea-level pressure (SSP) differences between the Subtropical (Azores) High and the Subpolar Low (Barnston and Livezey, 1987), with no relation at all to SST. Though pressures are related to temperature, SST is more informative in the broader context of climate variability, making NA2 a very important climate indicator, especially given that it is far more localized than NAO, which is defined as covering the entire north Atlantic above the 30°N line. Of all the patterns in this region, NA2 shows the most potential to be broadly informative on climate variability in the region, but even so, the other oscillators all show distinct teleconnection behavior in far closer quarters than anywhere else in the oceans.

e. Southern Ocean and Indian Ocean Regions

The Southern and Indian Oceans hold three dipoles in total (SO1, SO2, and IO1), but are best considered together as IO1, the sole Indian Ocean dipole, has one end which is nearly in the Southern Ocean. Also, all three show the same NW-SE pattern, as one might expect given the circumpolar currents and winds, which could be used to suggest that all three are simply components of the Antarctic Circumpolar Wave (ACW). However, the similarities quickly fall apart, leaving three of the most distinct dipoles found in the same region. Each has a distinct period: SO1 has a period of 4.5 years, SO2 has 4.9, and IO1 has 6.2. None of them show significant correlation to any of the others. However, SO1, which may actually have been previously identified by Yuan and Martinson (2000) in their study of SSTA and Antarctic sea ice extent (though a similar pattern was also noted in an eddy streamfunction proxy by Mo and Higgins (1998)), shows strong connections to El Niño related oscillators. Specifically, SO1 and Niño 3.4 have a correlation coefficient of 0.55 when Niño 3.4 is forward shifted by four months. Applying this same 4 month lead to EP1-EP4 results in significant correlation coefficients in all

4 of the dipoles (-0.55, -0.59, -0.59, and -0.6 respectively), making the correlation coefficients between SO1 and all of the El Niño related indices stronger than that of SO1 and the ACW. Our results therefore indicate that the movement of energy about Antarctica is more complex than a smooth transfer of energy in a ring.

f. South Atlantic Ocean Region

The South Atlantic Ocean boasts the final dipole to be discussed, which has been named SA1. Located nearly directly between Africa and South America on a NE to SW diagonal, SA1 has a period of 3.5 years. Of all the dipoles identified, this one shows the most published research nearly duplicating its behavior (Venegas et al., 1996; Morioka, 2012) from SSTA analysis. Still, its behavior is interesting in the context of the larger system of dipoles, as it may provide a symmetry for NA1.